STUDIES OF INTERACTIONS OF SMALL MOLECULES WITH MEMBRANES AND PROTEINS

By

Sahishna M. Phaniraj

Submitted to the graduate degree program in Medicinal Chemistry and the Graduate Faculty of the University of Kansas in partial fulfillment of the requirements for the degree of Doctor of Philosophy.

_____

Co-Chairperson Dr. Blake R. Peterson

_____

Co-Chairperson Dr. Michael S. Wolfe

_____

Dr. Michael F. Rafferty

_____

Dr. Paul R. Hanson

_____

Dr. Jeffrey P. Krise

Date Defended: November 8, 2019

School of Pharmacy, Room 1020

The Dissertation Committee for Sahishna M. Phaniraj

certifies that this is the approved version of the final dissertation:

STUDIES OF INTERACTIONS OF SMALL MOLECULES

WITH MEMBRANES AND PROTEINS

_____

Co-Chairperson Dr. Blake R. Peterson

_____

Co-Chairperson Dr. Michael S. Wolfe

Date Approved: November 8, 2019

ABSTRACT

The modern molecular understanding of biological systems relies on integration of principles, practices, and techniques from diverse fields such as molecular biology, biochemistry, and biophysics. This approach has provided great insights into the molecular complexity of living cells. However, studies of some biological assemblies, such as the dynamic collection of lipids, proteins, and other biomolecules that make up cellular membranes, remains a challenge. To simplify these systems, and enable investigations of their structure and function, a wide range of membrane-mimetic models have been developed. Chapter 1 of this dissertation reviews some of the most important methods for studies of these types of biological systems, including recently developed lipidic nanodiscs. In Chapter 2 of this dissertation, I describe the design and construction of a new class of nanodiscs that are stabilized by covalent crosslinking of a membrane scaffold protein. These nanodiscs, termed SpyDiscs, uniquely enable imaging of pore formation by membrane-disruptive peptides. Another class of molecules that interacts with biological membranes is described in Chapter 3 of this dissertation. In this chapter, we report the synthesis of a new class of hydrophobic fluorescent probes that can be used to visualize the endoplasmic reticulum of living cells. The final chapter of this dissertation describes a fluorescence polarization assay developed to study protein-protein interactions involved in iron homeostasis in the pathogenic bacterium *Pseudomonas aeruginosa*. These binding studies along with other observations offer a promising target for inhibition of this pathogen as a strategy to overcome multidrug resistance observed with this superbug.

ACKNOWLEDGEMENTS

First and foremost, I would like to thank my advisor, Dr. Blake R. Peterson, for his valuable guidance and mentorship. He has helped me grow as a research scientist and has taught me how to question things and express ideas. I would also like to thank the entire faculty of the Department of Medicinal Chemistry for their teaching and expertise throughout my graduate career. Special thanks to the members of my defense committee, Dr. Michael Wolfe, Dr. Mike Rafferty, Dr. Paul Hanson, and Dr. Jeff Krise, for their time and consideration.

I also thank all the Peterson lab members, past and present, especially Dr. Zhe Gao, Dr. Kelsey Knewtson and Angelo Andres, for their friendship, and the endless conversations that made my time in Lawrence memorable. I greatly appreciate our collaboration with Dr. Mario Rivera and Dr. Huili Yao.

Finally, I need to thank my parents Prathibha and Phaniraj, my godparents Rajitha and Yadav, all my family and friends for their constant support and motivation. A special thanks you my aunt, Rajitha, for the unconditional love, and for being my go-to person. A massive thank you to my husband, Prajwal, for the unwavering support, and for the numerous sacrifices you have made for my dream to come true. Thank you for being so understanding, and for tolerating me. I love you, Kothi. You are the best thing that has ever happened to me.

TABLE OF CONTENTS

LIST OF FIGURES

LIST OF TABLES

LIST OF SCHEMES

Chapter 1

Biophysical and biochemical techniques for studies of membranes and proteins

Structural biology involves the study of molecular structure and dynamics of biological macromolecules. This field integrates principles of molecular biology, biochemistry and biophysics with biophysical and biochemical techniques to enable scientists to analyze substances and reactions underlying life processes. Biophysical techniques that are used to study the structure, properties, and functions of macromolecules at the atomic or molecular level include a range of methods such as microscopy, spectroscopy, electrophysiology, and molecular modelling. Biochemical analysis methods involve assays and procedures to evaluate the properties of biomolecules in biological systems. These techniques are involved in the purification and characterization of biomolecules. Together, biophysical and biochemical techniques have transformed our understanding of the nature and molecular complexity of living cells.

1.1. Models of cellular membranes

A wide variety of techniques have been developed to investigate the structures and biochemistry of biological membranes. These studies have been used to understand functionally important biological macromolecules such as proteins, carbohydrates and membrane-active peptides that interact with lipid bilayers that define membranes. These macromolecules are not isolated molecular entities but are surrounded by lipid molecules present in membranes, which play a crucial role in maintaining the structural and

functional integrity of the cell. To investigate these critical interactions, a wide range of membrane-mimetic models of a variety of lipid compositions have been developed and will be reviewed here.

In the 1970s, patch-clamp technique was used to study small patches of membranes or very small cells. It is an electrophysiological technique that measures electric current generated by a living cell. This technique was used for measuring drug effects and mechanism of diseases. This method makes use of real cellular membrane in contrast to the model membranes that are discussed below.

1.1.1. Liposomes and related structures

Liposomes[1-4] or vesicles are defined by a lipid bilayer that separates an aqueous internal compartment from the solvent aqueous phase. These model membranes were initially used in the study of membrane proteins to provide compartmentalization and a large bilayer area. They represent the most widely used technique for reconstitution of membrane proteins with lipids. This model is advantageous because it closely resembles structures of cell membranes and can consist of a single bilayer of phospholipids formed when detergent-solubilized lipids are sonicated to spontaneously assemble into a vesicle (Figure 1.1). During this process, a small amount of buffer is encapsulated into the vesicle. Methods used to disperse these lipids in aqueous medium include sonication, French pressure cell, freeze-thaw, membrane extrusion, and many others. A number of factors play a role in the preparation of liposomes of defined sizes for studies of biomolecules. These include physicochemical properties of lipids and other biomolecules, the concentration of material to be encapsulated, shelf-life, polydispersity, and the dispersion

medium for lipid vesicles. Variations in time and manipulations of the lipid ratio can be used to produce very small vesicles of various sizes.[1] Applications of liposomes include gene transfer[5,6] and drug delivery, where lipophilic drugs become encapsulated.[7-9] However, there are many challenges in using these vesicle systems because they can be turbid, viscous, and unstable over extended periods of time. Liposomes are frequently heterogenous multilamellar structures and proteins embedded in them experience different conformations that may make them unsuitable for structural studies by methods such as NMR. Furthermore, they tend to segregate into phase-separated domains that are not uniform in size. Another potential disadvantage of liposomes is that they may prevent accessibility of probes to both sides of proteins embedded in these structures if only one side of the protein faces the lumen or central cavity.

1.1.2. Supported monolayers, micelles, and bilayers

Other lipidic systems used to study membrane proteins include monolayers, micelles, and bicelles. Lipid monolayers are simple structural models that mimic either the inner or outer leaflet of cell membranes. These are mainly employed in the study of structural changes when proteins interact with lipid membranes.[10] Supported monolayers consist of the transfer/coating of monomolecular films of lipids onto solid substrates such as silica beads.[11] However, the applications of monolayers are limited and are mostly used to obtain structural studies of embedded proteins by NMR. Micelles are monolayer aggregate of lipid molecules that arrange themselves in a spherical form in aqueous solutions (Figure 1.1). When lipids are dispersed in aqueous media, the hydrophobic chains of lipids aggregate on the inside of a micelle with the non-polar heads on the

outside.[12,13] Micelles are formed with the help of detergents where they can trap other hydrophobic molecules. They help extract membrane proteins by solubilization. Micelles are generally used in biochemical studies of solubilized integral membrane proteins.[14-16] However, detergents can influence the conformation of a protein present in the hydrophobic core of micelle, and lipid packing has an influence on the membrane protein function in lipid bilayers.[17] Another membrane mimetic employed to study membrane proteins by NMR are bicelles, also known as a bi-layered micelle.[18] Bicelles are lipidic structures and can be made with a variety of phospholipids, cholesterol, and ceramides.[19-21] They can be disc-shaped, cylindrical or lamellar depending on the composition of lipids, temperature, and hydration.[22-24] These can mimic a variety of membranes such as prokaryote, mitochondria, erythrocyte, and others.[25] However, controlling the precise lipid ratio is difficult in bicelles. Furthermore, diffusion of detergent into bicelles can cause protein instability and lead to aggregation.[26]

1.1.3. Nanodiscs

Nanodiscs represent a recently developed technology for studies of membrane proteins that is now considered to be superior to other membrane mimetics.[27-29] Nanodiscs are an assembly of phospholipid bilayers that are surrounded by a homodimer of an engineered lipoprotein termed a membrane scaffold protein (Figure 1.1). These structures exhibit well-defined sizes and can be used with various lipids to form the bilayer structures. They overcome several limitations of other membrane mimetics and provide an alternative approach to enable structure-functional studies of macromolecules that interact with membranes. Nanodiscs provide a more native-like membrane environment

than a micelle or liposome. Compared to bicelles, they do not require detergent in samples, and they offer greater flexibility in the choice of lipids used for assembly.

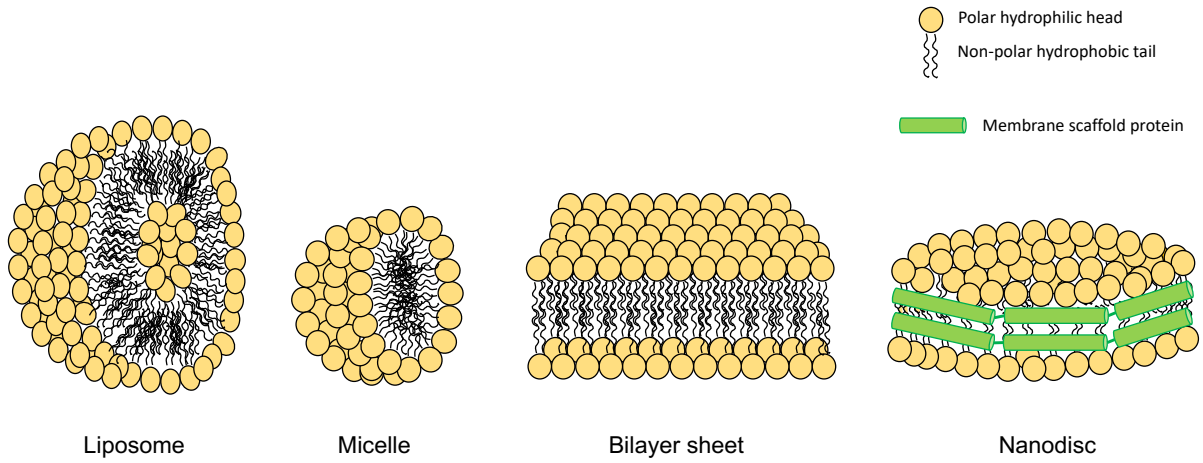

Figure 1.1. Membrane mimetic models. Cartoon representations of liposomes, micelles, bilayer sheets, and nanodiscs.

Nanodiscs are considered a state-of-the-art chemically-defined lipid bilayer. They mimic biomembranes and can self-assemble to incorporate integral membrane proteins. This system uniquely provides a nanometer scale membrane of defined and controlled composition, providing an attractive method for a variety of biophysical and biochemical studies of membrane proteins and peptides. The design of nanodiscs[30,31] was based on high-density lipoprotein (HDL), also known as good cholesterol. HDL is a part of a reverse cholesterol transport system that brings cholesterol and cholesterol esters back to the liver for elimination in bile.[32] The core protein component of HDL is apolipoprotein A-1 (apoA-1).[33] ApoA-1 consists of 10 alpha helices along with a globular region that does not interact with lipids. In 2004, Dr. Sligar of Univ. of Illinois genetically engineered the ApoA-1 protein to remove those parts of the sequence (the globular region and part of the first helix) that were not involved in forming these homogenous discs.[27] A

hexahistidine tag was further added to the N-terminus of the sequence for ease of purification (Figure 1.2). This engineered protein from human serum apoA-1 was termed membrane scaffold protein (MSP). MSP can form an amphipathic helix belt that wraps around the discoidal structure. These amphipathic helices are nonpolar on the inside against the alkyl chains of the phospholipids and they are polar on the outside to provide stability in aqueous buffer.

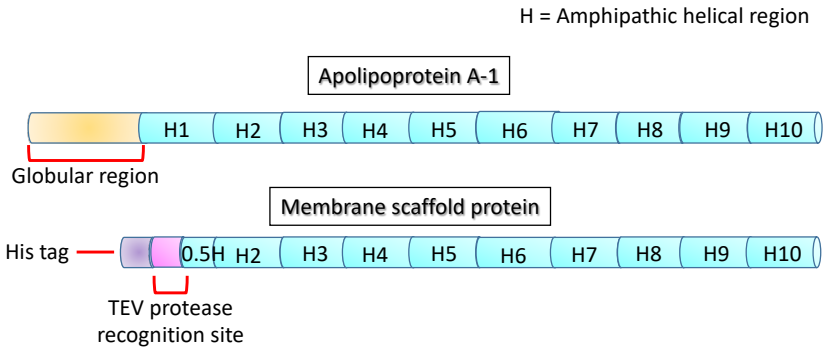

Figure 1.2. Secondary structural regions of apolipoprotein A-1 compared with the engineered membrane scaffold protein analogue.

Nanodiscs have been successfully assembled with synthetic lipids such as DMPC (1,2-dimyristoyl-sn-glycero-3-phosphocholine),[34-36] DPPC (1,2-dipalmitoyl-sn-glycero-3-phosphocholine),[37,38] POPC (1-palmitoyl-2-oleoyl-glycero-3-phosphocholine),[39-44] and mixtures of PC (phosphatidylcholine)[45-49] (Figure 1.3). Natural lipid mixtures such as *E. coli* lipids,[50-52] chicken egg PC lipids,[53,54] soy bean lipids,[55] and others have also been used to prepare nanodiscs. Nanodiscs are formed by a self-assembly process when precise molar ratios of phospholipids solubilized in detergent, membrane scaffold protein, and the detergent-solubilized target protein/peptide of interest are incubated at a specific temperature (Table 1.1).[27] Subsequent removal of detergent by dialysis or adsorbent beads initiates self-assembly of nanodiscs, where the target protein/peptide becomes

incorporated into the bilayer. These detergent-free nanodiscs are separated from lipid micelles and free proteins by size exclusion chromatography (Figure 1.4).

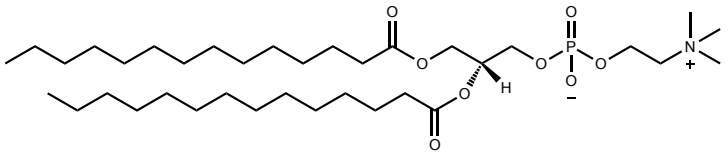

1,2-dimyristoyl-sn-glycero-3-phosphocholine (DMPC)

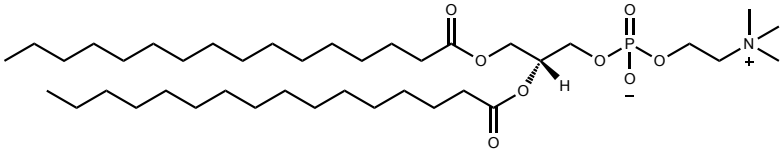

1,2-dipalmitoyl-sn-glycero-3-phosphocholine (DPPC)

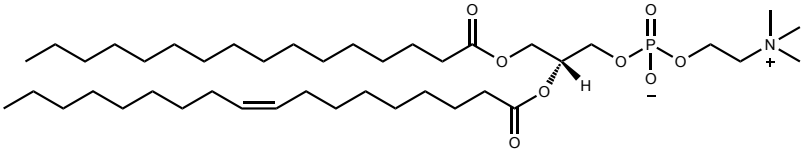

palmitoyl-2-oleoyl-glycero-3-phosphocholine (POPC)

Figure 1.3. Lipids commonly used for preparation of nanodiscs.

Table 1.1. The incubation temperature and optimal lipid : protein ratio used for the formation of nanodiscs. The phase transition temperature of individual lipids is listed.[27]

Phospholipid	Lipid phase transition temperature (T_m)	Incubation temperature for nanodisc formation	Optimal ratio of lipid : MSP1D1 protein
DPPC	41 °C	37 °C	90 : 1
DMPC	24 °C	25 °C	80 : 1
POPC	-2 °C	4 °C	65 : 1

Size exclusion chromatography (SEC) is a technique that separates biomolecules based on their size. SEC works by trapping smaller molecules in pores of an adsorbent material (stationary phase). As the solution travels down the column, molecules with a

larger size elute first followed by smaller molecules as they pass through the pores of the stationary phase and elute slowly. Because membrane proteins are of a variety of sizes, nanodiscs of different sizes are needed to study these proteins. Hence, the traditional membrane scaffold protein, which is derived from ApoA1 sequence (HDL), surrounding the nanodisc has been further engineered to give nanodiscs of different sizes for different applications.[55]

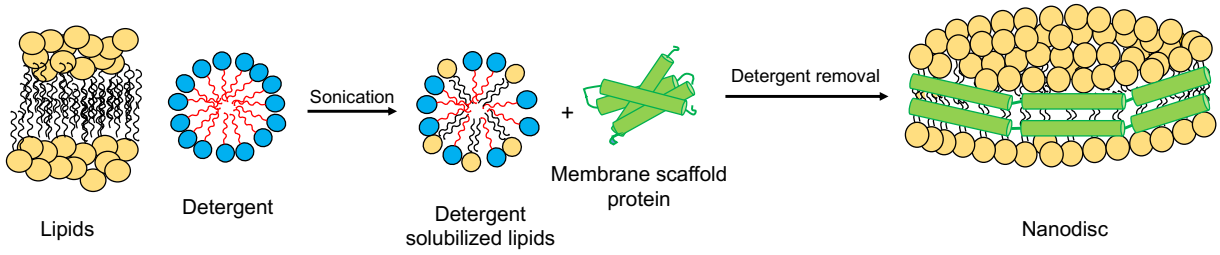

Figure 1.4. Production of empty nanodiscs. Nanodiscs are formed in a self-assembly process when detergent-solubilized lipids are incubated with membrane scaffold protein.

1.1.1.1. Stabilization of peptides and proteins in nanodiscs

The ability to engineer the membrane scaffold protein to create structures of well-defined molecular size and shape, in addition to the interchangeability and accessibility of the lipid and scaffold components, makes nanodiscs a versatile platform for diverse studies of model membranes. Empty nanodiscs have been thoroughly characterized using NMR methods to illustrate the structure of the membrane scaffold protein that surrounds the nanodisc,[56] to study lipid-MSP interactions,[57] and interactions of lipid head-groups with cations.[47] There are several advantages of nanodiscs compared to other membrane mimetic models. As individual membrane proteins are packed in separate nanodiscs, they can preserve target function, structure, and avoid aggregation. The possibility of uniformly sized nanodiscs has enabled high-resolution structures of

membranes proteins incorporated in nanodiscs using electron microscopy (EM). Three-dimensional reconstructions of these membrane proteins have yielded high-resolution images of membrane proteins in nanodiscs. A few examples include the ryanodine receptor, revealing the ordering of trans-membrane helices,[58] the structures of the TRPV1 ion channel,[59] Tc toxin,[60] lipoxygenase,[61] drug efflux pumps,[62] and the magnesium channel.[63] Thus, nanodiscs play an important role in structure determination of membrane proteins and their interactions.

1.1.1.2. Other applications of nanodisc technology

In addition to structural analysis of membrane proteins by EM, nanodiscs are also extensively used for a number of applications involving NMR and fluorescence methods. The first example of a membrane protein structure solved in nanodiscs by NMR was that of OmpX, which is a bacterial outer membrane protein.[64] Other applications of nanodiscs include:

- Spectroscopic single-molecule studies requiring attachment to a substrate,[65] as the samples are monodisperse, homogenous, and prevent protein self-aggregation.
- Atomic force microscopy and fluorescence spectroscopy[66,67] of membrane proteins.
- Ligand binding, protein dynamics, and molecular recognition events of enzymes[68] and electron transfer proteins.[69]
- Conformational studies of the cytoplasmic surface of G-protein coupled receptors (GPCR) induced by binding of ligand to the extracellular surface of a GPCR. The β2-adrenergic receptor (a GPCR) was studied in this way to profile receptor signaling.[70]

- Absorption of lipophilic compounds and high solubility can be used for the delivery of hydrophobic drugs.[71,72] Amphotericin B was incorporated into nanodiscs for the treatment of Leishmania in mice.[73,74]
- Binding studies of membrane proteins using surface plasmon resonance (SPR).[75-77] Affinity tags such as histidine, FLAG etc. added to the MSP sequence of nanodiscs allow attachment to the sensor surface, or the MSP can be genetically engineered to link biotin, sulfhydryl-reactive agents etc. Modification of MSP for attachment to the sensor surface enables label-free detection of unmodified membrane proteins. These nanodiscs allow accessibility to both sides of lipid bilayer for SPR studies.
- Nanodiscs made from a novel membrane scaffold protein used to investigate membrane-disruptive peptides is described in Chapter 2 of this dissertation. This is a new addition to the applications of nanodisc technology.

1.2. Fluorescent probes of biological systems

Fluorescent probes are powerful molecular tools to image cells in real-time and enable the visualization of biological structure and function. Fluorescent probes can be extremely sensitive and selective while minimally perturbing cell or subcellular components under study. Mammalian cells are highly complex and are compartmentalized using membrane-sealed cellular organelles associated with specific subsets of biomolecules. Major eukaryotic organelles include the nucleus, endoplasmic reticulum, mitochondria, golgi apparatus, endosomes, and lysosomes. This compartmentalization within organelles enables increased efficiency by segregation of specific chemical reactions.[78,79] For example, many proteins destined for localization in

the ER include the tetrapeptide sequence KDEL at the C-terminus.[80-82] Every organelle requires an appropriate microenvironment to function and disruption in organelle homeostasis or function can cause disease. For example, mitochondria generate reactive oxygen species (ROS) as mediators of oxidative stress.[83,84] Irregularity in this production of ROS leads to cardiac problems.[85] Therefore, monitoring the organelles and their microenvironment becomes crucial to understand their roles in cell function and the pathophysiology of the disease. In order to track and study these organelles in living cells, fluorescent probes are often used for optical imaging as they can allow direct visualization of subcellular structures with high sensitivity. Fluorescent probes that accumulate in specific organelles allow investigation of mechanisms of subcellular targeting because their specific accumulation can be readily observed by fluorescence microscopy.

1.2.1. Principles of fluorescence

Fluorescence[86] is a photophysical process observed when an object absorbs light at one wavelength and emits at a longer wavelength. Molecules that fluoresce are called fluorophores. The process of fluorescence can be represented with a Jablonski diagram[87] (Figure 1.5) that involves three stages: excitation, excited-state lifetime, and fluorescence emission. A fluorophore absorbs energy supplied by a light source such as an incandescent lamp or a laser.[88] It undergoes conformational changes and also interacts with its molecular environment that lead to partial dissipation of energy. This results in a relaxed singlet excited state (S_1) from where the photon is emitted to return the fluorophore to its ground state through the release of energy. Molecules can also be

returned to the ground state by other processes such as Förster resonance energy transfer (FRET) and collisional quenching.[89]

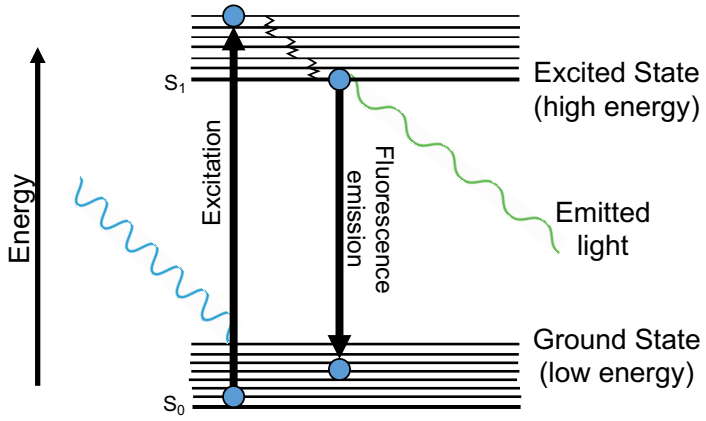

Figure 1.5. Jablonski diagram showing the processes involved in fluorescence.

1.2.2. Physicochemical properties and applications of fluorophores

Fluorescence spectral data are generally presented as fluorescence emission spectra, which is a plot of emission wavelength versus fluorescence intensity. Fluorophores have several specific properties such as absorbance, extinction coefficient (ε), quantum yield (Φ), and fluorescence life time (τ). The extinction coefficient of a fluorophore is the capacity for absorption of light at a given wavelength. The quantum yield is the amount of photons emitted per photons absorbed. The fluorescence lifetime (τ) of a fluorophore is the average time between its excitation and return to the ground state, typically 1-10 ns. Factors that influence fluorescence properties include the chemical structure of the fluorophore, the polarity and pH of the solvent in which the fluorophore is dissolved,[90] and the proximity and concentrations of fluorescence quenchers.[91,92] Modern instrumentation allows many fluorophores to be detected at very

low concentrations, and as a result, fluorescence technology is used extensively in biotechnology, flow cytometry, DNA sequencing, and many other applications.

1.2.2.1. Hydrophobic fluorophores for studies of membranes

Useful fluorescence for biological studies typically requires polyaromatic hydrocarbons or heterocycles. Extended conjugation shifts the absorption and fluorescence emission spectra to longer wavelengths to allow discrimination of fluorescent probes from intrinsically fluorescent biomolecules such as tryptophan. One application of fluorescence is the study of cell organelles by labelling of their membranes. Partitioning of hydrophobic probes into the nonpolar regions of membranes can be used to visualize these structures in cells. A wide variety of fluorescent lipid probes are available to label membrane structures (Figure 1.6).[89] Fluorophores can be attached to the fatty acid side chain (NBD-PC) or at the head group (Dansyl-PE) of different lipids. Other fluorophores such as fluorescein and rhodamine B (Figure 1.6) can also be linked to lipids for these types of studies.

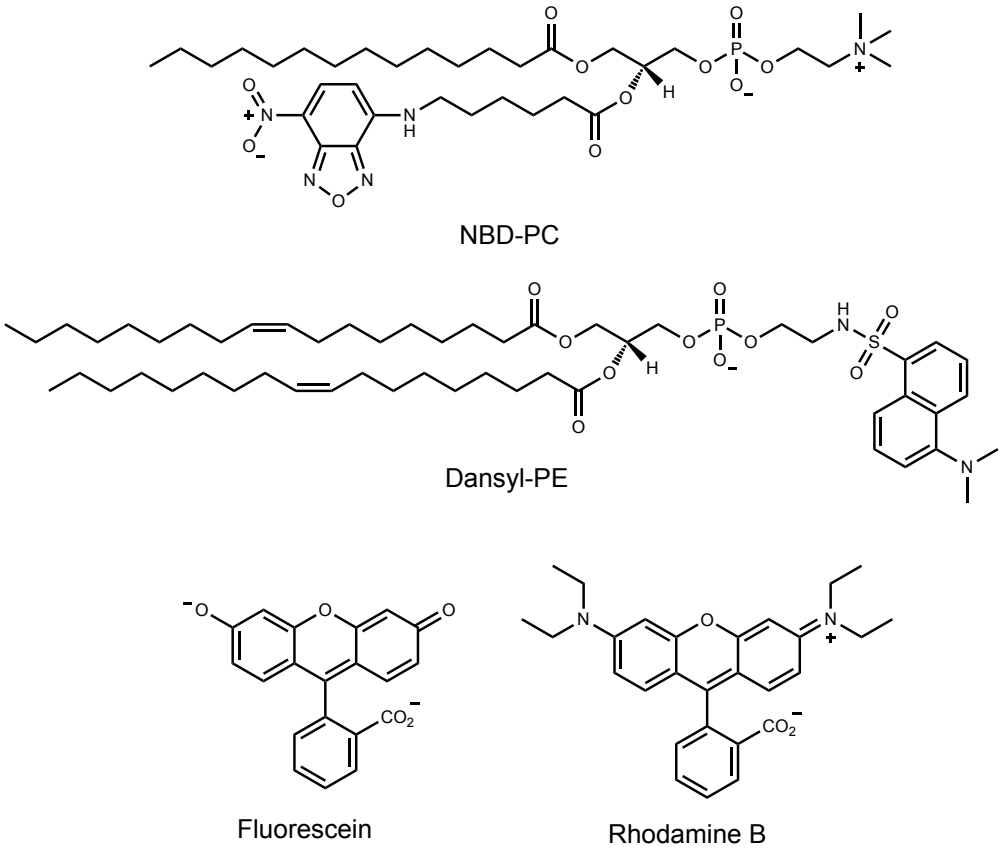

Figure 1.6. Fluorescent phospholipid analogues. PC = Phosphatidylcholine; PE = Phosphatidylethanolamine.

1.2.2.1.1. Fluorescent probes that associate with specific membranes of organelles

Fluorescent probes that label the plasma membrane and intracellular membranes have been extensively used for structural and biophysical analysis of these assemblies. Typical membrane phosphoglycerolipids of eukaryotes are phosphatidylserine (PS), phosphatidylethanolamine (PE), phosphatidylglycerol (PG), phosphatidylcholine (PC) and phosphatidylinositol (PI), and cardiolipin (CL).[79] For functions such as cell sorting and signal transduction, biomembranes contain at least five lipid classes. PC assembles into a bilayer because of its two fatty acyl chains and polar head group. PG and CL are synthesized in mitochondria, and mitochondrial CL promotes a non-bilayer configuration under charge neutralization conditions (divalent cations or high salt).[79] Inactivation of CL

synthase was found to be lethal in yeast,[93] which indicates that mitochondria require non-bilayer lipids. PE is also a non-bilayer lipid and is essential for functional embedding of membrane proteins, and membrane fusion and fission.[79] Along with glycerol-based phospholipids, eukaryotes contain sphingolipids and sterols, which are abundant in the plasma membrane and endosomes. Sphingolipids exhibit a solid gel phase, but they are fluidized by sterols. This combination of sphingolipids and sterols adds structural stability to membranes. The endoplasmic reticulum is high in PC and PI,[94,95] and these lipids are involved in the insertion of membrane proteins and secretory proteins. Cholesterol is also important for the physical properties of membranes and affects membrane thickness, rigidity, and lateral organization.[96] The lipid content of the plasma membrane consists of 30–50% cholesterol,[97,98] which is important for rigidity. On the contrary, membranes of the ER contain only 3–6% cholesterol.[99] It is thought that these differences in membrane composition, along with other physicochemical properties of an organelle, determines the accumulation of small molecules or fluorophores in specific organelle membranes. Alternatively, the association of molecular probes with organelle-specific resident proteins or linkage to a targeting signal can cause their accumulation in these compartments.

The endoplasmic reticulum (ER) is responsible for myriad important cellular functions including protein folding and unfolding, the synthesis of secreted and integral membrane proteins, lipid production, and calcium homeostasis. Relatively little is known about targeting of ER membranes with small molecules, but it has been proposed that amphipathic and moderately lipophilic compounds can selectively associate with the cholesterol-poor membranes of the ER.[100,101] A novel fluorophore that selectively targets and accumulates in the ER is described in Chapter 3 of this dissertation.

1.2.2.2. Fluorescent probes of receptor-ligand interactions

Receptor-ligand interactions play an important role in all biological events occurring in living cells. As a result, the discovery and quantification of binding of ligands to specific receptors is important for studying cellular pathways and drug development. Studies of receptor-ligand binding interactions can probe affinity, kinetics, conformational changes, specificity, and ligand efficiency, among others. In the early stages of drug discovery, compounds of interest are often initially identified based on affinity for a biological target. Binding assays with other targets can be further employed to assess ligand specificity. A meaningful receptor-ligand interaction often leads to a physiological response as a starting point for further development of a clinical drug candidate.

Several different techniques can be used to investigate receptor-ligand interactions. Fluorescence-based methods include fluorescence polarization (FP),[102] Förster resonance energy transfer (FRET),[103] and fluorescence intensity,[104] while non-fluorescence based techniques include isothermal titration calorimetry (ITC),[105] surface plasmon resonance (SPR),[106] nuclear magnetic resonance (NMR),[107] protein X-ray crystallography,[108] UV/Vis spectroscopy,[109] equilibrium dialysis,[110] and radiolabeling.[111] The advantages and limitations of each technique are listed in Table 1.2.

Table 1.2. Summary of ligand binding assays: advantages and disadvantages of the methods.[112,113]

Technique	Advantages	Disadvantages
Fluorescence polarization (FP)	• Measures kinetics and thermodynamics of binding • Simple, automated, suitable for HTS	• Susceptible to different fluorescent interferences • Difficult to obtain good fluorescent ligands for many receptors
Isothermal titration calorimetry (ITC)	• Quantitative thermodynamic data available • Directly measures heat exchange during complex formation • Non-destructive, high precision	• Complete thermodynamic profile not available • Not applicable to all systems, as large heat changes are required
Differential scanning calorimetry (DSC)	• Quantitative thermodynamic data available • Estimate stability of protein-ligand complexes	• Cannot control rate of experiment • Very sensitive to changes
Surface plasmon resonance (SPR)	• Real-time quantification of binding kinetics and affinities	• Prone to false positives • Target or ligand must be immobilized
Differential scanning fluorimetry (DSF)	• Real-time quantification of binding kinetics and affinities • Molecular details of receptor-ligand interactions	• Extensive optimization necessary • Prone to artifacts
Nuclear magnetic resonance (NMR)	• Molecular details of receptor-ligand interactions	• Expensive, time consuming • Generally, limited to small proteins
X-ray crystallography	• Solvent effect can be examined	• Protein target must crystallize • Expensive X-ray sources required

Radioligand binding assays	• Precise determination of receptor density, ligand binding sites and affinity	• Expensive • Hazards of handling radioactive materials

1.2.2.2.1. Fluorescence polarization

Fluorescence polarization (FP) was adopted in high throughput screening in mid 1990s to facilitate the drug discovery process. These assays are particularly useful because they are homogeneous, high-throughput, and can be inexpensive. They can provide quantitative measurement of receptor-ligand binding interactions and information on changes in molecular mobility, as the rotational rate of a free small ligand is faster compared to the rotational rate of a large receptor/protein-ligand complex.[114] As depicted in Figure 1.7, the rotation of a free ligand (a fluorophore in this case) is rapid, and this gives rise to a low polarization value. If this fluorophore is bound to protein, the rotation of the complex is slower due to a larger mass and gives rise to high polarization. The light emitted by a free ligand in solution is distributed in all direction as the free ligand rotates, whereas in case of protein-ligand complex the polarization of emitted light retains the polarization of excited light because it tumbles more slowly.[115]

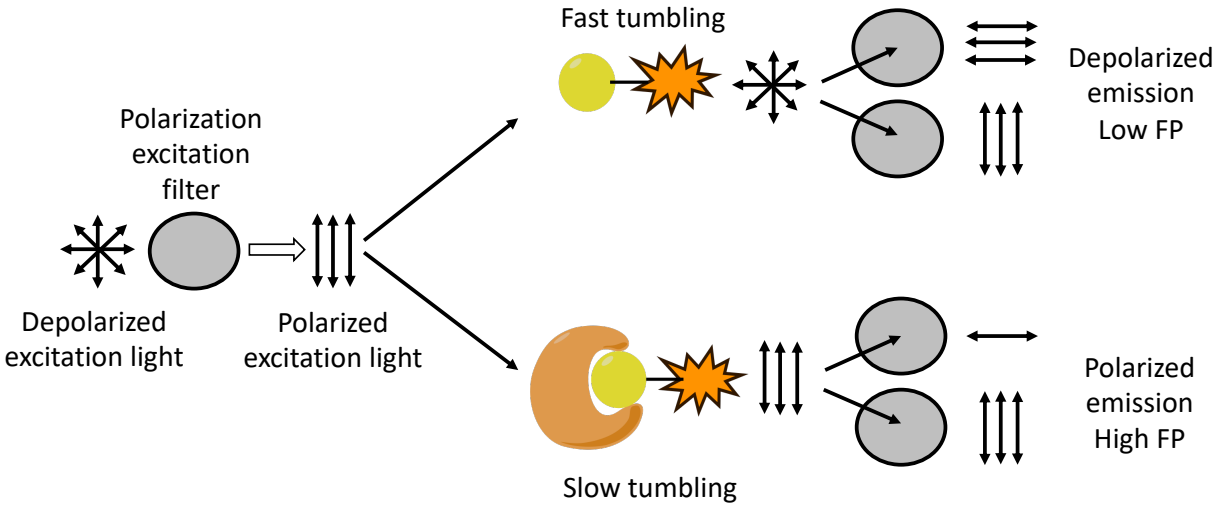

Figure 1.7. Schematic representation of fluorescence polarization of two samples: a free ligand in solution (top) and a protein-ligand complex (bottom).

In an FP assay, plane polarized light is used to excite a fluorophore. The fluorescence intensities in parallel (F_{II}) and perpendicular ($F_{\perp}$) directions to the plane of excitation are measured. The polarization (P) of the sample is calculated by the following equation:[115]

$$P = \frac{F_{II} - F_{\perp}}{F_{II} + F_{\perp}}$$

A fluorometer instrument capable of FP typically consists of an excitation light source (typically a Xe or Hg arc lamp) to excite the sample, excitation and emission polarizers (polaroid sheets or calcite polarizers), a filter or monochromator to remove scattered excited light, parallel and perpendicular polarizers to collect the emitted light and a sample platform (cuvette or multiwell plate).[114] To measure the affinity of a fluorescent ligand for a protein, the protein of interest is generally titrated into a fixed concentration of fluorescent ligand (below K_d) and allowed to reach equilibrium. In these types of experiments, it is important that effects on quenching or enhancement of the

fluorophore are evaluated in parallel because correction for these effects on the fluorescence lifetime is important to obtain accurate measurements of affinities. A fluorescence polarization assay to study protein-protein interactions is described in Chapter 4 of this dissertation.

1.3. Outline of this dissertation

My research has focused on the development of new biophysical and biochemical techniques in structural biology that would enable study of interactions of small molecules with membranes and proteins. In this dissertation, Chapter 2 describes modifications of nanodisc technology to generate covalently-linked, stabilized, nanodiscs in high yield based on the recently developed SpyCatcher/SpyTag system. Unlike traditional nanodiscs, these SpyDiscs were shown to enable studies of membrane-active agents. This approach provides a new tool for studies of biomolecules that disrupt membrane structure. Chapter 3 describes the synthesis and biological evaluation of novel hydrophobic resorufamine compounds that specifically accumulate in the ER. One of these compounds was used to facilitate visualization of small molecule-mediated release of a fusion protein from the ER into the secretory pathway. Finally, Chapter 4 reports the development of a fluorescence polarization assay for studies of ligands that inhibit a protein-protein interaction involved in iron homeostasis in pathogenic bacteria.

1.4. References

1. Miyamoto, V. K.; Stoeckenius, W., Preparation and characteristics of lipid vesicles. *J. Membr. Biol.* **1971***, 4*, 252-269.
2. Warschawski, D. E.; Arnold, A. A.; Beaugrand, M.; Gravel, A.; Chartrand, É.; Marcotte, I., Choosing membrane mimetics for NMR structural studies of transmembrane proteins. *Biochim. Biophys. Acta.* **2011***, 1808*, 1957-1974.
3. Maherani, B.; Arab-Tehrany, E.; R Mozafari, M.; Gaiani, C.; Linder, M., Liposomes: a review of manufacturing techniques and targeting strategies. *Curr. Nanosci.* **2011***, 7*, 436-452.
4. Bangham, A.; Standish, M. M.; Watkins, J. C., Diffusion of univalent ions across the lamellae of swollen phospholipids. *J. Mol. Biol.* **1965***, 13*, 238-IN227.
5. Welsh, N.; Oberg, C.; Hellerström, C.; Welsh, M., Liposome mediated in vitro transfection of pancreatic islet cells. *Biomed. Biochim. Acta.* **1990***, 49*, 1157-1164.
6. Wang, C. Y.; Huang, L., Highly efficient DNA delivery mediated by pH-sensitive immunoliposomes. *Biochemistry.* **1989***, 28*, 9508-9514.
7. Gabizon, A.; Chisin, R.; Amselem, S.; Druckmann, S.; Cohen, R.; Goren, D.; Fromer, I.; Peretz, T.; Sulkes, A.; Barenholz, Y., Pharmacokinetic and imaging studies in patients receiving a formulation of liposome-associated adriamycin. *Br. J. Cancer.* **1991***, 64*, 1125.
8. Geng, S.; Yang, B.; Wang, G.; Qin, G.; Wada, S.; Wang, J.-Y., Two cholesterol derivative-based PEGylated liposomes as drug delivery system, study on pharmacokinetics and drug delivery to retina. *Nanotechnology.* **2014***, 25*, 275103.

9. Gross, N.; Ranjbar, M.; Evers, C.; Hua, J.; Martin, G.; Schulze, B.; Michaelis, U.; Hansen, L. L.; Agostini, H. T., Choroidal neovascularization reduced by targeted drug delivery with cationic liposome-encapsulated paclitaxel or targeted photodynamic therapy with verteporfin encapsulated in cationic liposomes. *Mol. Vis.* **2013***, 19*, 54.

10. Brockman, H., Lipid monolayers: why use half a membrane to characterize protein-membrane interactions? *Curr. Opin. Struct. Biol.* **1999***, 9*, 438-443.

11. Linseisen, F. M.; Hetzer, M.; Brumm, T.; Bayerl, T. M., Differences in the physical properties of lipid monolayers and bilayers on a spherical solid support. *Biophys. J.* **1997***, 72*, 1659-1667.

12. Dill, K. A.; Koppel, D. E.; Cantor, R. S.; Dill, J. D.; Bendedouch, D.; Chen, S.-H., Molecular conformations in surfactant micelles. *Nature.* **1984***, 309*, 42.

13. Lipfert, J.; Columbus, L.; Chu, V. B.; Lesley, S. A.; Doniach, S., Size and shape of detergent micelles determined by small-angle X-ray scattering. *J. Phys. Chem. B.* **2007***, 111*, 12427-12438.

14. Eshaghi, S.; Hedrén, M.; Nasser, M. I. A.; Hammarberg, T.; Thornell, A.; Nordlund, P., An efficient strategy for high-throughput expression screening of recombinant integral membrane proteins. *Protein Sci.* **2005***, 14*, 676-683.

15. Columbus, L.; Lipfert, J.; Klock, H.; Millett, I.; Doniach, S.; Lesley, S. A., Expression, purification, and characterization of Thermotoga maritima membrane proteins for structure determination. *Protein Sci.* **2006***, 15*, 961-975.

16. Sanders, C. R.; Sönnichsen, F., Solution NMR of membrane proteins: practice and challenges. *Magn. Reson. Chem.* **2006***, 44*, S24-S40.

17. Andersen, O. S.; Koeppe, R. E., Bilayer thickness and membrane protein function: an energetic perspective. *Annu. Rev. Biophys. Biomol. Struct.* **2007***, 36*.

18. Noguchi, H., Structure formation in binary mixtures of lipids and detergents: Self-assembly and vesicle division. *J. Chem. Phys.* **2013***, 138*, 01B611.

19. Struppe, J.; Komives, E.; Taylor, S.; Vold, R., 2H NMR studies of a myristoylated peptide in neutral and acidic phospholipid bicelles. *Biochemistry.* **1998***, 37*, 15523-15527.

20. Struppe, J.; Whiles, J. A.; Vold, R. R., Acidic phospholipid bicelles: a versatile model membrane system. *Biophys. J.* **2000***, 78*, 281-289.

21. Tiburu, E. K.; Moton, D. M.; Lorigan, G. A., Development of magnetically aligned phospholipid bilayers in mixtures of palmitoylstearoylphosphatidylcholine and dihexanoylphosphatidylcholine by solid-state NMR spectroscopy. *Biochim. Biophys. Acta.* **2001***, 1512*, 206-214.

22. Raffard, G.; Steinbruckner, S.; Arnold, A.; Davis, J. H.; Dufourc, E. J., Temperature−Composition Diagram of Dimyristoylphosphatidylcholine−Dicaproylphosphatidylcholine “Bicelles” Self-Orienting in the Magnetic Field. A Solid State 2H and 31P NMR Study. *Langmuir.* **2000***, 16*, 7655-7662.

23. Arnold, A.; Labrot, T.; Oda, R.; Dufourc, E. J., Cation modulation of bicelle size and magnetic alignment as revealed by solid-state NMR and electron microscopy. *Biophys. J.* **2002***, 83*, 2667-2680.

24. Harroun, T. A.; Koslowsky, M.; Nieh, M.-P.; de Lannoy, C.-F.; Raghunathan, V.; Katsaras, J., Comprehensive examination of mesophases formed by DMPC and DHPC mixtures. *Langmuir.* **2005***, 21*, 5356-5361.

25. Marcotte, I.; Auger, M., Bicelles as model membranes for solid-and solution-state NMR studies of membrane peptides and proteins. *Concept Magn. Res. A.* **2005***, 24*, 17-37.

26. Triba, M. N.; Warschawski, D. E.; Devaux, P. F., Reinvestigation by phosphorus NMR of lipid distribution in bicelles. *Biophys. J.* **2005***, 88*, 1887-1901.

27. Denisov, I. G.; Grinkova, Y. V.; Lazarides, A. A.; Sligar, S. G., Directed self-assembly of monodisperse phospholipid bilayer Nanodiscs with controlled size. *J. Am. Chem. Soc.* **2004***, 126*, 3477-3487.

28. Denisov, I. G.; Sligar, S. G., Nanodiscs for structural and functional studies of membrane proteins. *Nat. Struct. Mol. Biol.* **2016***, 23*, 481.

29. Bayburt, T. H.; Sligar, S. G., Self-assembly of single integral membrane proteins into soluble nanoscale phospholipid bilayers. *Protein Sci.* **2003***, 12*, 2476-2481.

30. Brouillette, C. G.; Jones, J. L.; Ng, T. C.; Kercret, H.; Chung, B. H.; Segrest, J. P., Structural studies of apolipoprotein AI/phosphatidylcholine recombinants by high-field proton NMR, nondenaturing gradient gel electrophoresis, and electron microscopy. *Biochemistry.* **1984***, 23*, 359-367.

31. Jonas, A., Reconstitution of high-density lipoproteins. *Methods Enzymol.* **1986***, 128*, 553.

32. Cohen, D. E.; Fisher, E. A. (**2013**). *Lipoprotein metabolism, dyslipidemia, and nonalcoholic fatty liver disease.* Paper presented at the Seminars in liver disease.

33. Shoulders, C. C.; Kornblihtt, A. R.; Munro, B. S.; Baralle, F. E., Gene structure of human apolipoprotein Al. *Nucleic Acids Res.* **1983***, 11*, 2827-2837.

34. Xu, H.; Hill, J. J.; Michelsen, K.; Yamane, H.; Kurzeja, R. J.; Tam, T.; Isaacs, R. J.; Shen, F.; Tagari, P., Characterization of the direct interaction between KcsA-Kv1. 3 and its inhibitors. *Biochim. Biophys. Acta.* **2015***, 1848*, 1974-1980.

35. Tark, S.-H.; Das, A.; Sligar, S.; Dravid, V. P., Nanomechanical detection of cholera toxin using microcantilevers functionalized with ganglioside nanodiscs. *Nanotechnology.* **2010***, 21*, 435502.

36. Bayburt, T. H.; Carlson, J. W.; Sligar, S. G., Reconstitution and imaging of a membrane protein in a nanometer-size phospholipid bilayer. *J. Struct. Biol.* **1998***, 123*, 37-44.

37. Xu, X.-P.; Kim, E.; Swift, M.; Smith, J. W.; Volkmann, N.; Hanein, D., Three-dimensional structures of full-length, membrane-embedded human αIIbβ3 integrin complexes. *Biophys. J.* **2016***, 110*, 798-809.

38. Grinkova, Y. V.; Denisov, I. G.; Waterman, M. R.; Arase, M.; Kagawa, N.; Sligar, S. G., The ferrous-oxy complex of human aromatase. *Biochem. Biophys. Res. Commun.* **2008***, 372*, 379-382.

39. Mak, P. J.; Denisov, I. G.; Grinkova, Y. V.; Sligar, S. G.; Kincaid, J. R., Defining CYP3A4 structural responses to substrate binding. Raman spectroscopic studies of a nanodisc-incorporated mammalian cytochrome P450. *J. Am. Chem. Soc.* **2011***, 133*, 1357-1366.

40. Mak, P. J.; Gregory, M. C.; Denisov, I. G.; Sligar, S. G.; Kincaid, J. R., Unveiling the crucial intermediates in androgen production. *Proc. Natl. Acad. Sci.* **2015***, 112*, 15856-15861.

41. Mak, P. J.; Gregory, M. C.; Sligar, S. G.; Kincaid, J. R., Resonance Raman spectroscopy reveals that substrate structure selectively impacts the heme-bound diatomic ligands of CYP17. *Biochemistry.* **2013***, 53*, 90-100.

42. Mak, P. J.; Luthra, A.; Sligar, S. G.; Kincaid, J. R., Resonance Raman spectroscopy of the oxygenated intermediates of human CYP19A1 implicates a compound I intermediate in the final lyase step. *J. Am. Chem. Soc.* **2014***, 136*, 4825-4828.

43. Nakatani-Webster, E.; Hu, S.-L.; Atkins, W. M.; Catalano, C. E., Assembly and characterization of gp160-nanodiscs: A new platform for biochemical characterization of HIV envelope spikes. *J. Virol.* **2015***, 226*, 15-24.

44. Shaw, A. W.; Pureza, V. S.; Sligar, S. G.; Morrissey, J. H., The local phospholipid environment modulates the activation of blood clotting. *J. Biol. Chem.* **2007***, 282*, 6556-6563.

45. Ye, X.; McLean, M. A.; Sligar, S. G., Conformational equilibrium of talin is regulated by anionic lipids. *Biochim. Biophys. Acta.* **2016***, 1858*, 1833-1840.

46. Zhang, P.; Ye, F.; Bastidas, A. C.; Kornev, A. P.; Wu, J.; Ginsberg, M. H.; Taylor, S. S., An isoform-specific myristylation switch targets type II PKA holoenzymes to membranes. *Structure.* **2015***, 23*, 1563-1572.

47. Boettcher, J. M.; Davis-Harrison, R. L.; Clay, M. C.; Nieuwkoop, A. J.; Ohkubo, Y. Z.; Tajkhorshid, E.; Morrissey, J. H.; Rienstra, C. M., Atomic view of calcium-induced clustering of phosphatidylserine in mixed lipid bilayers. *Biochemistry.* **2011***, 50*, 2264-2273.

48. Her, C.; Filoti, D. I.; McLean, M. A.; Sligar, S. G.; Ross, J. A.; Steele, H.; Laue, T. M., The charge properties of phospholipid nanodiscs. *Biophys. J.* **2016***, 111*, 989-998.

49. Eggensperger, S.; Fisette, O.; Parcej, D.; Schäfer, L. V.; Tampé, R., An annular lipid belt is essential for allosteric coupling and viral inhibition of the antigen translocation complex TAP (transporter associated with antigen processing). *J. Biol. Chem.* **2014***, 289*, 33098-33108.

50. Finkenwirth, F.; Sippach, M.; Landmesser, H.; Kirsch, F.; Ogienko, A.; Grunzel, M.; Kiesler, C.; Steinhoff, H.-J.; Schneider, E.; Eitinger, T., ATP-dependent conformational changes trigger substrate capture and release by an ECF-type biotin transporter. *J. Biol. Chem.* **2015***, 290*, 16929-16942.

51. Hörnschemeyer, P.; Liss, V.; Heermann, R.; Jung, K.; Hunke, S., Interaction analysis of a two-component system using Nanodiscs. *PLoS One.* **2016***, 11*, e0149187.

52. Dominik, P. K.; Borowska, M. T.; Dalmas, O.; Kim, S. S.; Perozo, E.; Keenan, R. J.; Kossiakoff, A. A., Conformational chaperones for structural studies of membrane proteins using antibody phage display with nanodiscs. *Structure.* **2016***, 24*, 300-309.

53. Mi, L.-Z.; Grey, M. J.; Nishida, N.; Walz, T.; Lu, C.; Springer, T. A., Functional and structural stability of the epidermal growth factor receptor in detergent micelles and phospholipid nanodiscs. *Biochemistry.* **2008***, 47*, 10314-10323.

54. Bajaj, R.; Bruce, K. E.; Davidson, A. L.; Rued, B. E.; Stauffacher, C. V.; Winkler, M. E., Biochemical characterization of essential cell division proteins FtsX and FtsE that mediate peptidoglycan hydrolysis by PcsB in Streptococcus pneumoniae. *Microbiologyopen.* **2016***, 5*, 738-752.

55. Öjemyr, L. N.; Von Ballmoos, C.; Gennis, R. B.; Sligar, S. G.; Brzezinski, P., Reconstitution of respiratory oxidases in membrane nanodiscs for investigation of proton-coupled electron transfer. *FEBS Lett.* **2012***, 586*, 640-645.

56. Li, Y.; Kijac, A. Z.; Sligar, S. G.; Rienstra, C. M., Structural analysis of nanoscale self-assembled discoidal lipid bilayers by solid-state NMR spectroscopy. *Biophys. J.* **2006***, 91*, 3819-3828.

57. Kijac, A.; Shih, A. Y.; Nieuwkoop, A. J.; Schulten, K.; Sligar, S. G.; Rienstra, C. M., Lipid− protein correlations in nanoscale phospholipid bilayers determined by solid-state nuclear magnetic resonance. *Biochemistry.* **2010***, 49*, 9190-9198.

58. Efremov, R. G.; Leitner, A.; Aebersold, R.; Raunser, S., Architecture and conformational switch mechanism of the ryanodine receptor. *Nature.* **2015***, 517*, 39.

59. Gao, Y.; Cao, E.; Julius, D.; Cheng, Y., TRPV1 structures in nanodiscs reveal mechanisms of ligand and lipid action. *Nature.* **2016***, 534*, 347.

60. Gatsogiannis, C.; Merino, F.; Prumbaum, D.; Roderer, D.; Leidreiter, F.; Meusch, D.; Raunser, S., Membrane insertion of a Tc toxin in near-atomic detail. *Nat. Struct. Mol. Biol.* **2016***, 23*, 884.

61. Kumar, R. B.; Zhu, L.; Idborg, H.; Rådmark, O.; Jakobsson, P.-J.; Rinaldo-Matthis, A.; Hebert, H.; Jegerschöld, C., Structural and functional analysis of calcium ion mediated binding of 5-lipoxygenase to nanodiscs. *PLoS One.* **2016***, 11*, e0152116.

62. Daury, L.; Orange, F.; Taveau, J.-C.; Verchère, A.; Monlezun, L.; Gounou, C.; Marreddy, R. K.; Picard, M.; Broutin, I.; Pos, K. M., Tripartite assembly of RND multidrug efflux pumps. *Nat. Commun.* **2016***, 7*, 10731.

63. Matthies, D.; Dalmas, O.; Borgnia, M. J.; Dominik, P. K.; Merk, A.; Rao, P.; Reddy, B. G.; Islam, S.; Bartesaghi, A.; Perozo, E., Cryo-EM structures of the magnesium channel CorA reveal symmetry break upon gating. *Cell.* **2016***, 164*, 747-756.

64. Hagn, F.; Etzkorn, M.; Raschle, T.; Wagner, G., Optimized phospholipid bilayer nanodiscs facilitate high-resolution structure determination of membrane proteins. *J. Am. Chem. Soc.* **2013***, 135*, 1919-1925.

65. Pandit, A.; Shirzad-Wasei, N.; Wlodarczyk, L. M.; van Roon, H.; Boekema, E. J.; Dekker, J. P.; Willem, J., Assembly of the major light-harvesting complex II in lipid nanodiscs. *Biophys. J.* **2011***, 101*, 2507-2515.

66. Nath, A.; Trexler, A. J.; Koo, P.; Miranker, A. D.; Atkins, W. M.; Rhoades, E. Single-molecule fluorescence spectroscopy using phospholipid bilayer nanodiscs. In *Methods Enzymol.* **2010**,(Vol. 472, pp. 89-117): Elsevier.

67. Nath, A.; Koo, P. K.; Rhoades, E.; Atkins, W. M., Allosteric effects on substrate dissociation from cytochrome P450 3A4 in nanodiscs observed by ensemble and single-molecule fluorescence spectroscopy. *J. Am. Chem. Soc.* **2008***, 130*, 15746-15747.

68. Luthra, A.; Gregory, M.; Grinkova, Y.; Denisov, I.; Sligar, S. Nanodiscs in the studies of membrane-bound cytochrome P450 enzymes. In *Cytochrome P450 Protocols* **2013**,(pp. 115-127): Springer.

69. Laursen, T.; Singha, A.; Rantzau, N.; Tutkus, M.; Borch, J.; Hedegård, P.; Stamou, D.; Møller, B. L.; Hatzakis, N. S., Single molecule activity measurements of cytochrome P450 oxidoreductase reveal the existence of two discrete functional states. *ACS Chem. Biol.* **2014***, 9*, 630-634.

70. Lamichhane, R.; Liu, J. J.; Pljevaljcic, G.; White, K. L.; van der Schans, E.; Katritch, V.; Stevens, R. C.; Wüthrich, K.; Millar, D. P., Single-molecule view of basal activity and activation mechanisms of the G protein-coupled receptor β2AR. *Proc. Natl. Acad. Sci.* **2015***, 112*, 14254-14259.

71. Simonsen, J. B., Evaluation of reconstituted high-density lipoprotein (rHDL) as a drug delivery platform–a detailed survey of rHDL particles ranging from biophysical properties to clinical implications. *Nanomed. Nanotechnol.* **2016***, 12*, 2161-2179.

72. Ryan, R. O., Nanodisks: hydrophobic drug delivery vehicles. *Expert Opin. Drug Del.* **2008***, 5*, 343-351.

73. Cole, P.; Bishop, J.; Beckstead, J.; Titus, R.; Ryan, R., Effect of amphotericin B nanodisks on Leishmania major infected mice. *Pharm. Anal. Acta.* **2014***, 5*.

74. Oda, M. N.; Hargreaves, P. L.; Beckstead, J. A.; Redmond, K. A.; van Antwerpen, R.; Ryan, R. O., Reconstituted high density lipoprotein enriched with the polyene antibiotic amphotericin B. *J. Lipid Res.* **2006***, 47*, 260-267.

75. Trahey, M.; Li, M. J.; Kwon, H.; Woodahl, E. L.; McClary, W. D.; Atkins, W. M., Applications of lipid nanodiscs for the study of membrane proteins by surface plasmon resonance. *Curr. Protoc. Protein Sci.* **2015***, 81*, 29.13. 21-29.13. 16.

76. Bocquet, N.; Kohler, J.; Hug, M. N.; Kusznir, E. A.; Rufer, A. C.; Dawson, R. J.; Hennig, M.; Ruf, A.; Huber, W.; Huber, S., Real-time monitoring of binding events on a thermostabilized human A2A receptor embedded in a lipid bilayer by surface plasmon resonance. *Biochim. Biophys. Acta.* **2015***, 1848*, 1224-1233.

77. Glück, J. M.; Koenig, B. W.; Willbold, D., Nanodiscs allow the use of integral membrane proteins as analytes in surface plasmon resonance studies. *Anal. Biochem.* **2011***, 408*, 46-52.

78. Van Meer, G.; Voelker, D. R.; Feigenson, G. W., Membrane lipids: where they are and how they behave. *Nat. Rev. Mol. Cell Biol.* **2008***, 9*, 112.

79. van Meer, G.; de Kroon, A. I., Lipid map of the mammalian cell. *J. Cell Sci.* **2011***, 124*, 5-8.

80. Arar, K.; Monsigny, M.; Mayer, R., Synthesis of oligonucleotide-peptide conjugates containing a KDEL signal sequence. *Tetrahedron Lett.* **1993***, 34*, 8087-8090.

81. Singh, P.; Tang, B.; Wong, S. H.; Hong, W., Transmembrane topology of the mammalian KDEL receptor. *Mol. Cell. Biol.* **1993***, 13*, 6435-6441.

82. Yamamoto, K.; Fujii, R.; Toyofuku, Y.; Saito, T.; Koseki, H.; Hsu, V. W.; Aoe, T., The KDEL receptor mediates a retrieval mechanism that contributes to quality control at the endoplasmic reticulum. *EMBO J.* **2001***, 20*, 3082-3091.

83. Dickinson, B. C.; Srikun, D.; Chang, C. J., Mitochondrial-targeted fluorescent probes for reactive oxygen species. *Curr. Opin. Chem. Biol.* **2010***, 14*, 50-56.

84. D'Autréaux, B.; Toledano, M. B., ROS as signalling molecules: mechanisms that generate specificity in ROS homeostasis. *Nat. Rev. Mol. Cell Biol.* **2007***, 8*, 813.

85. Bugger, H.; Abel, E. D., Mitochondria in the diabetic heart. *Cardiovas. Res.* **2010***, 88*, 229-240.

86. Stokes, G., On the Change of Refrangibility of Light. *Philos. Trans. R. Soc.* **1852***, 142*, 463-562.

87. Frackowiak, D., The jablonski diagram. *J. Photochem. Photobiol.* **1988***, 2*, 399.

88. Valeur, B.; Berberan-Santos, M. N., A brief history of fluorescence and phosphorescence before the emergence of quantum theory. *J. Chem. Educ.* **2011***, 88*, 731-738.

89. Lakowicz, J. R. Principles of fluorescence spectroscopy. **2013**. Springer Science & Business Media.

90. Macgregor, R. B.; Weber, G., Estimation of the polarity of the protein interior by optical spectroscopy. *Nature.* **1986***, 319*, 70.

91. Marmé, N.; Knemeyer, J.-P.; Sauer, M.; Wolfrum, J., Inter-and intramolecular fluorescence quenching of organic dyes by tryptophan. *Bioconjugate Chem.* **2003***, 14*, 1133-1139.

92. Watt, R. M.; Voss Jr, E. W., Mechanism of quenching of fluorescein by anti-fluorescein IgG antibodies. *Immunochemistry.* **1977***, 14*, 533-541.

93. de Kroon, A. I., Metabolism of phosphatidylcholine and its implications for lipid acyl chain composition in Saccharomyces cerevisiae. *Biochim. Biophys. Acta-Mol. Cell Biol. L.* **2007***, 1771*, 343-352.

94. Zambrano, F.; Fleischer, S.; Fleischer, B., Lipid composition of the Golgi apparatus of rat kidney and liver in comparison with other subcellular organelles. *Biochim. Biophys. Acta, Lipids Lipid Metab.* **1975***, 380*, 357-369.

95. Griffiths, G.; Back, R.; Marsh, M., A quantitative analysis of the endocytic pathway in baby hamster kidney cells. *J. Cell Biol.* **1989***, 109*, 2703-2720.

96. Silvius, J. R., Role of cholesterol in lipid raft formation: lessons from lipid model systems. *Biochim. Biophys. Acta.* **2003***, 1610*, 174-183.

97. Lange, Y.; Ye, J.; Rigney, M.; Steck, T. L., Regulation of endoplasmic reticulum cholesterol by plasma membrane cholesterol. *J. Lipid Res.* **1999***, 40*, 2264-2270.

98. Maxfield, F. R.; Mesmin, B.; Pipalia, N.; Lamlal, T.; Eliezer, D. (**2011**). Intracellular cholesterol transport. In: Federation of American Societies for Experimental Biology.

99. Lange, Y., Disposition of intracellular cholesterol in human fibroblasts. *J. Lipid Res.* **1991***, 32*, 329-339.

100. Zheng, N.; Tsai, H. N.; Zhang, X.; Shedden, K.; Rosania, G. R., The subcellular distribution of small molecules: a meta-analysis. *Mol. Pharm.* **2011***, 8*, 1611-1618.

101. Colston, J.; Horobin, R.; Rashid-Doubell, F.; Pediani, J.; Johal, K., Why fluorescent probes for endoplasmic reticulum are selective: an experimental and QSAR-modelling study. *Biotech. Histochem.* **2003***, 78*, 323-332.

102. Lea, W. A.; Simeonov, A., Fluorescence polarization assays in small molecule screening. *Expert Opin. Drug Discov.* **2011***, 6*, 17-32.

103. Nikiforov, T. T.; Beechem, J. M., Development of homogeneous binding assays based on fluorescence resonance energy transfer between quantum dots and Alexa Fluor fluorophores. *Anal. Biochem.* **2006***, 357*, 68-76.

104. Pollard, T. D., A guide to simple and informative binding assays. *Mol. Biol. Cell.* **2010***, 21*, 4061-4067.

105. Freyer, M. W.; Lewis, E. A., Isothermal titration calorimetry: experimental design, data analysis, and probing macromolecule/ligand binding and kinetic interactions. *Method. Cell Biol.* **2008***, 84*, 79-113.

106. Nguyen, H. H.; Park, J.; Kang, S.; Kim, M., Surface plasmon resonance: a versatile technique for biosensor applications. *Sensors.* **2015***, 15*, 10481-10510.

107. Cala, O.; Guillière, F.; Krimm, I., NMR-based analysis of protein–ligand interactions. *Anal. Bioanal. Chem.* **2014***, 406*, 943-956.

108. Schlichting, I. X-ray crystallography of protein-ligand interactions. In *Protein-ligand interactions* **2005**,(pp. 155-165): Springer.

109. Nienhaus, K.; Nienhaus, G. U. Probing heme protein-ligand interactions by UV/visible absorption spectroscopy. In *Protein-Ligand Interactions* **2005**,(pp. 215-241): Springer.

110. Barre, J.; Chamouard, J.; Houin, G.; Tillement, J., Equilibrium dialysis, ultrafiltration, and ultracentrifugation compared for determining the plasma-protein-binding characteristics of valproic acid. *Clin. Chem.* **1985***, 31*, 60-64.

111. Maguire, J. J.; Kuc, R. E.; Davenport, A. P. Radioligand binding assays and their analysis. In *Receptor binding techniques* **2012**,(pp. 31-77): Springer.

112. De Jong, L. A.; Uges, D. R.; Franke, J. P.; Bischoff, R., Receptor–ligand binding assays: technologies and applications. *J. Chromatogr. B.* **2005***, 829*, 1-25.

113. Du, X.; Li, Y.; Xia, Y.-L.; Ai, S.-M.; Liang, J.; Sang, P.; Ji, X.-L.; Liu, S.-Q., Insights into protein–ligand interactions: mechanisms, models, and methods. *Int. J. Mol. Sci.* **2016***, 17*, 144.

114. Jameson, D. M.; Ross, J. A., Fluorescence polarization/anisotropy in diagnostics and imaging. *Chem. Rev.* **2010***, 110*, 2685-2708.

115. Ciulli, A. Biophysical screening for the discovery of small-molecule ligands. In *Protein-Ligand Interactions* **2013**,(pp. 357-388): Springer.

Chapter 2

Covalently-crosslinked nanodiscs for studies of membrane-disruptive peptides

2.1. Introduction

Plasma membranes of living cells represent complex and dynamic assemblies of lipids, proteins, and other biomolecules. Ever since lipid bilayers were defined as a basic structural unit of biological membranes,[1,2] model systems of various lipid compositions were created to study properties of these structures.[3] These models are designed to simplify these biological systems and facilitate their investigation. As discussed in Chapter 1, traditional model membranes include supported lipid monolayers and bilayers,[4] liposomes,[5,6] micelles,[7] bicelles,[8] and amphipathic polymers (amphipols).[9] These models have been extensively used for structural and functional studies of membrane-embedded proteins, peptides, and drugs.[10] However, the heterogeneity of many model membrane systems limits their utility for structural studies of membrane-associated molecules. Moreover, the numerous important biological processes that disrupt cellular membranes including apoptosis,[11-13] immunity,[14,15] bacterial toxins,[16,17] viral infection,[18] and protein translocation[19] provide additional challenges for studies of effects on membranes. As a more chemically-defined alternative to traditional model membranes, nanodiscs have been developed to provide nanometer-scale mimics of cellular lipid bilayers.[20-22] As shown in Figure 2.1, many of these model membranes are derived from homodimers of the Membrane Scaffold Protein 1D1 (MSP1D1),[20,23] a protein that encircles a cluster of lipids to provide lipidic discs with a well-defined chemical composition of ~126 lipids and

a bilayer area of ~4400 Å^2.[22,24] These nanodiscs enable a wide variety of structural studies of proteins integrated in lipid bilayers. Examples include OmpX,[25] BCL-XL,[26] human CYP3A4,[27] TRPV1,[28] Cytb5-CytP450,[29] and many more.[30]

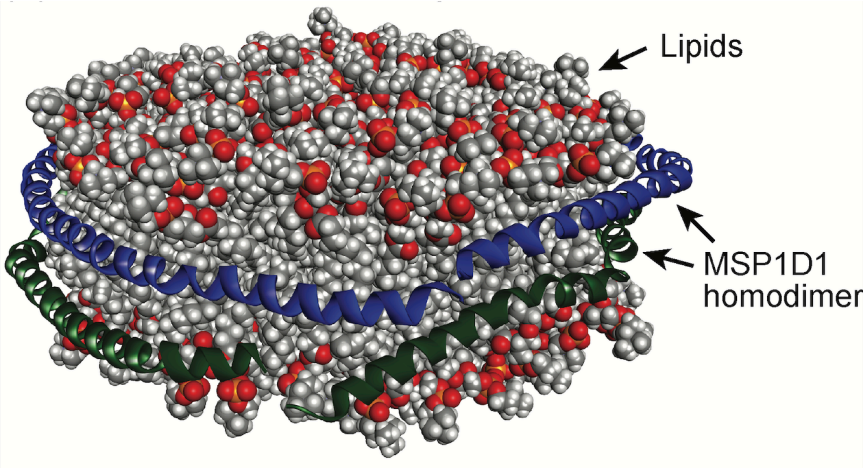

Figure 2.1. Model of an MSP1D1 lipidic nanodisc. The traditional MSP1D1 nanodisc consists of lipids held together by two membrane scaffold proteins (shown in blue and green).

Although nanodiscs are considered best in class for many types of studies of membrane proteins and peptides, they exhibit some limitations. One such limitation is their relatively low thermal stability. They disintegrate over time and can exhibit some heterogeneity in size. A contributor to this low stability and heterogeneity is the gaps between the protein belts that surround nanodiscs. These gaps may allow the escape of lipids and contribute to protein aggregation. To help overcome this issue, Wagner and co-workers developed covalently circularized nanodiscs[31] that can be prepared using the enzyme sortase. These nanodiscs beneficially exhibit greater homogeneity in size and improved stability. However, they require the non-commercially available enzyme sortase

for cyclization of a modified membrane scaffold protein, substantially increasing the complexity involved in their production and purification.

To solve this problem, we explored the addition of cysteines to the termini of the membrane scaffold protein (MSP) to generate a covalent disulfide bond. We additionally investigated crosslinking of these cysteines by alkylation to yield a more stable m-xylene (mxy) thioether. These mxy-crosslinked MSP nanodiscs were termed mxy-MSPSS_M6 nanodiscs. However, despite numerous attempts, these approaches, based on Cys-crosslinking, did not generate pure nanodiscs in high yield. Better results were obtained using a new technology based on the SpyTag/SpyCatcher system to covalently link the membrane scaffold protein. We termed this protein SpyMSP, and we termed nanodiscs assembled from this protein SpyDiscs.

We hypothesized that SpyDiscs derived from SpyMSP might be sufficiently stable to enable visualization of the effects of membrane disruptive peptides by transmission electron microscopy (TEM). To test this hypothesis, we examined incorporation of alamethicin and melittin, two natural membrane-disruptive peptides, as well as a synthetic cholesterol-linked endosome-disruptive peptide termed Chol-EDP,[32] previously reported by our laboratory (Figure 2.2). Alamethicin, the best understood of these peptides, is a 20-residue antimicrobial peptide produced by the fungus *Trichoderma viride*.[33] This peptide exhibits antimicrobial activity by forming non-specific pores in cell membranes that exhibit properties of voltage-gated channels.[34] These pores have been directly visualized by electrochemical scanning tunneling microscopy in a phospholipid matrix[35] and by atomic force microscopy in a supported lipid membrane.[36] These studies, and others,[37,38] have shown that alamethicin forms alpha-helices that predominantly self-

assemble as hexamers in membranes. These assemblies form barrel-stave channels with an outer diameter of 2.0 ± 0.3 nm. Melittin from bee venom comprises a 26-residue lytic and antimicrobial[39] pore-forming peptide.[40,41] Dye leakage[42] and computational[43] studies of melittin indicate that it forms toroidal pores of 1.3–1.5 nm, although somewhat larger pores were proposed from neutron scattering data.[44] For all of these membrane-active peptides, direct visualization of pores by TEM has not been previously reported. We demonstrate here that in contrast to unmodified MSP1D1 nanodiscs, more thermally stable SpyDiscs enable visualization by TEM of nanometer-diameter pores induced by these membrane-active peptides, suggesting that SpyDiscs may have general utility for studies of membrane-disruptive peptides and proteins. In this chapter, I present the initial design, analysis, and application of disulfide linked MSPSS_M6 nanodiscs and covalently linked mxy_MSPSS_M6 nanodiscs, their limitations, and the subsequent development of SpyDiscs as an improved approach for covalent crosslinking of these model membranes.

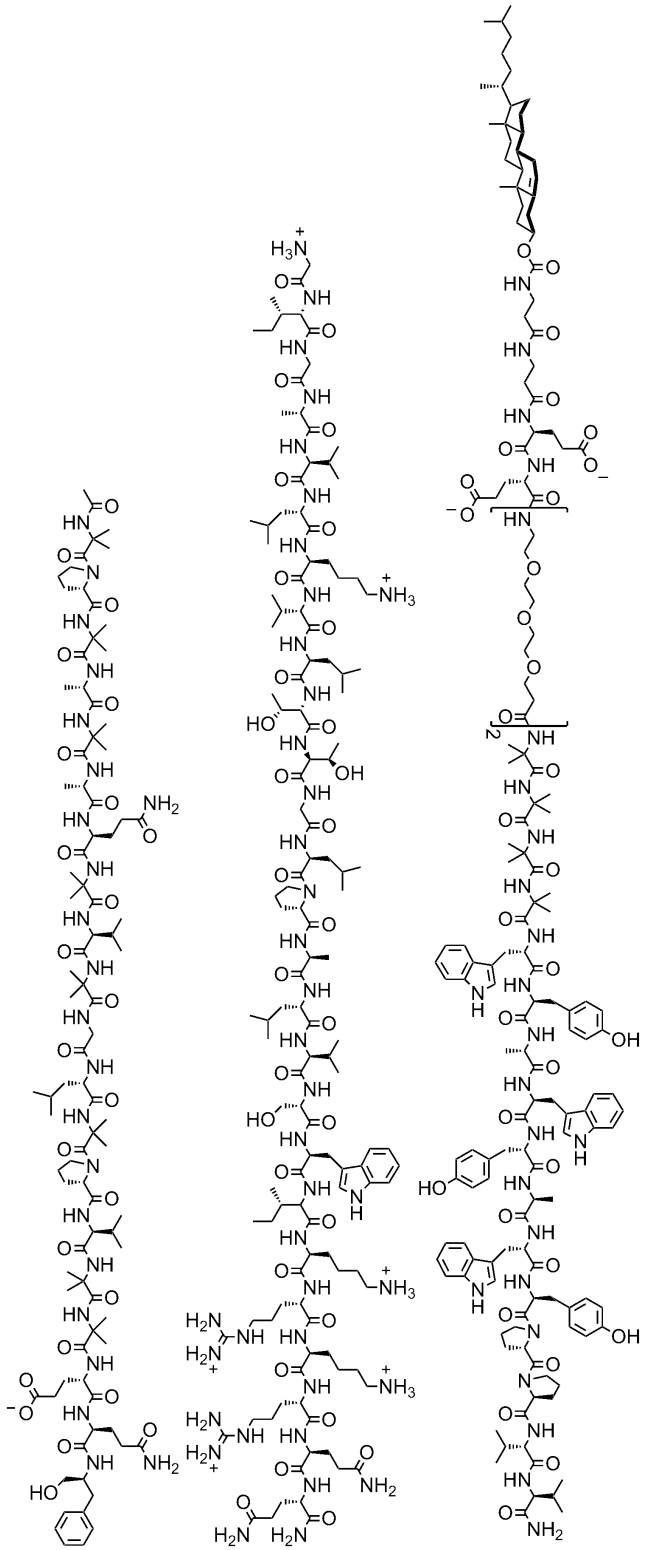

Figure 2.2. Structures of membrane-active peptides. Alamethicin and melittin are natural products, whereas Chol-EDP is a synthetic peptide.

2.2. Disulfide crosslinking of a membrane scaffold protein for stabilization of nanodiscs

2.2.1. Design of the MSPSS_M6 protein

To close the gaps predicted to exist between the N-and C-termini when the MSP surrounds lipids in traditional nanodiscs, we designed a new MSP termed MSPSS_M6 (Figure 2.3). This protein includes an additional 14 amino acid linker segment from human Apolipoprotein A-1 (ApoA1) of high density lipoprotein (HDL),[45] which was previously used to design MSP1D1.[22] We envisioned cyclizing MSPSS_M6 by oxidizing cysteines that were additionally included at the N-and C-termini to form a disulfide bond. This protein was overexpressed in *E. coli*, purified on Ni-NTA resin, cleaved with TEV protease, and analyzed by SDS-PAGE (Figure 2.4) and mass spectrometry (Figure 5.2, Appendix A).

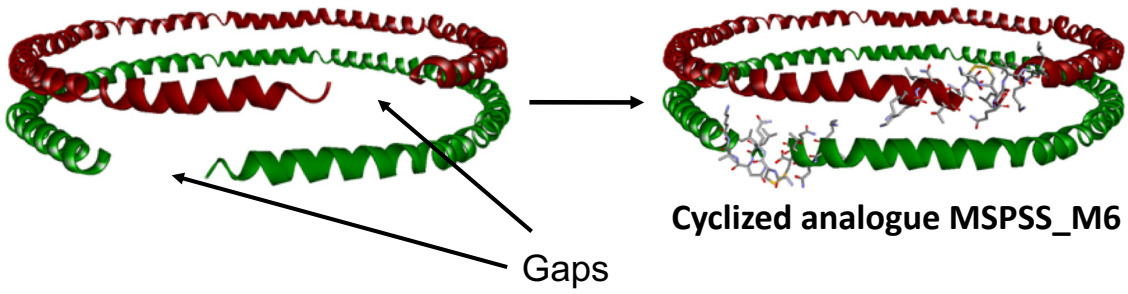

Figure 2.3. Comparison of a structure of the MSP1D1 homodimer (left) with a model of MSPSS_M6 (right) cyclized by formation of cysteine disulfides.

(A) Analysis of Ni-NTA purification of MSPSS_M6 by SDS-PAGE

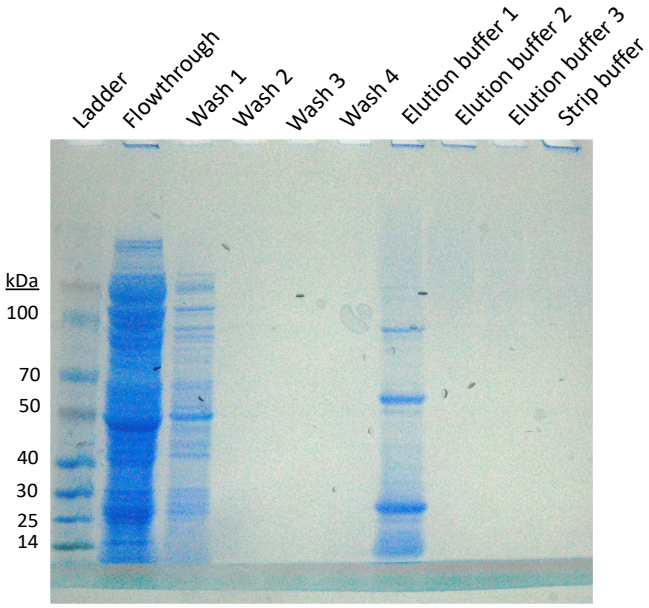

(B) Analysis of MSPSS_M6 by SDS-PAGE after TEV cleavage

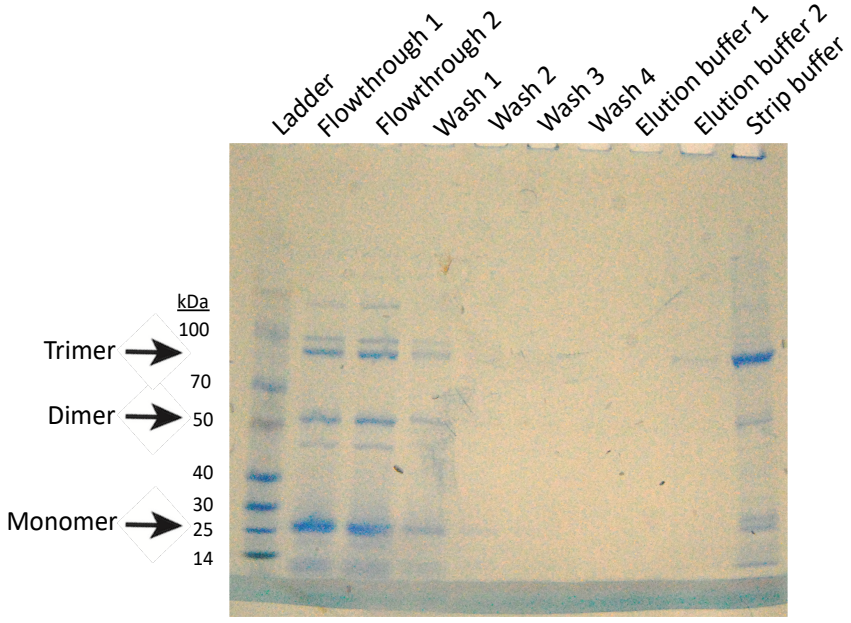

Figure 2.4. Analysis of MSPSS_M6 during purification on Ni-NTA resin (A) and after cleavage by TEV protease (B) by SDS-PAGE.

2.2.2. MSPSS_M6 forms nanodiscs as imaged by TEM

To investigate nanodiscs derived from MSPSS_M6, this protein was assembled with POPC lipids and purified by size-exclusion chromatography (SEC). As shown in Figure 2.5, imaging by transmission electron microscopy (TEM) revealed that this protein can form discoidal structures of 14 ± 3 nm in diameter.

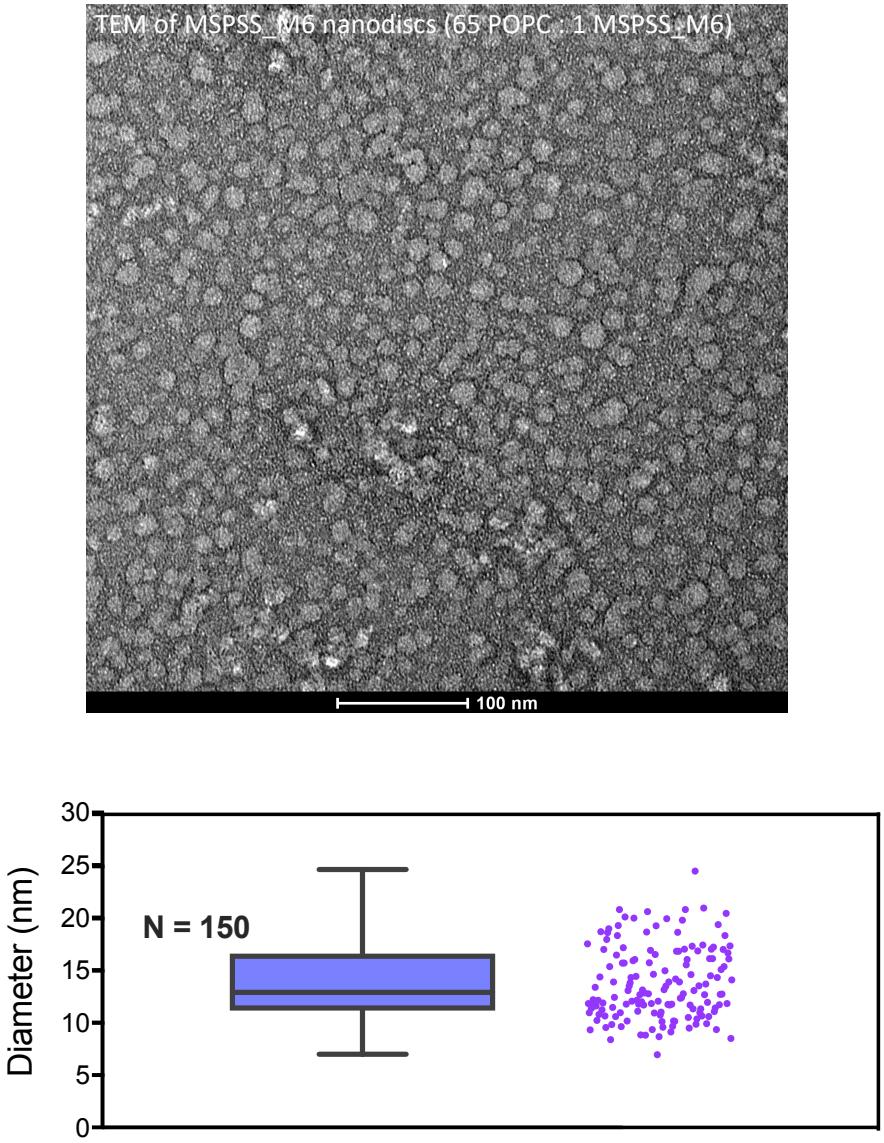

Figure 2.5. Measurement of sizes of nanodiscs by TEM. Imaging of MSPSS_M6-POPC nanodiscs revealed discoid structures with a diameter of 13.8 ± 3.4 nm (range = 17.7 nm). The box-and-whisker plot gives the distribution of diameters of nanodiscs. All nanodiscs are reconstituted with POPC lipids. 'N' is the number of nanodiscs measured.

2.2.3. Comparison of the stabilities of MSP1D1 and MSPSS_M6 nanodiscs

2.2.3.1. Analysis of stability by temperature-dependent circular dichroism spectroscopy

Circular dichroism (CD) spectroscopy was used to compare the thermal stability of traditional MSP1D1 nanodiscs with disulfide-linked MSPSS_M6 nanodiscs. This spectroscopic method is commonly used to investigate the secondary structure of proteins. For example, β-sheets exhibit a characteristic minimum at 215 nm (n→π*) and a maximum at 198 nm (π→π*), whereas alpha helices exhibit two double minima at 208 (π→π*) and 220 nm (n→π*), with a stronger maximum at 191-193 nm (π→π*). In contrast, random coils in proteins tend to exhibit a maxima and minima essentially opposite from these features in α-helical and β-sheet structures. As seen in Figure 2.6, in both traditional and modified nanodiscs, a spectral signature consistent with the formation of alpha helices was observed. However, in temperature-dependent studies, the CD spectra of disulfide-linked nanodiscs had a much lower minima at 10 °C compared to the traditional nanodiscs, indicating higher helicity of the disulfide linked MSP compared to MSP1D1. Moreover, spectra at 70 °C showed that the modified membrane scaffold protein still retains substantial helical structure, which appeared to be lost in the traditional MSP.

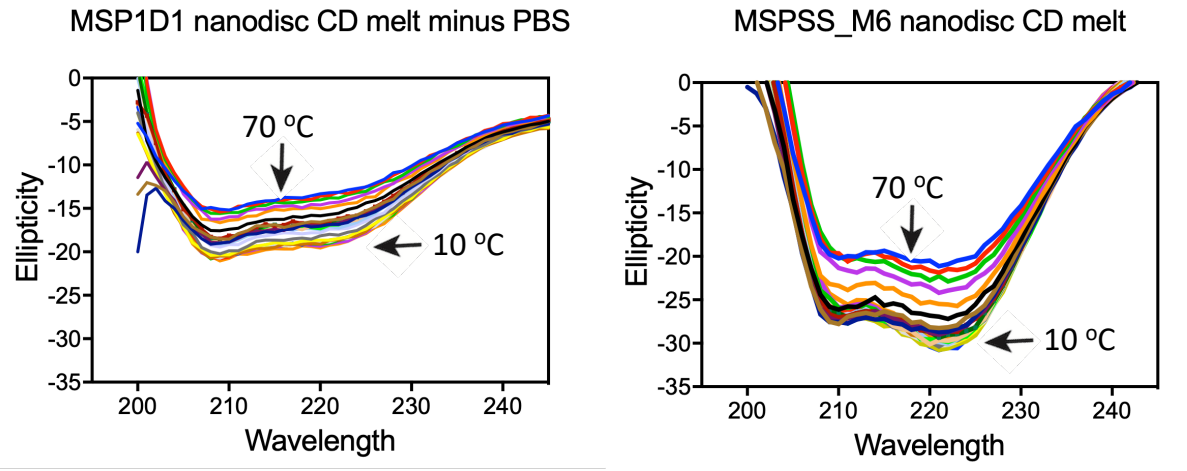

Figure 2.6. Comparison of CD spectra of traditional MSP1D1 nanodiscs and MSPSS_M6 nanodiscs after assembly with POPC lipids. Nanodiscs made with MSPSS_M6 protein were more thermally-stable than the MSP1D1 nanodiscs.

2.2.3.2. Comparison of nanodisc stability by size exclusion chromatography

The TEM images and CD data showed that MSPSS_M6 nanodiscs are well-defined and are more stable than MSP1D1 nanodiscs at higher temperatures. To test the stability of the disulfide-linked nanodiscs over time, traditional MSP1D1 nanodiscs and MSPSS_M6 nanodiscs were stored at 4 °C and SEC readings were obtained every week for three weeks. As shown in Figure 2.7, the disulfide linked nanodiscs were much more stable after 3 weeks at 4 °C compared to MSP1D1 nanodiscs.

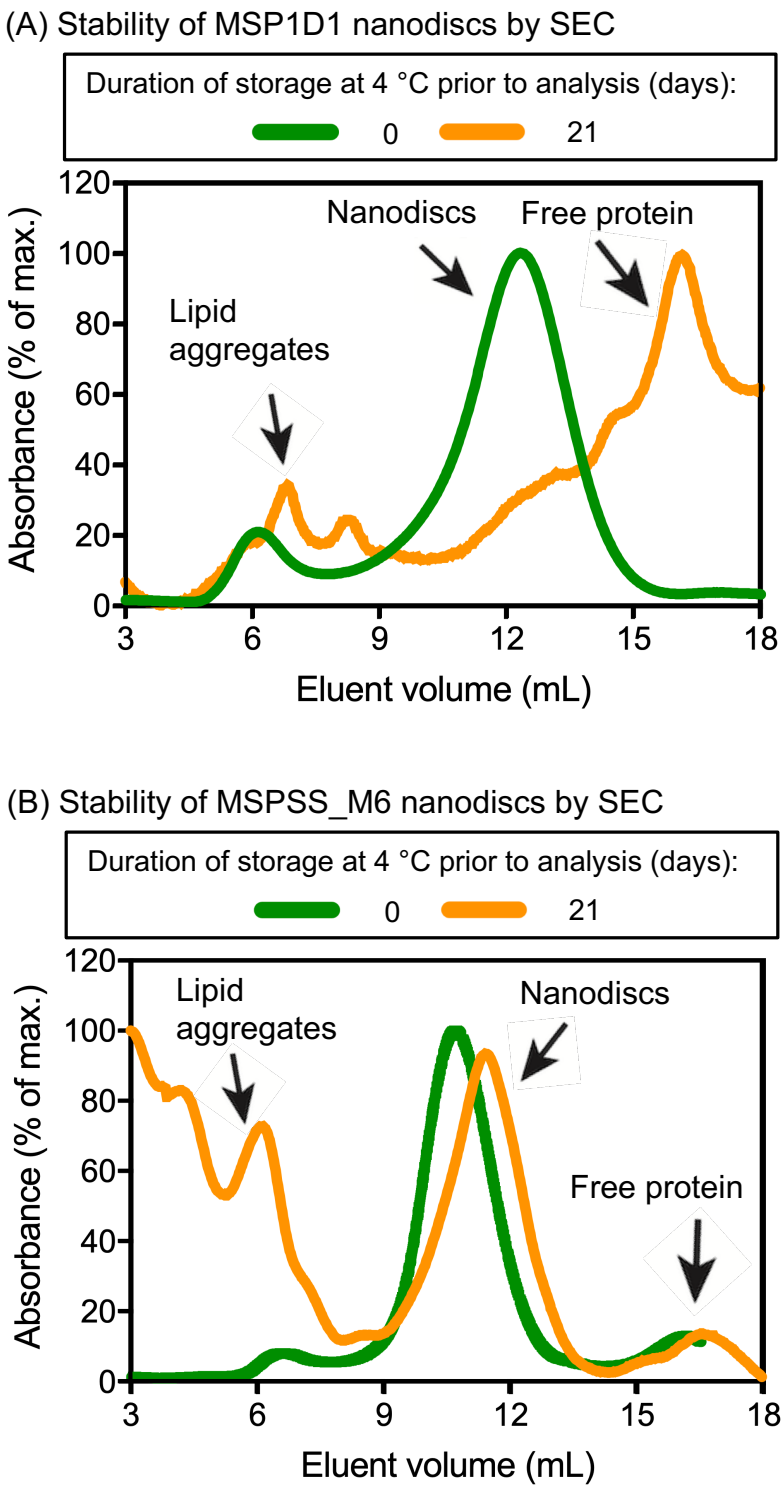

Figure 2.7. Stability of MSP1D1 and MSPSS_M6 nanodiscs at 4 °C. Only the MSPSS_M6 nanodiscs could be observed as a defined peak after 3 weeks.

Although nanodiscs formed with MSPSS_M6 protein are more thermally stable, this protein was observed to form higher oligomers (Figure 2.4), with a predominant dimer visible by mass spectrometry (Figure 5.2, Appendix A), even under mass spectrometry-reducing conditions, consistent with cysteine disulfide exchange. This phenomenon may also contribute to the somewhat high variation observed in the sizes of these nanodiscs (Figure 2.5).

2.3. Attempts to crosslink MSP cysteines as meta-xylene thioethers to avoid disulfide exchange

As an approach to avoid potential disulfide exchange in MSPSS_M6 nanodiscs, we envisioned cross-linking the cysteines of MSPSS_M6 with meta-dibromoxylene. This xylene linkage might additionally allow the study of proteins that include Cys residues, which could be incompatible with disulfide-linked nanodiscs. To generate these proteins, TEV cleaved MSPSS_M6 protein was overexpressed in *E.coli*, treated with meta-dibromoxylene to afford a protein termed mxy_MSPSS_M6. Characterization of this protein by mass spectroscopy revealed the correct molecular species (Figure 5.3, Appendix A) and no presence of higher oligomers.

2.3.1. mxy_MSPSS_M6 forms nanodiscs as imaged by TEM

The mxy_MSPSS_M6 protein was assembled with POPC lipids and nanodiscs were purified by size-exclusion chromatography. As shown in Figure 2.8, imaging by TEM revealed that this protein forms discoidal structures of 14 ± 3 nm in diameter.

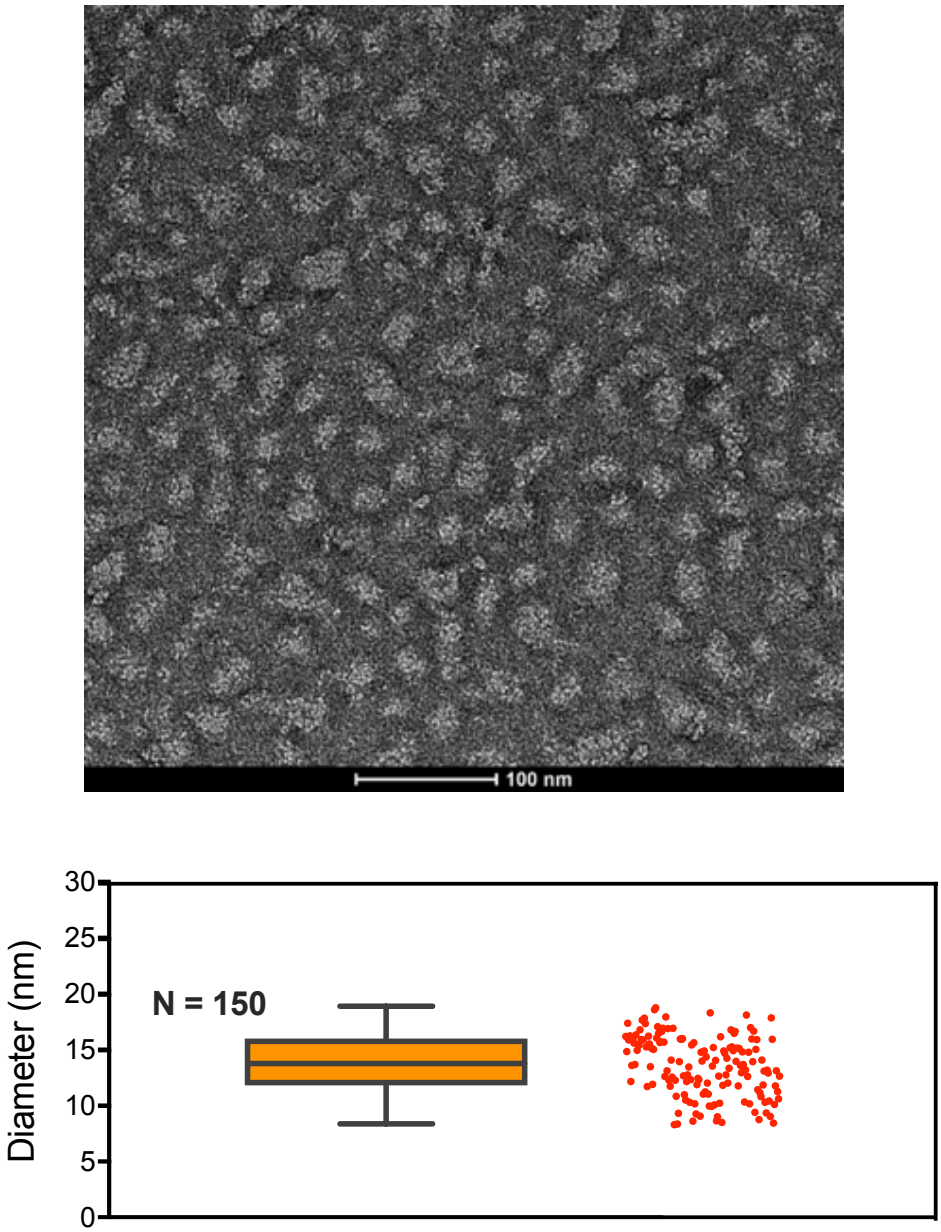

Figure 2.8. Measurement of the sizes of nanodisc by TEM. Imaging of mxy_MSPSS_M6-POPC nanodiscs revealed discoid structures with a diameter of 13.6 ± 2.7 nm (range = 10.5 nm). The box-and-whisker plot gives the distribution of diameters of nanodiscs (below). All nanodiscs are reconstituted with POPC lipids. 'N' is the number of nanodiscs measured.

2.3.2. Characterization of mxy_MSPSS_M6 protein by HPLC

Although covalently crosslinking in mxy_MSPSS_M6 nanodiscs appeared to solve the problem of disulfide exchange by preventing the formation of higher oligomers (Figure 5.3, Appendix A), analysis by HPLC revealed that this approach did not yield pure proteins for production of nanodiscs (Figure 2.9). Additionally, the mxy_MSPSS_M6 protein was obtained in low yield (~ 4 mg/L) after cross-linking. Due to these limitations, we decided to investigate alternative approaches for cyclization of the membrane scaffold protein without the use of Cys residues.

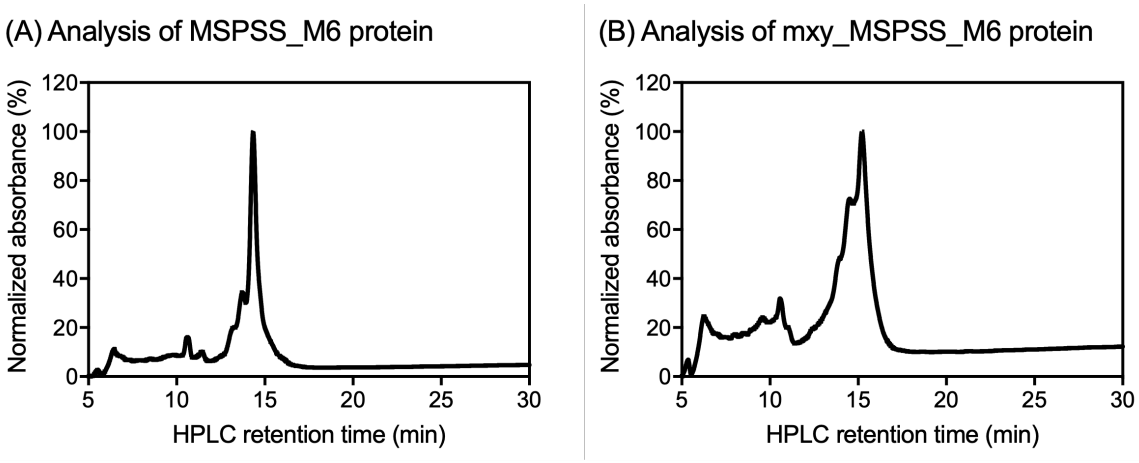

Figure 2.9. Analysis of MSPSS_M6 and mxy_MSPSS_M6 proteins by reverse-phase HPLC. Multiple peaks were observed in both cases, but higher levels of impurities were observed for mxy_MSPSS_M6.

2.4. Covalently cross-linked SpyDiscs

As an alternative approach, we employed a recent technology based on the SpyTag/SpyCatcher system. Using this system, we designed a protein termed SpyMSP and SpyDiscs, as nanodiscs derived from this protein. SpyMSP was constructed by fusing a variant of the protein SpyCatcher to the N-terminus and the peptide SpyTag[46,47] to the C-terminus of MSP1D1. These fusion elements were originally isolated from the

immunoglobin-like collagen adhesion domain (CnaB2) of the bacterium *Streptococcus pyogenes*. In CnaB2, an internal isopeptide bond[48] spontaneously forms between amino acids Lys31 and Asp117, providing exceptionally high protein stability.[49-51] Based on this observation, split engineering was used to design a 13 amino acid peptide termed SpyTag that binds with high affinity (K_d = 0.2 μM) to its partner protein SpyCatcher, where it rapidly forms an analogous isopeptide amide bond (Figure 2.10).[47] Fusion of enzymes at their N- and C-termini to SpyTag and SpyCatcher has been shown to enhance their thermal stability through covalent circularization.[52-56]

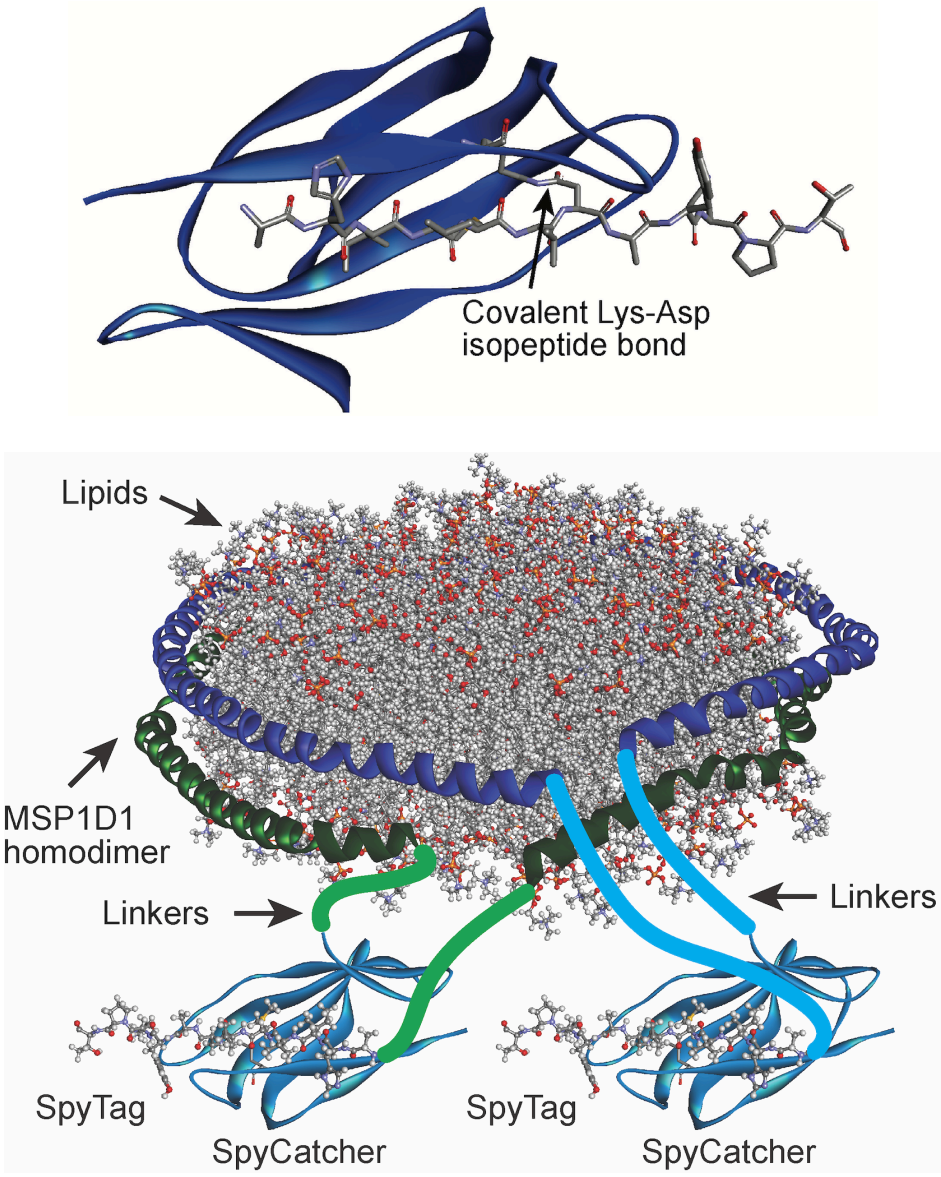

Figure 2.10. Structure of the SpyCatcher protein (top, blue ribbons) covalently linked to the SpyTag peptide (sticks, PDB 4MLS[57]). Design of SpyDiscs by fusion of MSP1D1 to these elements (bottom).

2.4.1. Design of covalently cross-linked SpyMSP

To prepare cyclized SpyMSP, MSP1D1 was flanked by a minimized SpyCatcherΔN1[57] protein and SpyTag. Using a molecular model of ApoA1 of HDL[45] to design a linker segment, a model of a MSP1D1 nanodisc,[58] and the structure of SpyCatcher bound to SpyTag,[57] we designed the SpyMSP protein sequence shown in

Figure 2.11. In this construct, an N-terminal hexahistadine tag, linker, and TEV protease cleavage site (ENLYFQG), similar to that used for expression of MSP1D1, was fused through a GlySer linker to the previously reported SpyCatcherΔN1 protein sequence. Modeling suggested that to avoid potentially detrimental effects of SpyCatcher on the helical structure of MSP1D1, a downstream linker of approximately 20 amino acids was needed, and this was accomplished by the addition of a GlySerGlyGlySerGly linker followed by 14 amino acids derived from ApoA1 that were predicted to form a contiguous helical segment upstream of the membrane scaffold protein without detrimentally affecting the packing of the lipids within the nanodisc. This membrane scaffold protein was followed by another GlySerGlyGlySerGly linker, which was in turn fused to the SpyTag peptide at the C-terminus. Purification of SpyMSP, and treatment with TEV protease, allowed production of covalently cyclized SpyMSP (24-346). To examine the importance of formation of a covalent isopeptide bond in SpyDiscs, we additionally prepared a mutant SpyMSP D340A protein where the Asp at residue 7 of the SpyTag peptide (residue 340 in the full-length protein) was mutated to Ala to block formation of this bond (highlighted in Figure 2.11). This D340A mutation has been previously used as a control in other studies of the SpyTag peptide.[47,52,53]

His tag, TEV cleavage site, and Gly-Ser linker (1-26):

MGYYHHHHHHDYDIPTT*ENLYFQG*SG

SpyCatcher∆N1 protein and Gly-Ser linker (27-124):

DSATHIKFS**K**RDEDGKELAGATMELRDSSGKTISTWISDGQVKDFYLYPGKYTFVETAAPDG

YEVATAITFTVNEQGQVTVNGKATKGDAHIGSGGSG

Apo A1 leader peptide and MSP1D1 protein (126-327):

QLNLKLLDNWDSVTSTFSKLREQLGPVTQEFWDNLEKETEGLRQEMSKDLEEVKAKVQPYL

DDFQKKWQEEMELYRQKVEPLRAELQEGARQKLHELQEKLSPLGEEMRDRARAHVDALRT

HLAPYSDELRQRLAARLEALKENGGARLAEYHAKATEHLSTLSEKAKPALEDLRQGLLPVLE

SFKVSFLSALEEYTKKLNTQ

Gly-Ser Linker and SpyTag peptide (328-346):

GSGGSGAHIVMV**D**AYKPTK

Figure 2.11. Sequence of SpyMSP (1-346). Design features are listed above standard amino acid abbreviations. The TEV protease cleavage site is shown in italics, where cleavage occurs between Gln23 and Gly24. The reactive Lys36 from SpyCatcher and Asp340 from SpyTag that form an isopeptide amide bond are shown in bold. GlySer linker sequences are underlined. In SpyMSP D340A, where isopeptide bond formation is blocked, Asp340 is mutated to Ala.

2.4.2. Characterization of SpyMSP and SpyMSP D340A proteins

Both the SpyMSP and SpyMSP D340A proteins could be readily overexpressed in *E. coli* in high yields (30–35 mg/L). These proteins were purified on Ni-NTA resin and cleaved with TEV protease to generate SpyMSP (24-346) and SpyMSP D340A (24-346). Analysis by SDS-PAGE (Figure 2.12), HPLC (Figure 2.13), and mass spectrometry

(Figure 2.13) demonstrated that these proteins can be isolated in >95% purity, and SpyMSP (24-346) forms a covalent isopeptide bond.

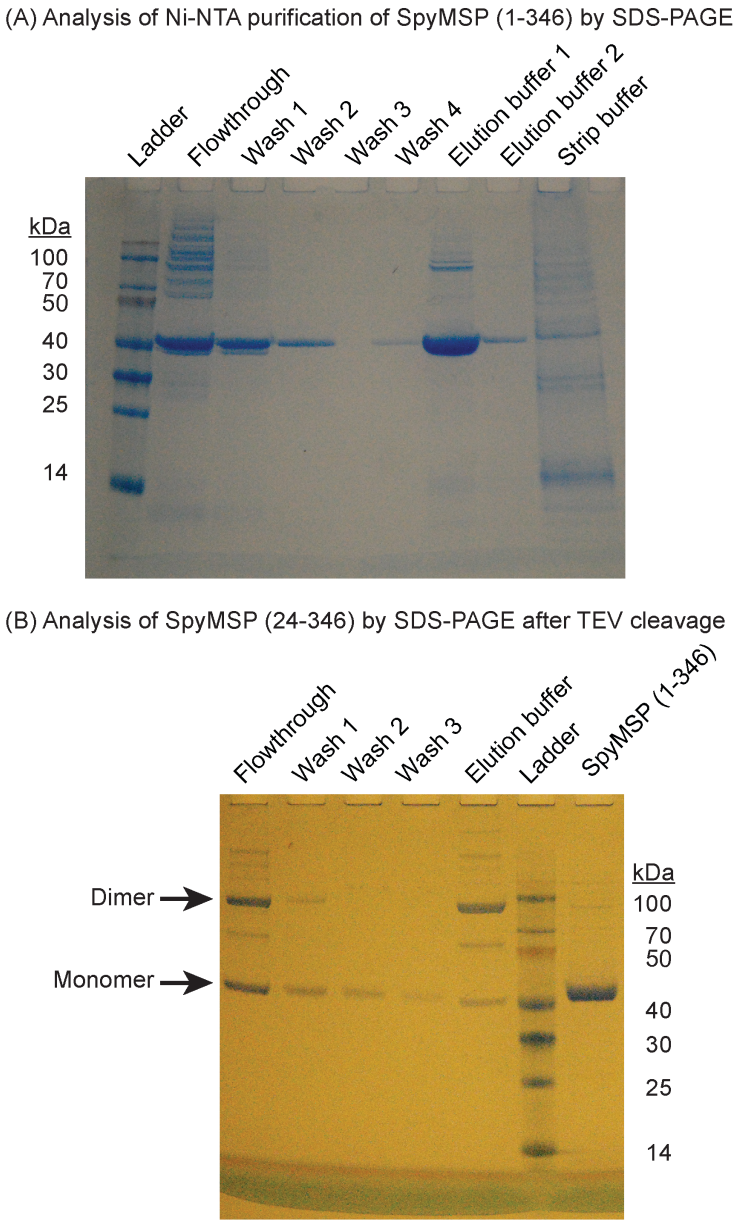

Figure 2.12. Analysis of SpyMSP during purification on Ni-NTA resin (A) and after cleavage by TEV protease (B) by SDS-PAGE.

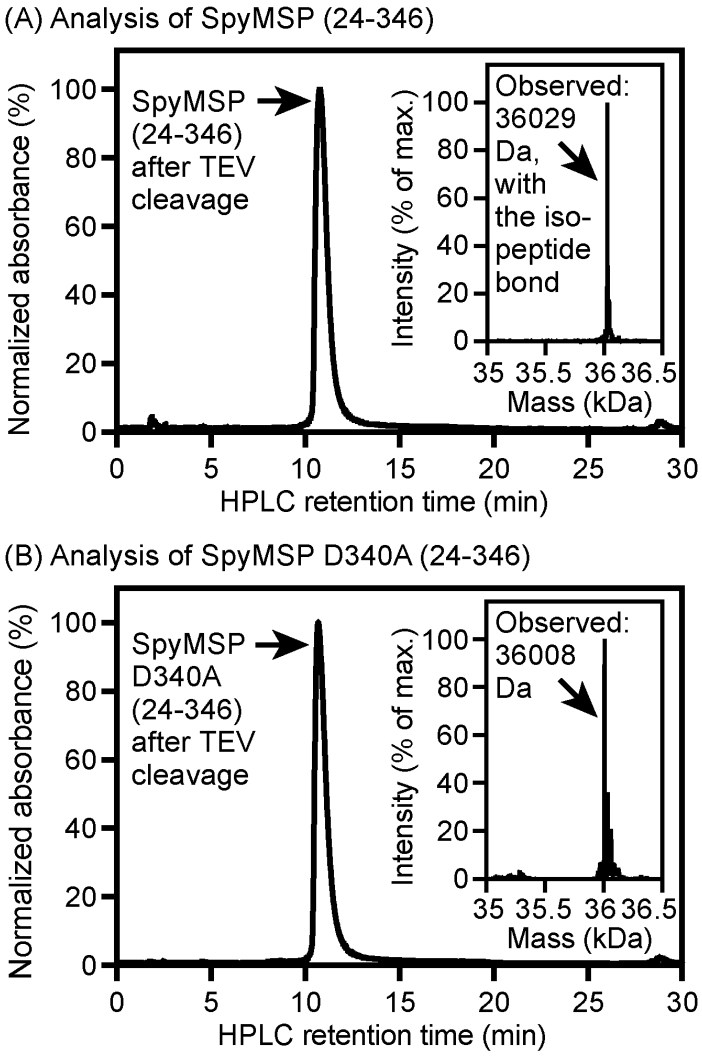

Figure 2.13. Characterization of SpyMSP proteins after purification on Ni-NTA resin followed by cleavage with TEV protease. Analysis by reverse-phase HPLC revealed single peaks of high purity. In panel A, SpyMSP (24-346) was found to have a mass of 36029 Da (inset). The cyclized product with an isopeptide bond has a theoretical MW of 36031 Da. In panel B, SpyMSP D340A (24-346) exhibited a mass of 36008 Da (inset), with a theoretical MW of 36005 Da.

2.4.3. Visualization of SpyDiscs and D340A SpyDiscs by TEM

For comparison with SpyMSP and SpyMSP D340A, MSP1D1 was overexpressed, purified, and cleaved with TEV protease as previously reported.[23] These proteins were assembled with POPC lipids and nanodiscs were purified by size-exclusion chromatography (Figure 2.14).

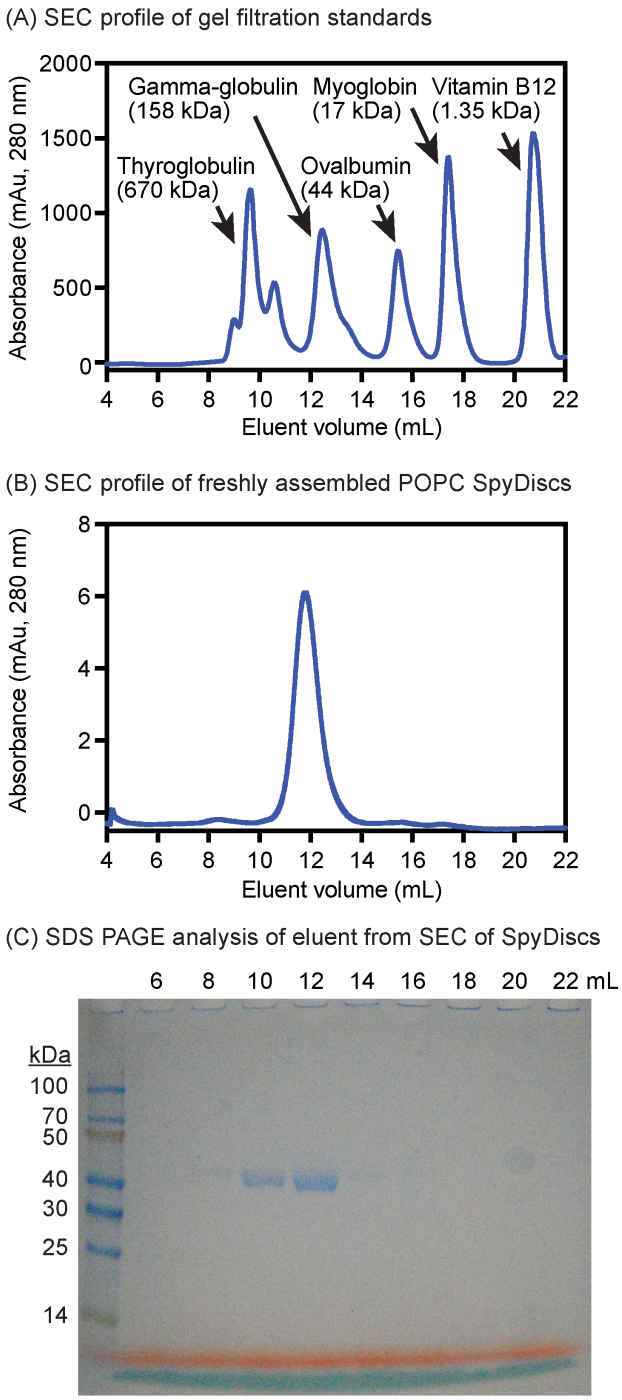

Figure 2.14. Panels A and B: SEC profiles of protein size standards (A) and POPC SpyDiscs (B) purified on a superdex 200 10/300 column (GE Healthcare). Reference samples (Biorad #1511901) were thyroglobulin, bovine gamma-globulin, chicken ovalbumin, equine myoglobin, and vitamin B12 (MW 1,350-670,000 g/mol, pI 4.5-6.9). Panel C: Analysis of fractions shown in panel B by SDS-PAGE, showing SpyMSP associated with SpyDisc fractions isolated by SEC.

As shown in Figure 2.15, imaging by transmission electron microscopy (TEM) revealed that all of these proteins form discoidal structures of ~ 12 nm in diameter.

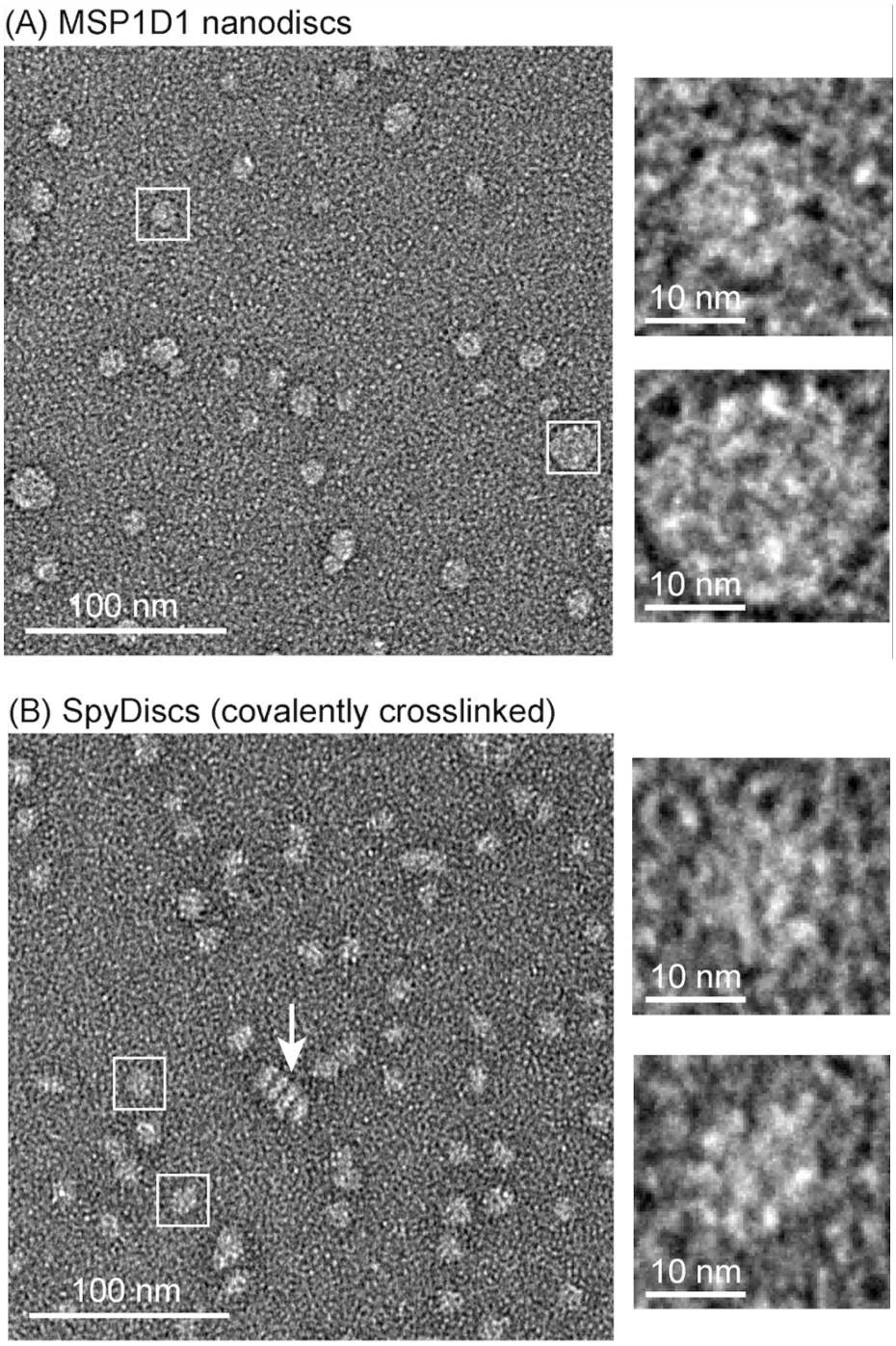

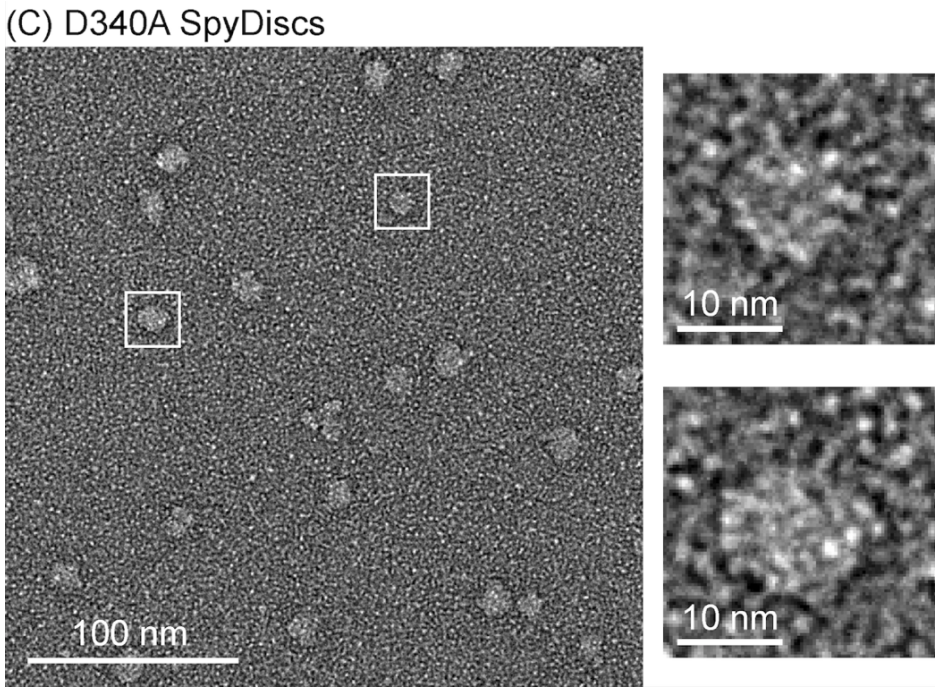

Figure 2.15. Imaging of MSP1D1 nanodiscs, SpyDiscs, and D340A SpyDiscs by TEM after assembly with POPC lipids. Representative individual nanodiscs framed in white boxes are shown in expansions on the right. In B, the arrow points at a stack of nanodiscs in a face-to-face geometry.

2.4.4. Measurement of SpyDiscs and D340A SpyDiscs nanodiscs

Measurement of the variance in sizes by TEM (Figure 2.16, using ImageJ software)[59] and dynamic light scattering (DLS, Figure 2.17) revealed that the covalently crosslinked SpyDiscs (diameter = 12 ± 2 nm) were more homogeneous than D340A SpyDiscs (diameter = 13 ± 3 nm) or MSP1D1 nanodiscs (diameter = 10 ± 3 nm), consistent with other studies of circularized nanodiscs.[31] In some images, stacks of SpyDiscs in a face-to-face geometry were observed, as previously described by others.[60]

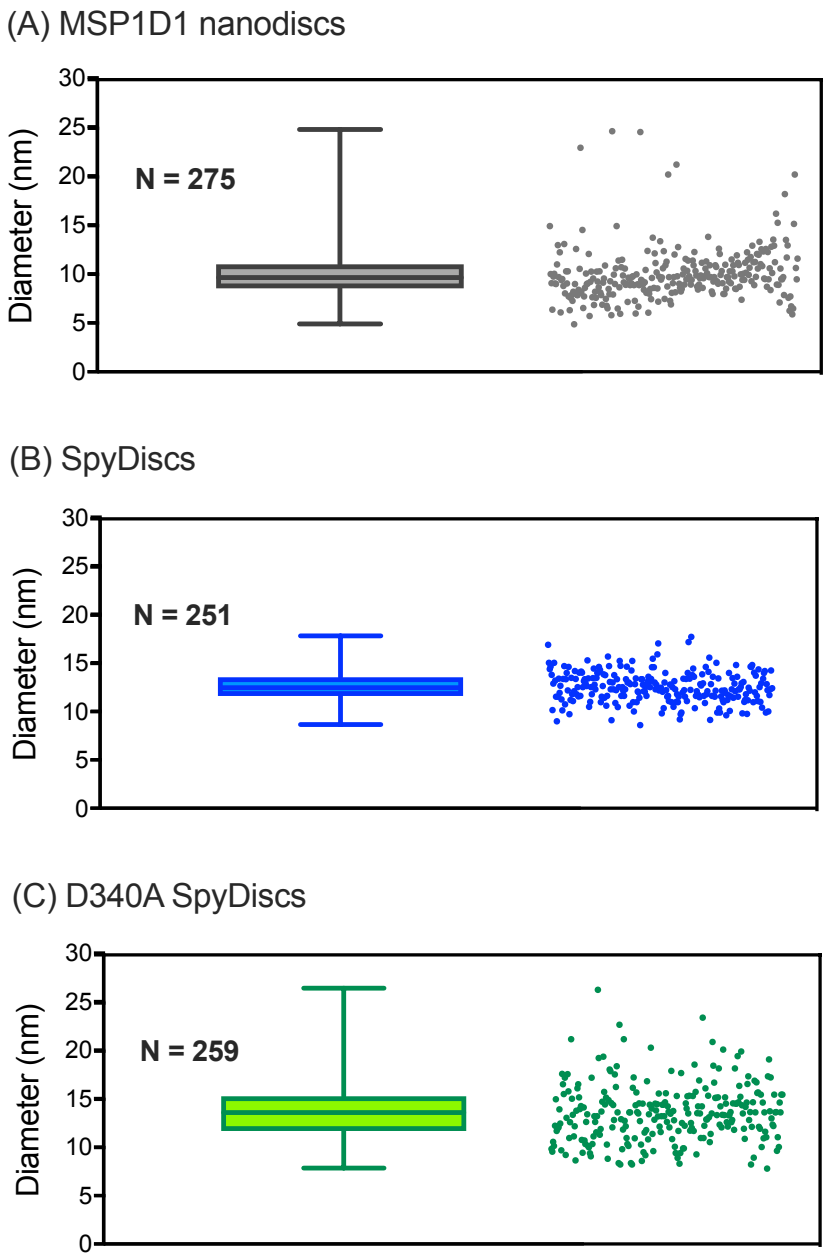

Figure 2.16. Measurement of the sizes of nanodisc by TEM. Panel A: MSP1D1 nanodiscs (10.0 ± 2.6 nm, range = 19.8 nm). Panel B: SpyDiscs (12.6 ± 1.6 nm, range = 9.2 nm). Panel C: D340A SpyDiscs (13.6 ± 3.0 nm, range = 18.6 nm). The box-and-whisker plot gives the distribution of diameters of nanodiscs. All nanodiscs are reconstituted with POPC lipids. 'N' is the number of nanodiscs measured.

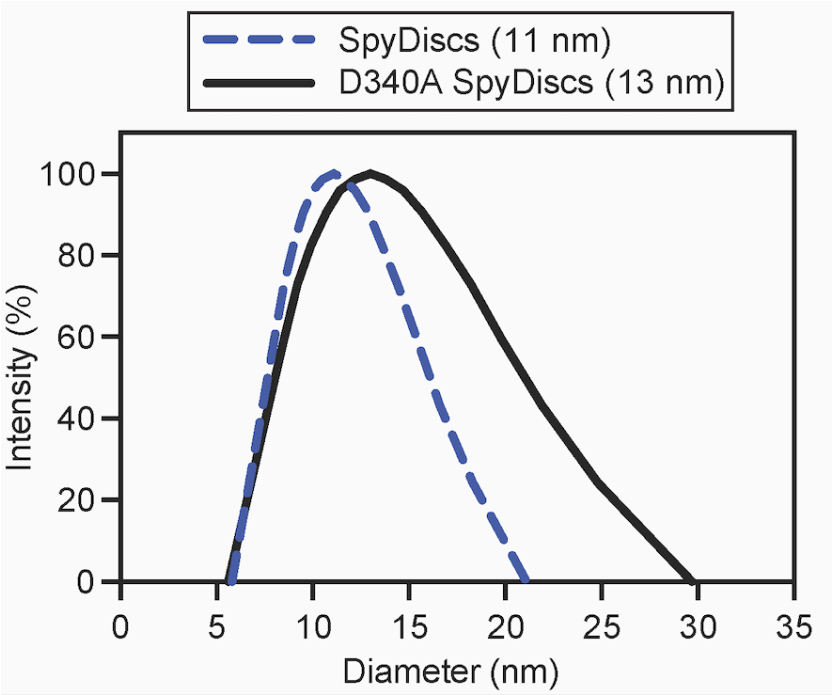

Figure 2.17. Analysis of hydrodynamic diameters of SpyDiscs and D340A SpyDiscs by DLS.

2.4.5. Analysis of the stability of SpyDiscs and D340A SpyDiscs

2.4.5.1. Thermal stability by circular dichroism (CD)

To examine the relative stability of SpyDiscs compared to MSP1D1 nanodiscs, CD spectroscopy was used to investigate changes in the secondary structure as a function of temperature. As shown in Figure 2.18, phase transition temperatures (T_m) were measured by fitting the temperature-dependent molar ellipticity at 222 nm, a measure of protein helicity, to a Boltzmann sigmoidal model. In these studies, MSP1D1-POPC nanodiscs exhibited the lowest overall helicity, as evidenced by the most positive molar ellipticity at 222 nm, and the lowest T_m of 58 °C. As predicted, the covalently crosslinked SpyDiscs exhibited the greatest helicity and the highest T_m of > 75 °C, whereas the D340A mutant lacking the isopeptide bond exhibited intermediate stability and helicity with a T_m

of 69 °C. These results suggest that the non-covalent association of SpyTag with SpyCatcher in this D340A mutant offers a substantial degree of stabilization in these complexes, but formation of the isopeptide bond provides the greatest thermal stability.

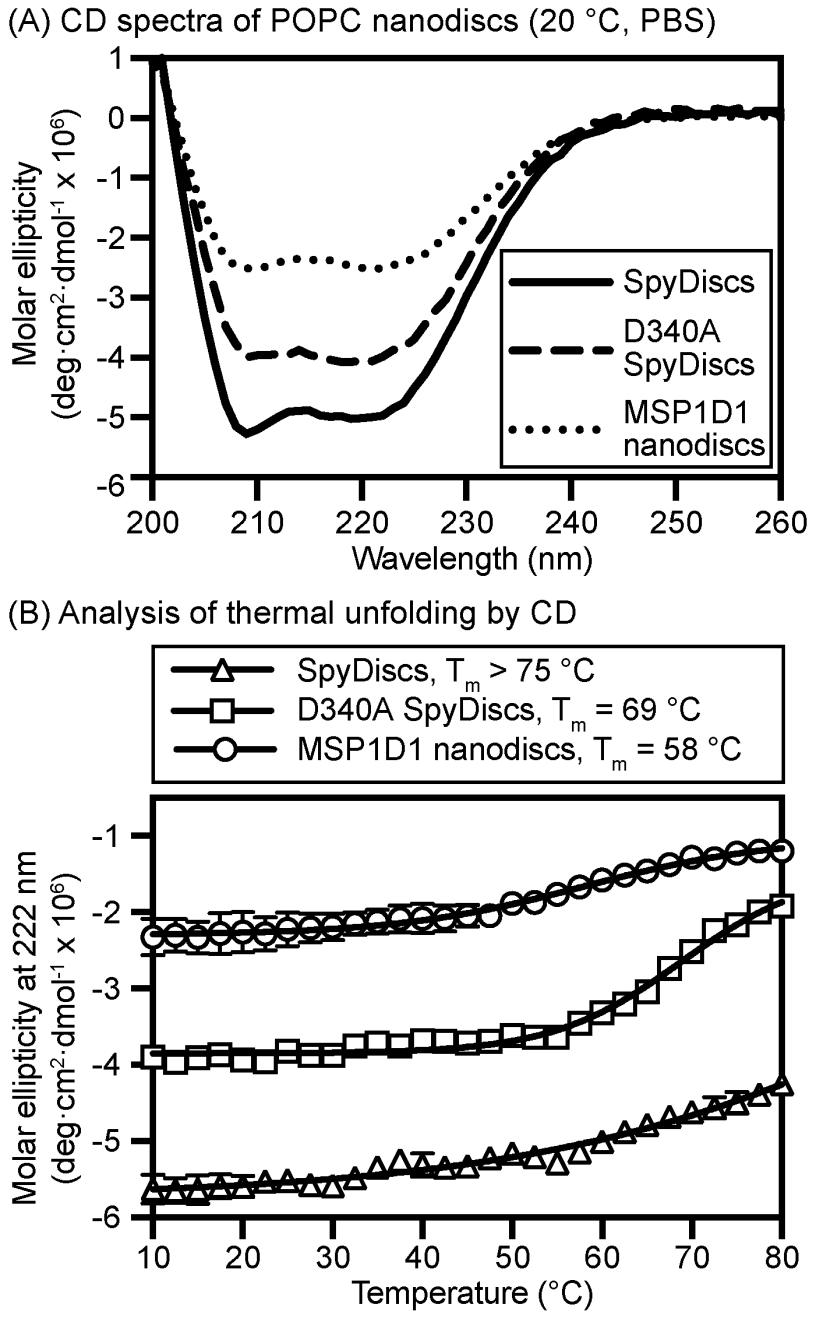

Figure 2.18. Circular dichroism spectra of POPC nanodiscs at 20 °C (A) and analysis of their thermal unfolding (T_m) by CD at 222 nm to monitor changes in helical secondary structure (B). SpyDiscs exhibit the greatest overall helicity and the highest T_m of > 75 °C in PBS (pH 7.4).

2.4.5.2. Stability of POPC nanodiscs by SEC upon storage at 4 °C

To further compare the stability of POPC nanodiscs, we analyzed decomposition by size-exclusion chromatography after continuous storage at 4 °C. As shown in Figure 2.19, MSP1D1 nanodiscs begin to disintegrate around week 3 to form lipid aggregates and free protein, were ~50% of the mixture at week 5, and they were only minor components of the mixture by week 10. In contrast, SpyDiscs maintain > 80% integrity after storage at 4 °C for 10 weeks. Consistent with the results observed from the thermal melt experiments, the D340A SpyDiscs exhibited intermediate stability. They were substantially more stable than MSP1D1 nanodiscs, but some decomposition was observed around week 6, further establishing the importance of the covalent isopeptide to maximize the stability of SpyDiscs.

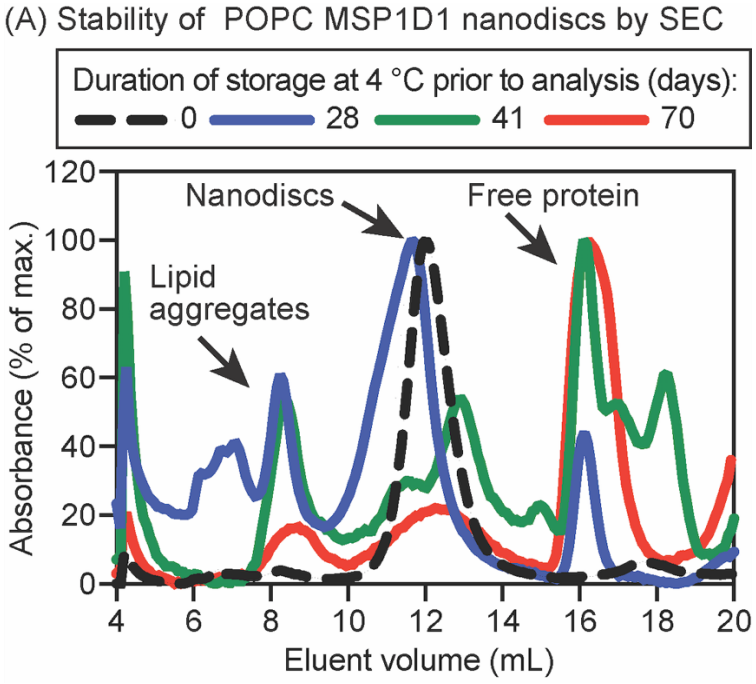

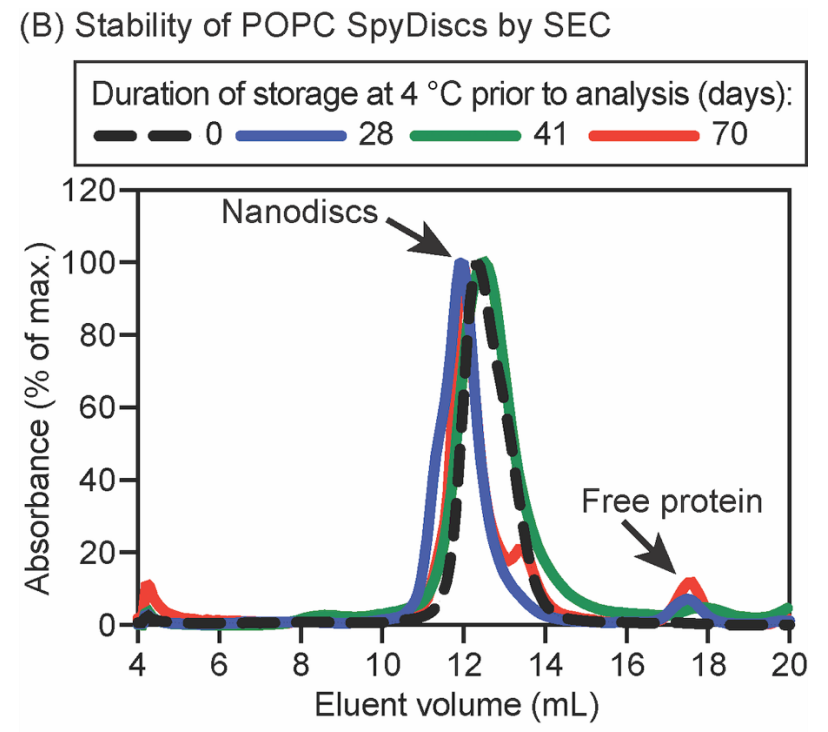

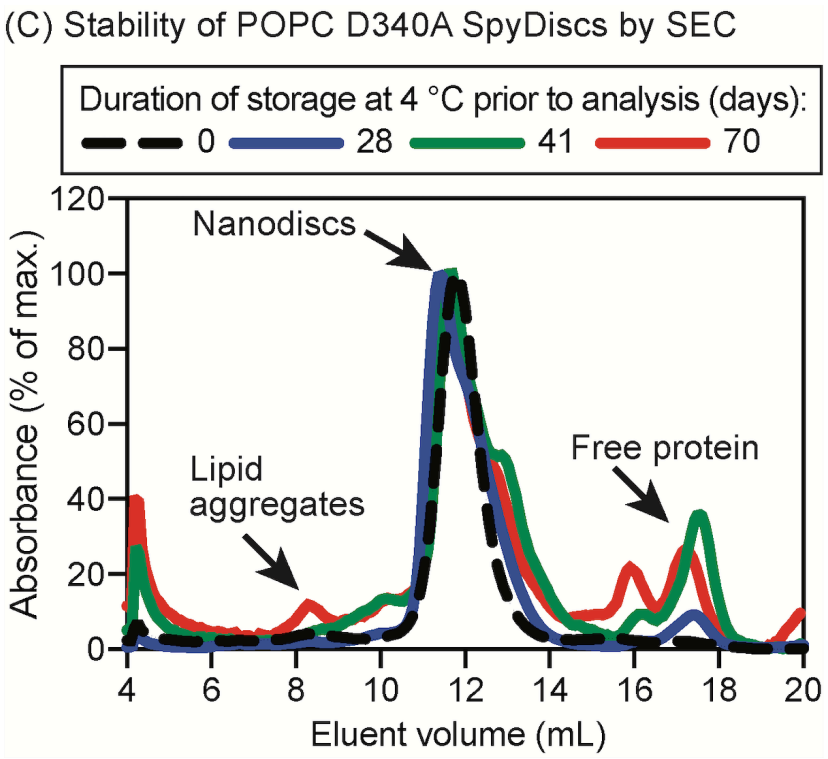

Figure 2.19. Stability of POPC MSP1D1 nanodiscs (A), SpyDiscs (B), and D340A SpyDiscs (C) over 0–10 weeks at 4 °C. Only SpyDiscs maintained >80% integrity after 10 weeks.

2.4.5.3. Stability of DMPC nanodiscs by SEC upon storage at 22 °C and 37 °C

DMPC nanodiscs were analyzed after storage at 22 °C and 37 °C. These samples were examined at different timepoints over four weeks. The stability of these sample was evaluated by comparing peaks corresponding to nanodiscs, lipid aggregates and free protein. These studies revealed that among the DMPC nanodiscs stored at 22 °C (Figure 2.20) and 37 °C (Figure 2.21), covalently-crosslinked SpyDiscs exhibited enhanced stability compared to the non-covalent D340A SpyDiscs and MSP1D1 nanodiscs.

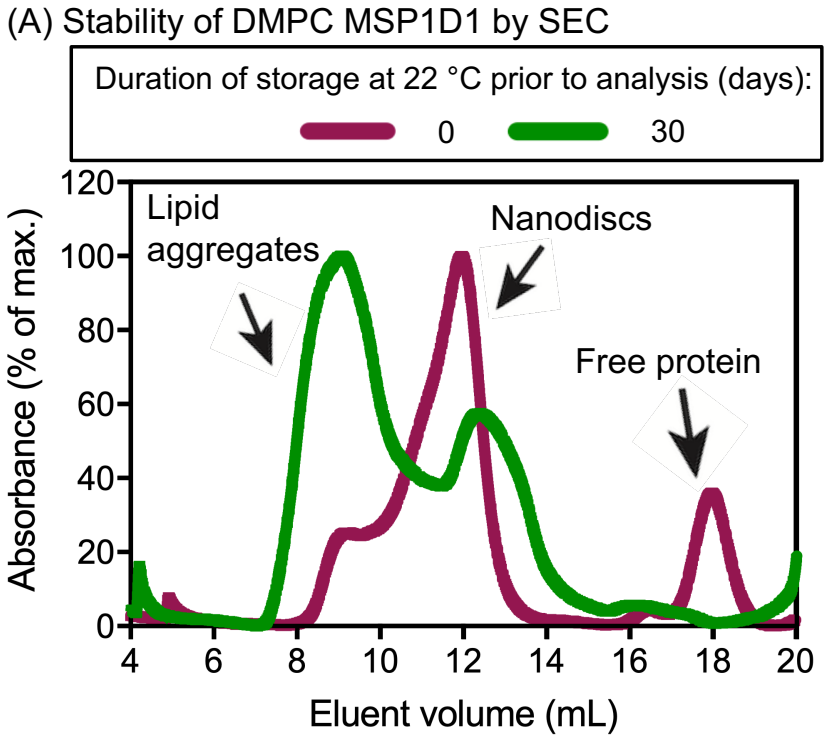

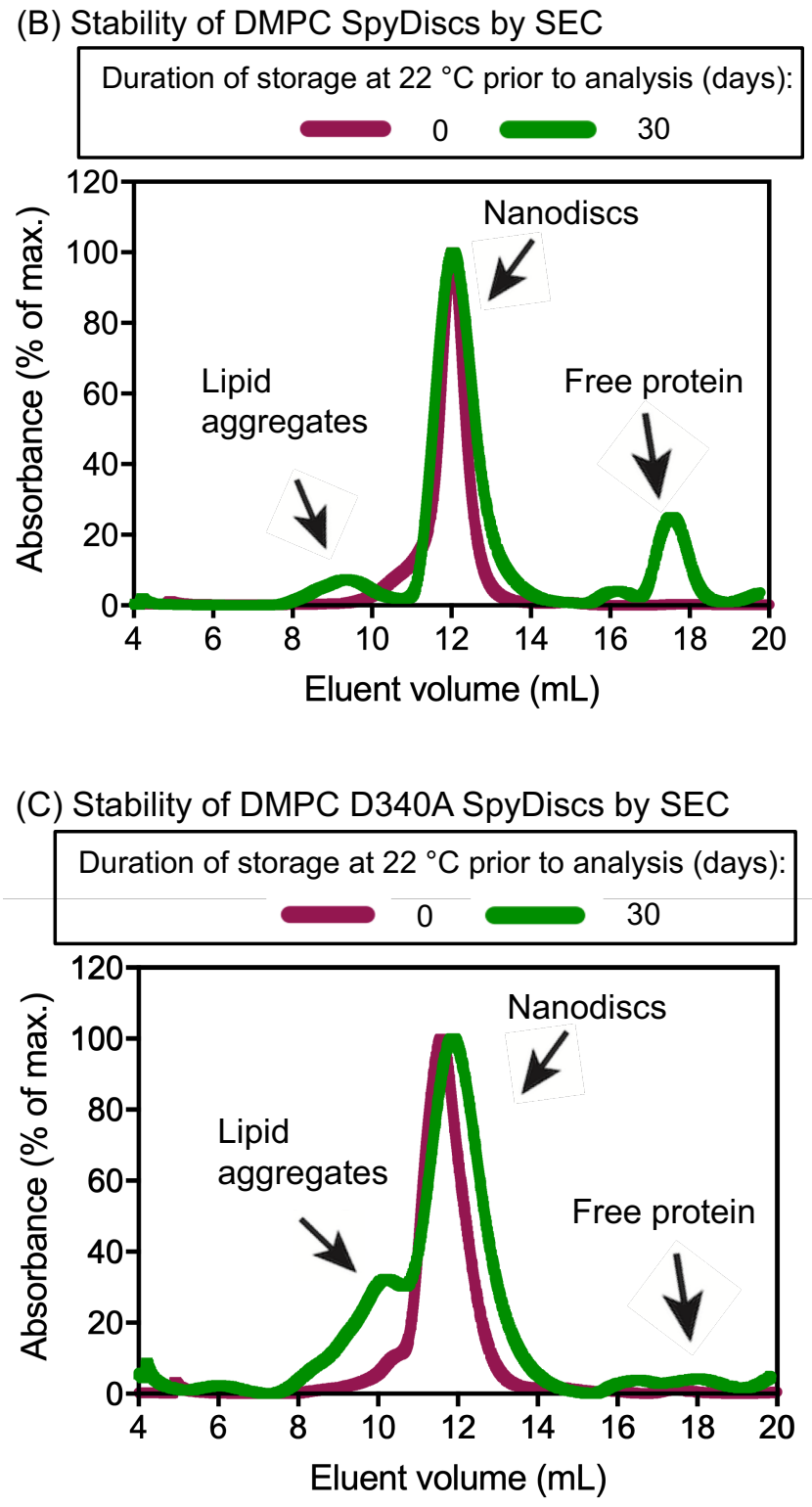

Figure 2.20. Stability of DMPC MSP1D1 nanodiscs (A), SpyDiscs (B), and D340A SpyDiscs (C) over 0-4 weeks at 22 °C.

(A) Stability of DMPC MSP1D1 by SEC

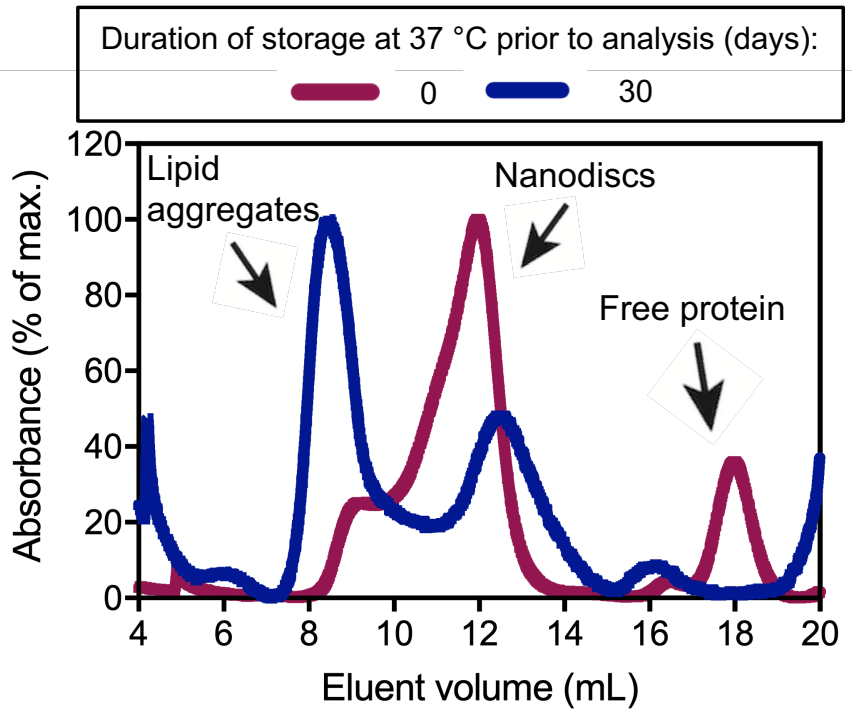

(B) Stability of DMPC SpyDiscs by SEC

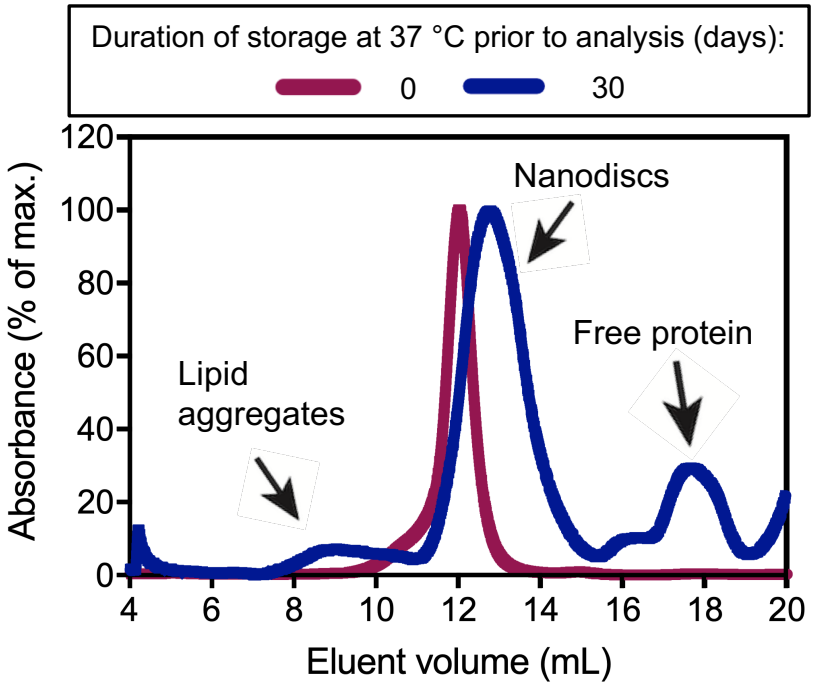

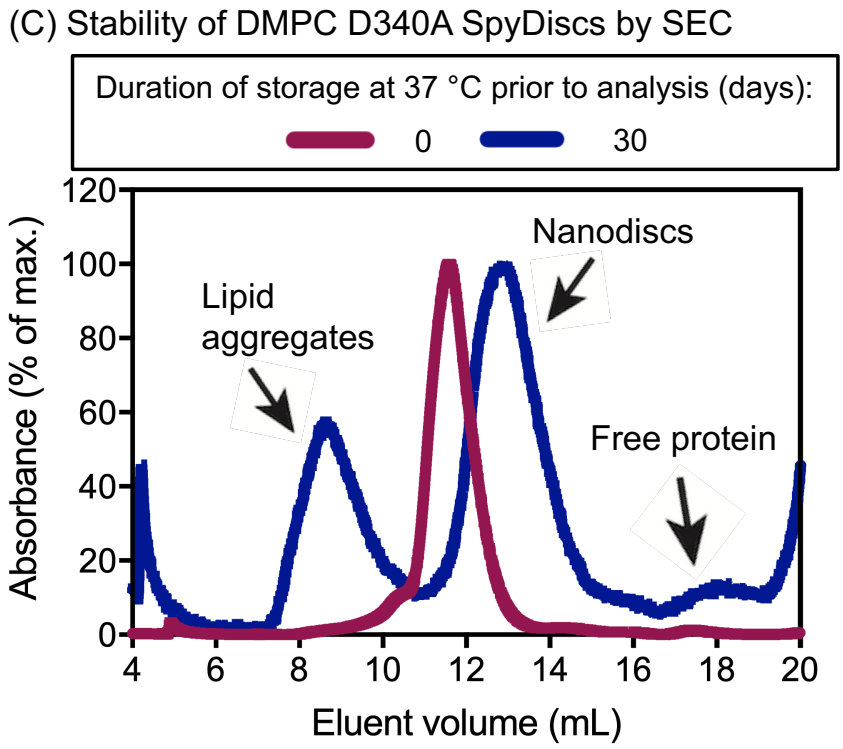

Figure 2.21. Stability of DMPC MSP1D1 nanodiscs (A), SpyDiscs (B), and D340A SpyDiscs (C) over 0-4 weeks at 37 °C.

2.5. Analysis of effects of membrane-disruptive peptides on MSP1D1 nanodiscs, SpyDiscs, and D340A SpyDiscs

To investigate the effects of membrane-active peptides, we reconstituted MSP1D1 nanodiscs, SpyDiscs, and D340A SpyDiscs with the peptides alamethicin, melittin, and Chol-EDP. As shown in Figure 2.22, the typical 10 nm discoidal structures of MSP1D1 nanodiscs were massively disrupted under these conditions, and only large aggregates were observed by TEM in the presence of any of these peptides. These aggregates ranged from ~ 50 nm to 500 nm or larger in diameter.

(A) MSP1D1 nanodiscs with alamethicin

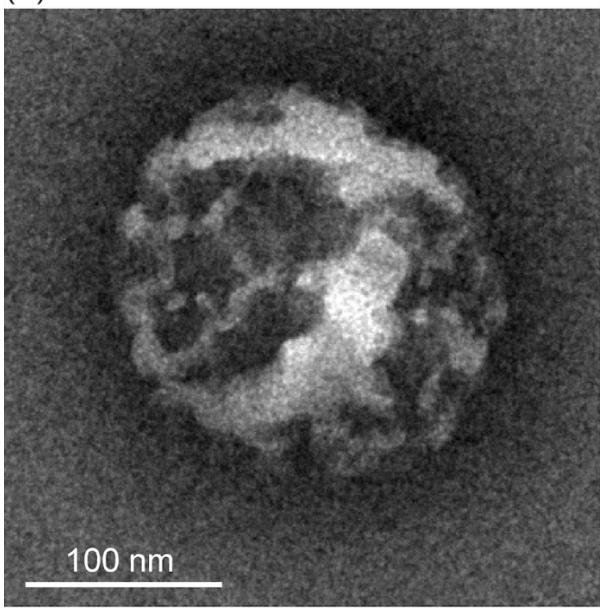

(B) MSP1D1 nanodiscs with mellitin

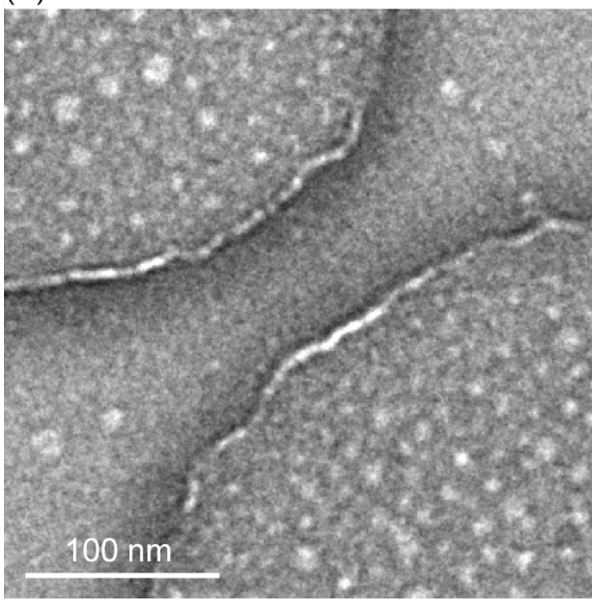

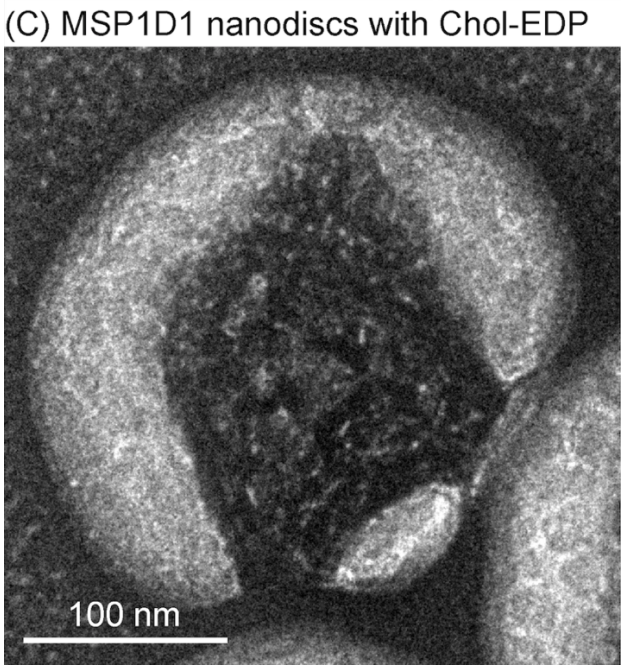

Figure 2.22. TEM of MSP1D1 and POPC in the presence of the membrane active peptides alamethicin (A), melittin (B), and Chol-EDP (C). Nanodiscs did not form under these conditions, and large protein-lipid aggregates were observed.

In contrast, when these peptides were assembled with SpyDiscs under the same conditions (Figure 2.23), only minor effects on the overall size of the discoid structures were observed. Moreover, when alamethicin was incorporated into SpyDiscs, discrete pores of 2 ± 1 nm diameter were clearly visible within nanodiscs measuring 12 ± 1 nm (n = 25). These results were consistent with the pore diameter of 2.0 ± 0.3 nm previously measured by electrochemical scanning tunneling microscopy[35] and atomic force microscopy.[36] Surprisingly, when SpyDiscs were assembled with melittin, this peptide reduced the size of the discoids to 8 ± 1 nm (n=30) as measured by TEM. However discrete pores of 2 ± 1 nm were also observed in these smaller SpyDiscs. We suggest that this contraction in size could potentially relate to the non-lamellar phase and toroidal nature of pores induced by melittin compared with the barrel-stave pores formed by

alamethicin.[44,61] Both alamethicin and melittin form amphiphilic helices in membranes, but at pH 7, the predominant net charge for alamethicin is −1 and for melittin is +5, resulting in stronger electrostatic interactions of melittin with membranes that favor formation of toroidal pores.[61] SpyDiscs assembled with Chol-EDP were similar to those observed with alamethicin with overall dimensions of 12 ± 1 nm (n = 25) and pores of 2 ± 1 nm in diameter measured by TEM.

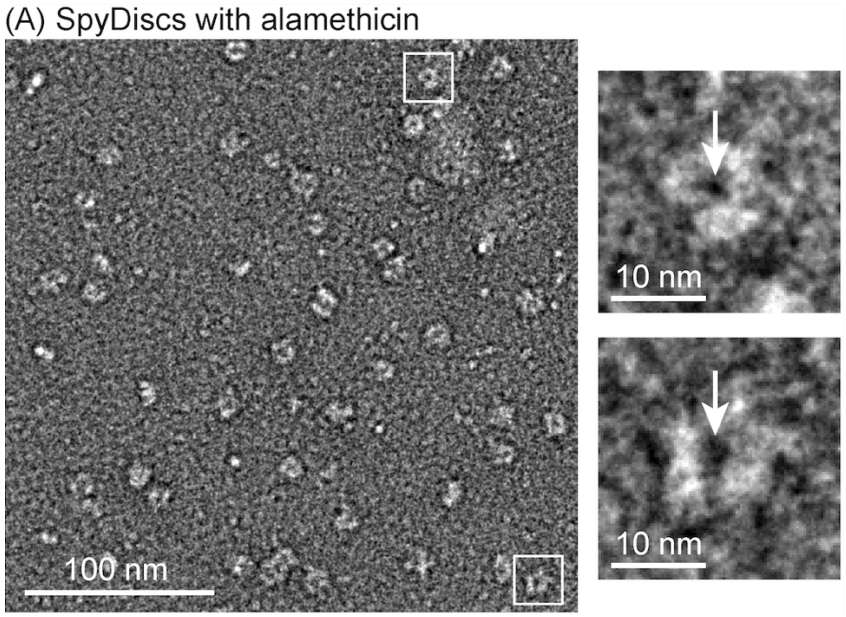

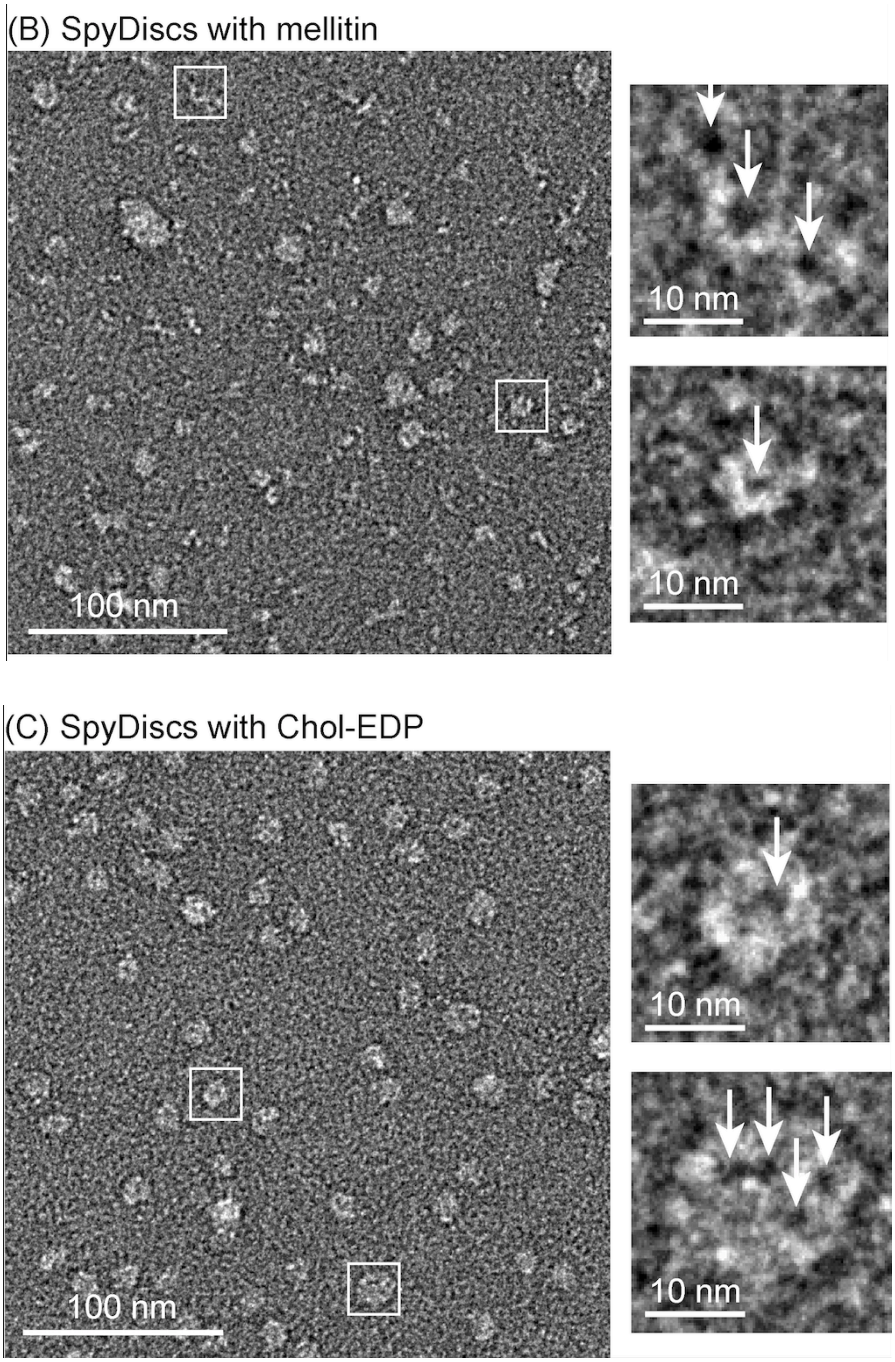

Figure 2.23. TEM of SpyDiscs assembled with POPC in the presence of the membrane active peptides alamethicin (A), melittin (B), and Chol-EDP (C). These conditions did not disrupt the formation of SpyDiscs, and most of the SpyDiscs in the field of view exhibited one or more distinct pores of 2 ± 1 nm diameter. Treatment with alamethicin and Chol-EDP did not significantly affect the diameter of SpyDiscs (12 ± 1 nm), but melittin caused contraction of SpyDiscs to 8 ± 1 nm.

Similar imaging studies of the non-covalently crosslinked D340A SpyDiscs revealed that these nanodiscs are sufficiently stable to allow imaging of pores formed by membrane-active peptides (Figure 2.24). In this system, the same trends were observed, where all three peptides promoted the formation of pores with a diameter of 2 ± 1 nm. The D340A SpyDiscs exhibited diameters of 13 ± 2 nm (n = 25) for alamethicin and Chol-EDP and were similarly contracted to 9 ± 1 nm (n = 25) by melittin.

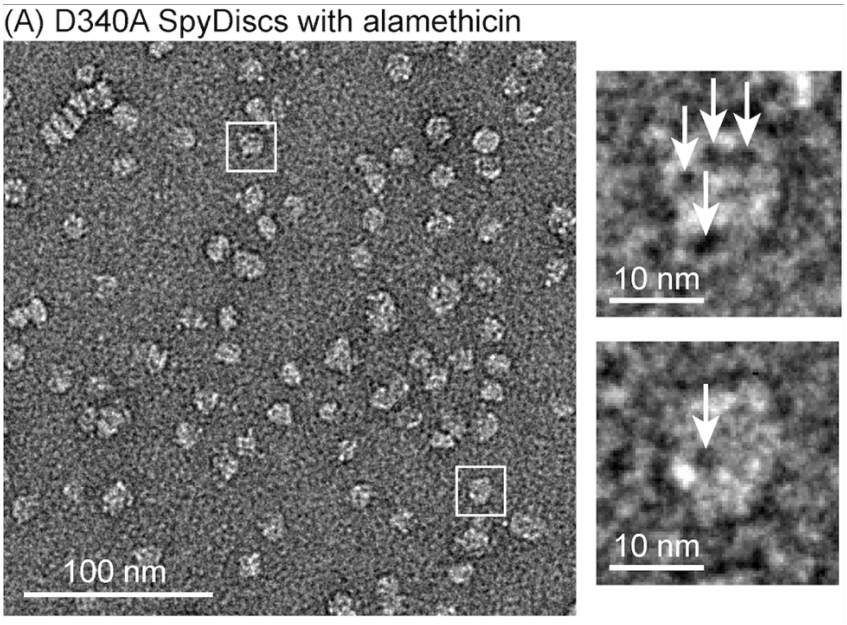

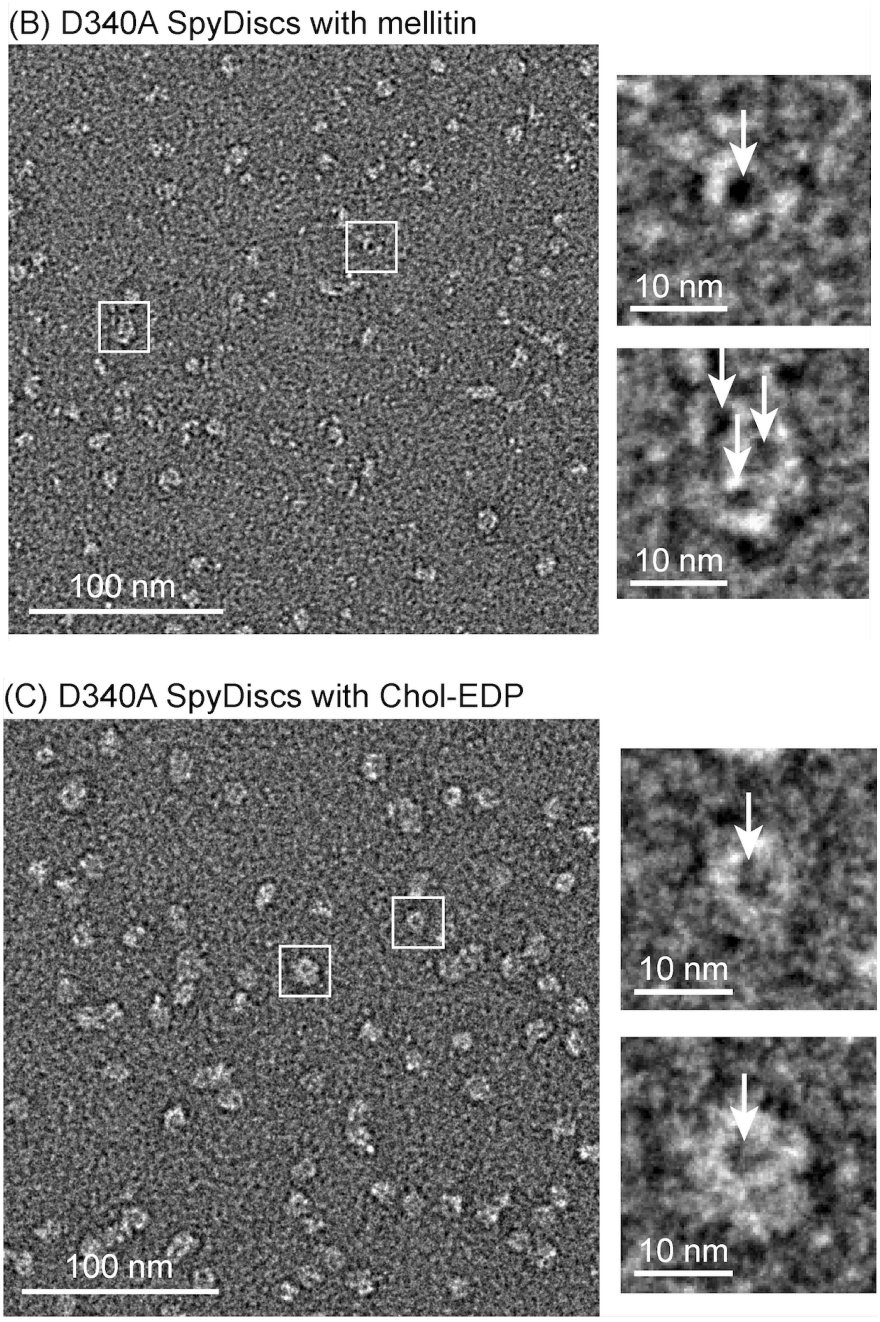

Figure 2.24. TEM of D340A SpyDiscs assembled with POPC in the presence of alamethicin (A), melittin (B), and Chol-EDP (C). These conditions did not disrupt the formation of D340A SpyDiscs, and most of the SpyDiscs in the field of view exhibited one or more distinct pores of 2 ± 1 nm diameter. Treatment with alamethicin and Chol-EDP did not significantly affect the diameter of D340A SpyDiscs (13 ± 2 nm, n = 25), but melittin caused contraction of D340A SpyDiscs to 9 ± 1 nm (n = 25).

2.6. Conclusions and future directions

Fusion of SpyCatcher and SpyTag to the membrane scaffold protein MSP1D1 enables the construction of lipidic nanodiscs that spontaneously cyclize through formation of a covalent isopeptide bond. With diameters of 12 ± 2 nm, SpyDiscs are similar in size to conventional nanodiscs derived from the membrane scaffold protein MSP1D1. However, SpyDiscs exhibit substantially higher melting temperatures of > 75 °C measured by temperature-dependent CD spectroscopy. When stored at 4 °C, this enhanced stability allows SpyDiscs to maintain > 80% integrity after 10 weeks, conditions where traditional MSP1D1 nanodiscs extensively disintegrate. The covalent isopeptide bond of SpyDiscs substantially enhances the stability of these assemblies when compared to D340A mutant SpyDiscs where formation of this bond is blocked. However, D340A SpyDiscs are more stable than MSP1D1 nanodiscs, suggesting that non-covalent interactions between SpyTag D340A with SpyCatcher can provide a substantial stabilizing mechanism. In contrast to conventional MSP1D1 nanodiscs, the enhanced stability of SpyDiscs enables imaging of pore formation by membrane-active peptides such as alamethicin, melittin, and Chol-EDP. These peptides form pores of 2 ± 1 nm diameter in SpyDiscs that can be imaged by transmission electron microscopy. For the natural products alamethicin[35,36] and melittin,[42,43] these values are consistent with pore sizes obtained using other experimental and computational approaches. For the synthetic peptide Chol-EDP, these results suggest that similarly small pores are created by this compound in membranes. This interpretation would be consistent with its low toxicity towards mammalian cells under conditions where it promotes the escape of small molecules from endosomes.[32] Given that many important biological processes including

apoptosis,[11-13] immunity,[14,15] bacterial toxins,[16,17] viral infection,[18] and protein translocation[19] function to disrupt membranes, SpyDiscs may offer useful tools for investigating these systems by NMR, TEM, Cryo-EM, and other methods.

2.7. Experimental

2.7.1. General

Chemicals were obtained from Avanti Polar Lipids, Sigma Aldrich, Acros Organics, Alfa Aesar, or Oakwood Chemical. Chol-EDP was prepared as previously described.[32] Water was purified with a MilliQ purification system (Millipore). Absorbance spectra were obtained on an Aligent 8452A diode array spectrometer. PCR amplifications were performed on T-gradient thermocycler (Biometra). Theoretical masses and extinction coefficients of the protein constructs were calculated with the Expasy tool protparam.

2.7.2. Design, cloning, and mutagenesis of plasmids

2.7.2.1. MSPSS_M6 plasmid

In MSPSS_M6, the initiator methionine was followed by a GC linker, heptahistidine tag, and tobacco etch virus (TEV) protease cleavage site, similar to the leader sequence preceding MSP1D1 in plasmid pMSP1D1 (pMSP1D1 was a gift from Stephen Sligar (Addgene plasmid # 20061). This was fused at its C-terminus to fourteen amino acids (QLNLKLLDNWDSVT) from human-ApoA1. These ApoA1 residues were incorporated based on visualization of a model of ApoA1[45] (UniProtKB:P02647),[62] to provide a contiguous extended sequence for MSP1D1. At the C-terminus of MSP1D1, another Cys

was added to form the disulfide bond with the Cys at the N-terminus. The plasmid pMSPSS_M6 was constructed by PCR with Phusion polymerase (New England Biolabs) An MfeI restriction site was introduced in the sequence to facilitate primer synthesis. The primers 5' NcoI (1-) 5'-GATATACCATGGGTCATCATCATCATCA-3', 3' MfeI (-33) 5'-CAGATTCAAtTGCTTCCCCAGCGCGGAACCGCAACCCTGAAAATACAAATTCTCAGT-3', 5' MfeI (33-) 5'-GGGAAGCAaTTGAATCTGAAGTTGCTTGATAACTGGGATAGCGTTACGTCTACCTTC AGTAAACTTCGCGAA-3' and 3' HindIII-Stop (-234) 5'-CGGAGTAAGCTTAGCACTGGGTATTCAGCTTTTTAGTATA-3', and pMSP1D1 as a template to add 5'- *NcoI* and 3'- *HindIII* restriction sites. The PCR fragment was digested with *NcoI* and *HindIII*, ligated into *NcoI* and *HindIII*-digested pET28a, and confirmed by Sanger sequencing. Vectors derived from pET28a were propagated on LB/kanamycin plates.

2.7.2.2. SpyMSP and D340A SpyMSP plasmids

In SpyMSP, the initiator methionine was followed by a GYY linker, hexahistidine tag, and tobacco etch virus (TEV) protease cleavage site, similar to the leader sequence preceding MSP1D1 in plasmid pMSP1D1 (pMSP1D1 was a gift from Stephen Sligar (Addgene plasmid # 20061). A short GS linker was added to the N-terminus of SpyCatcherΔN1,[57] which was fused at its C-terminus through a longer GSGGSG linker to fourteen amino acids (QLNLKLLDNWDSVTA) from human-ApoA1. These ApoA1 residues were incorporated based on visualization of a model of ApoA1[45] (UniProtKB:P02647),[62] to provide a contiguous extended sequence for MSP1D1. At the

C-terminus of MSP1D1, another GSGGSG linker was added followed by the 13 amino acid SpyTag peptide[47] (AHIVMVDAYKPTK). The SpyMSP gene was codon-optimized for expression in *E. coli*, synthesized, and cloned into the 5'- *NcoI* and 3'- *HindIII* sites of plasmid pET28a by GenScript USA to afford plasmid pSpyMSP. The mutant plasmid pSpyMSP D340A was constructed by PCR with Phusion polymerase (New England Biolabs), the primers 5'- ACTCCGCCATGGGTTACTACCATCACCATCACC-3' and 5'- AAGCTTATTTGGTCGGTTTGTACGCCGCCACCATAACGATGTGCGCA-3', and pSpyMSP as a template to mutate Asp340 to Ala and add 5'- *NcoI* and 3'- *HindIII* restriction sites. The PCR fragment was digested with *NcoI* and *HindIII*, ligated into *NcoI* and *HindIII*-digested pET28a, and confirmed by Sanger sequencing. Vectors derived from pET28a were propagated on LB/kanamycin plates.

2.7.3. Expression and purification of proteins

2.7.3.1. MSP1D1 protein

MSP1D1 was expressed, cleaved with TEV protease, and purified as previously reported.[23] The concentration of purified MSP1D1 (MW: 22044 Da) was determined using a nanodrop instrument by absorbance at 280 nm (ε = 18450 $cm^{-1}M^{-1}$).

2.7.3.2. MSPSS_M6 protein

Expression and purification of the MSPSS_M6 protein was based on this previously described[20] method with some modifications. A colony of chemically competent BL21 (DE3) *E. coli* transformed with pMSPSS_M6 was suspended in LB media (10 mL) containing kanamycin (50 μg/mL) and incubated at 37 °C with agitation

(200 rpm) until OD_{600} reached 0.5. The cell pellet was isolated by centrifugation, dispersed in sterile TB media (1L) containing kanamycin (50 μg/mL), and incubated at 37 °C (200 rpm) until OD_{600} reached 0.6–0.8 (3 to 4 h). These cells were induced with isopropyl-β-D-thiogalactopyranoside (IPTG, final concentration 1 mM), and further grown at 37 °C (200 rpm) until the OD_{600} was 1.8–2.1 (16–18 h). Cells were harvested by centrifugation (4,000 rpm, 4 °C, 10 min). The supernatant was discarded, and the cell pellet was dispersed in Buffer 1 (20 mM Tris HCl, pH 7.4, 50 mM NaCl, loading buffer). The protease inhibitor PMSF (final concentration 500 mM) was added, and the cells were lysed by sonication on ice. This lysate was centrifuged (13,000 rpm, 4 °C, 10 min), the pellet was discarded, and the supernatant was collected. Aqueous polyethylenimine (PEI) (700 μL 50%) was added to the supernatant to precipitate nucleic acids, which were removed by centrifugation (13,000 rpm, 4 °C, 10 min). The pellet was discarded, and the supernatant was loaded onto a Ni^{2+}-NTA column, prewashed with Buffer 1, for protein purification. The column was washed sequentially with 10 column volumes of the following buffers: Buffer 1 + 1 % Triton-X, Buffer 1 + imidazole (20 mM), Buffer 1, Buffer 1 + imidazole (40 mM). The protein was eluted with Buffer 1 + imidazole (500 mM). TEV protease (New England Biolabs, 100 μL (1000 units) TEV protease for 2 mg MSPSS_M6 protein) was added with TEV protease reaction buffer, and the digestion was allowed to proceed at 30 °C for 3 h. This mixture was again loaded onto Ni^{2+}-NTA column and purification protocol described previously was followed. In this case, the MSPSS_M6 protein was eluted with loading buffer (Buffer 1) after the His-tag was cleaved. The protein eluate was dialyzed against 50-fold nanodisc assembly buffer (20 mM Tris HCl, pH 7.4, 50 mM NaCl and 0.5 mM EDTA) in regenerated cellulose dialysis tubing (3500 Da, Fisher

Brand) at 4 °C for 4 h. This buffer was exchanged two times for 4 h, and dialysis was carried out for additional 16 h. Protein was concentrated using Amicon ultra 3,000 MWCO centrifugal concentrators (Millipore Sigma), and was further purified by size-exclusion chromatography on an AKTA pure system (GE Healthcare) using a Superdex 75 Increase 10/300 GL column equilibrated with SEC buffer (50 mM Tris HCl, pH 7.4, 150 mM NaCl) at a flow rate of 0.5 mL/min. The concentration of purified MSPSS_M6 (MW: 23891 Da) was determined using a nanodrop instrument by absorbance at 280 nm (ε = 24075 $cm^{-1}M^{-1}$).

2.7.3.3. SpyMSP and D340A SpyMSP proteins

Expression and purification of the SpyMSP and SpyMSP D340A proteins was based on this previously described[20] method with some modifications. A colony of chemically competent BL21 (DE3) *E. coli* transformed with pSpyMSP was suspended in LB media (10 mL) containing kanamycin (50 μg/mL) and incubated at 37 °C with agitation (200 rpm) until OD_{600} reached 0.5. The cell pellet was isolated by centrifugation, dispersed in sterile TB media (1L) containing kanamycin (50 μg/mL) and incubated at 37 °C (200 rpm) until OD_{600} reached 0.6–0.8 (3 to 4 h). These cells were induced with isopropyl-β-D-thiogalactopyranoside (IPTG, final concentration 1 mM), and further grown at 15 °C (200 rpm) until the OD_{600} was 1.8–2.1 (12–14 h). Cells were harvested by centrifugation (4,000 rpm, 4 °C, 10 min). The supernatant was discarded, and the cell pellet was dispersed in Buffer 2 (20 mM Tris HCl, pH 7.4, 50 mM NaCl, 2 mM TCEP, loading buffer). The protease inhibitor PMSF (final concentration 500 mM) was added, and the cells were lysed by sonication on ice. This lysate was centrifuged (13,000 rpm, 4

°C, 10 min), the pellet was discarded, and the supernatant was collected. Aqueous polyethylenimine (PEI) (700 μL 50%) was added to the supernatant to precipitate nucleic acids, which were removed by centrifugation (13,000 rpm, 4 °C, 10 min). The pellet was discarded, and the supernatant was loaded onto a Ni^{2+}-NTA column, prewashed with Buffer 2, for protein purification. The column was washed sequentially with 10 column volumes of the following buffers: Buffer 2 + 1 % Triton-X, Buffer 2 + imidazole (20 mM), Buffer 2, Buffer 2 + imidazole (40 mM). The protein was eluted with Buffer 2 + imidazole (500 mM). TEV protease (New England Biolabs, 100 μL (1000 units) TEV protease for 2 mg SpyMSP protein) was added with TEV protease reaction buffer, and the digestion was allowed to proceed at 30 °C for 3 h. This mixture was again loaded onto Ni^{2+}-NTA column and purification protocol described previously was followed. In this case, the cyclized SpyMSP protein was eluted with loading buffer (Buffer 2) after the His-tag was cleaved. The protein eluate was dialyzed against 50-fold nanodisc assembly buffer (20 mM Tris HCl, pH 7.4, 50 mM NaCl and 0.5 mM EDTA) in regenerated cellulose dialysis tubing (3500 Da, Fisher Brand) at 4 °C for 4 h. This buffer was exchanged two times for 4 h, and dialysis was carried out for additional 16 h. Protein was concentrated using Amicon ultra 3,000 MWCO centrifugal concentrators (Millipore Sigma), and was further purified by size-exclusion chromatography on an AKTA pure system (GE Healthcare) using a Superdex 75 Increase 10/300 GL column equilibrated with SEC buffer (50 mM Tris HCl, pH 7.4, 150 mM NaCl) at a flow rate of 0.5 mL/min. The concentration of purified SpyMSP (MW: 36031 Da, after loss of a water molecule) was determined using a nanodrop instrument by absorbance at 280 nm (ε = 36900 $cm^{-1}M^{-1}$).

The SpyMSP D340A protein was similarly overexpressed and purified. The concentration of purified SpyMSP D340A (MW: 36005 Da) was determined using a nanodrop instrument by absorbance at 280 nm (ε = 36900 $cm^{-1}M^{-1}$). The purity of these proteins, evaluated by analytical HPLC and SDS-PAGE, exceeded 95%.

2.7.4. Reconstitution of empty nanodiscs

2.7.4.1. Nanodiscs made with POPC lipids

Nanodiscs were assembled following a published protocol.[20] An appropriate amount of POPC lipids dissolved in chloroform was dried under nitrogen followed by overnight removal of residual chloroform in a vacuum desiccator. Lipids were resuspended in nanodisc assembly buffer that was supplemented with sodium cholate to provide a molar ratio of lipid:sodium cholate of 1:2. The lipid and cholate mixture was sonicated with a microtip probe (Fisher Scientific Sonic Dismembrator Model 500) for 5 min on ice at 10% amplitude (10 sec on and 30 sec off) until the lipid was clearly dispersed in the solution. The MSPs were resuspended in the lipid-cholate mixture (final [cholate] = 30 mM) and incubated at 4 °C (for POPC) for 1 h. The molar ratio of POPC:protein was 130:1 for SpyDiscs and D340A SpyDiscs, whereas it was 65:1 for MSPSS_M6 and MSP1D1 nanodiscs. This ratio of 130:1 was chosen based on the previously published[23] ratio of POPC:MSP1E3 protein used for MSP1E3 nanodiscs, given that the diameter of both these nanodiscs are similar. After incubating the nanodisc constituents for 1 h, the contents were dialyzed in regenerated cellulose dialysis tubing (12 – 14 kDa MWCO, Fisherbrand) or a Slide-A-Lyzer device (MWCO of 10 kDa) against 1000-fold of nanodisc assembly buffer (20 mM Tris HCl, pH 7.4, 50 mM NaCl and 0.5 mM EDTA) for 4 h at 4

°C. This buffer was exchanged two times for 4 h, and dialysis was carried out for an additional 16 h. The sample was purified by size-exclusion chromatography on an AKTA pure system using a Superdex 200 increase 10/300 GL column (10 mm X 300 mm) equilibrated with SEC buffer (50 mM Tris HCl, pH 7.4, 150 mM NaCl) at a flow rate of 0.5 mL/min. The fractions that corresponded to the size of the nanodiscs, based on external size standards, were collected, and the purity of these nanodiscs was assessed by SDS-PAGE. The concentration of purified nanodiscs was determined with a nanodrop instrument by the absorbance at 280 nm using the molar extinction coefficient of MSPSS_M6 (ε = 24075 $cm^{-1}M^{-1}$), SpyMSP (ε = 36390 $cm^{-1}M^{-1}$) and SpyMSP D340A (ε = 36390 $cm^{-1}M^{-1}$). MSP1D1 nanodiscs were used as a control.

2.7.4.2. Nanodiscs made with DMPC lipids

Nanodiscs were assembled following a published protocol.[20] An appropriate amount of DMPC lipids dissolved in chloroform was dried under nitrogen followed by overnight removal of residual chloroform in a vacuum desiccator. Lipids were resuspended in nanodisc assembly buffer that was supplemented with sodium cholate to provide a molar ratio of lipid:sodium cholate of 1:2. The lipid and cholate mixture was sonicated with a microtip probe (Fisher Scientific Sonic Dismembrator Model 500) for 5 min on ice at 10% amplitude (10 sec on and 30 sec off) until the lipid was clearly dispersed in the solution. The MSPs were resuspended in the lipid-cholate mixture (final [cholate] = 30 mM) and incubated at 25 °C (for DMPC) for 1 h. The molar ratio of DMPC:protein was 150:1 for SpyDiscs and D340A SpyDiscs, whereas it was 80:1 for MSP1D1 nanodiscs. This ratio of 150:1 was chosen based on the previously published[23] ratio of

DMPC:MSP1E3 protein used for MSP1E3 nanodiscs, given that the diameter of both these nanodiscs are similar. After incubating the nanodisc constituents for 1 h, the contents were dialyzed in regenerated cellulose dialysis tubing (12 – 14 kDa MWCO, Fisherbrand) or a Slide-A-Lyzer device (MWCO of 10 kDa) against 1000-fold of nanodisc assembly buffer (20 mM Tris HCl, pH 7.4, 50 mM NaCl and 0.5 mM EDTA) for 4 h at 25 °C. This buffer was exchanged two times for 4 h, and dialysis was carried out for an additional 16 h. The sample was purified by size-exclusion chromatography on an AKTA pure system using a Superdex 200 increase 10/300 GL column (10 mm X 300 mm) equilibrated with SEC buffer (50 mM Tris HCl, pH 7.4, 150 mM NaCl) at a flow rate of 0.5 mL/min. The fractions that corresponded to the size of the nanodiscs, based on external size standards, were collected, and the purity of these nanodiscs was assessed by SDS-PAGE. The concentration of purified nanodiscs was determined with a nanodrop instrument by the absorbance at 280 nm using the molar extinction coefficient of SpyMSP (ε = 36390 $cm^{-1}M^{-1}$) and SpyMSP D340A (ε = 36390 $cm^{-1}M^{-1}$). MSP1D1 nanodiscs were used as a control.

2.7.5. Reconstitution of membrane-disruptive peptides with POPC nanodiscs

These nanodiscs were assembled similarly to empty nanodiscs with an additional step in the incubation process. An appropriate amount of POPC lipids dissolved in chloroform was dried under nitrogen followed by overnight removal of residual chloroform in a vacuum desiccator. Lipids were resuspended in nanodisc assembly buffer that was supplemented with sodium cholate to provide a molar ratio of lipid:sodium cholate of 1:2. The lipid and cholate mixture was sonicated for 5 min on ice. The MSPs and membrane-

active peptide (alamethicin, melittin, or Chol-EDP – 10 mM DMSO stock, final DMSO concentration: 0.8%) was resuspended in the lipid-cholate mixture (final [cholate] = 30 mM) and incubated at 4 °C (for POPC) for 1 h. The POPC:protein molar ratio was 130:1 for SpyDiscs and D340A SpyDiscs, whereas it was 65:1 for MSP1D1 nanodiscs. The molar ratio of protein:membrane-active peptide was 1:2. After incubating the nanodisc constituents for 1 h, the contents were in regenerated cellulose dialysis tubing (12 – 14 kDa MWCO, Fisherbrand) or a Slide-A-Lyzer device (MWCO of 10 kDa) against 1000-fold nanodisc forming buffer (20 mM Tris HCl, pH 7.4, 50 mM NaCl and 0.5 mM EDTA) for 4 h at 4 °C (for POPC). This buffer was exchanged two times for 4 h, and dialysis was carried out for additional 16 h. The sample was purified by size-exclusion chromatography Superdex 200 10/300 column equilibrated with SEC buffer (50 mM Tris HCl, pH 7.4, 150 mM NaCl). The fractions that corresponded to the size of the nanodiscs, based on external size standards, were collected, and the purity of these nanodiscs was assessed by SDS-PAGE.

2.7.6. Negative-stain transmission electron microscopy (TEM)

Samples of nanodiscs (5 μL, 50 μg/mL) in SEC buffer were adsorbed on carbon-coated copper grids (300 mesh, 3 min). These copper grids were subjected to negative glow-discharge using a sputter coater (EMS150RS, Electron Microscopy Sciences, USA) for 30 sec prior to sample application to make the surface hydrophilic. Excess sample solution on the copper grids was wicked away with filter paper. The grids with nanodiscs were negatively stained with 2% (w/v) uranyl acetate solution (5 min), the excess stain was wicked away with filter paper, and these grids were used for imaging. The negatively

stained grids with nanodiscs were imaged using a 200 kV FEI Technai F20 XT field emission transmission electron microscope at an electron acceleration voltage of 120 kV. TEM images were captured using a normative and standardized electron dose on a eucentric specimen stage and a constant defocus value from the carbon-coated surfaces. Images were randomly acquired in a size of 1024x1024 pixel resolution at 10 different locations within the grid. Images were selected based on visual assessment of particle dispersion, quality of stain, quality of background, and low astigmatism. Diameters of nanodiscs and pores obtained from TEM images (mean ± SD) were measured by reference to the scale bar using ImageJ software.[59] The number of experiments (N) correspond to independent measurements from at least three different sample preparations.

2.7.7. Dynamic light scattering (DLS)

The size of nanodiscs was additionally analyzed by DLS. The experiments were performed using the dynamic light scattering mode on a ZetaPALS zetasizer (Brookhaven Instruments Corporation, Holtzville, NY), using quartz cuvettes that were cleaned to remove any dust and air-dried. Nanodisc samples were diluted to 0.2 mg/mL in SEC buffer and passed through a 0.22 μm filter before analysis. The hydrodynamic diameters of each sample were determined by generating an autocorrelation decay function, with each being a 5-scan average (each ~30 s long) at 22 °C. The intensity distributions were fit using the lognormal and cumulant analysis algorithm of the instrument software.

2.7.8. Circular dichroism (CD)

The CD spectra were collected using a Jasco J-815 spectropolarimeter (Jasco Inc, Easton, MD). The instrument was allowed to equilibrate at 22 °C for 15 min prior to data acquisition. Spectra was recorded from 200–280 nm to monitor secondary structure. CD absorbance was measured using a rectangular quartz cuvette with a 0.1 cm path length. Data were collected with protein samples at 0.2 mg/mL in Phosphate Buffered Saline (1X PBS, pH 7.4, Corning Life Sciences). The instrument was set to record data from 10–90 °C with increments of 2.5 °C and a 1 nm step size. Triplicate scans were collected from 200-280 nm in continuous scanning mode for each temperature, with a scan speed of 100 nm/min and a 1 nm bandwidth. The scans were collected at a rate of 1 °C/min and samples were allowed to equilibrate for an additional 3 min after the instrument reached a new temperature increment prior to the collection of data. The buffer signal was subtracted, corrected for protein concentration and the CD signal in molar ellipticity was reported. T_m was obtained from curve fitting with the Boltzmann sigmoid equation (GraphPad Prism 8).

2.7.9. Mass spectrometry

Mass spectra were obtained at the Mass Spectrometry Laboratory at the University of Kansas. Whole protein mass determinations were derived from data obtained by LC/MS, desalting samples, followed by ionization by electrospray with mass analysis in a QTof instrument. Protein (10–100 ng) in water was trapped on a C4 column at low organic content and then eluted with a gradient to 70% organic solvent. The solvent used was MeOH:CH_3CN:isopropanol in equal ratios, and the aqueous solution included 0.08%

formic acid. The ‘zero charge’ spectra were generated from electrospray generated charge state ladders using the MaxEntI tool in Waters masslynx 4.1. A Waters QTof premier or Synapt G2 mass analyzer was used with data acquired up to 3000 u. C4 reverse-phase Zorbax columns with 1 mm ID and manually packed guard columns were used for purification.

2.7.10. High performance liquid chromatography (HPLC)

HPLC data was acquired on Agilent 1220 Infinity LC equipped with Agilent PLRP-S reverse phase column (8 um particle size, 4.6 mm x 250 mm) and diode array detector. Elution was achieved with a gradient of water and acetonitrile (90:10 to 0:100 containing 0.1% TFA) over 25 min.

2.8. References

1. Edidin, M., Lipids on the frontier: a century of cell-membrane bilayers. *Nat. Rev. Mol. Cell Biol.* **2003***, 4*, 414.

2. Danielli, J. F.; Davson, H., A contribution to the theory of permeability of thin films. *J. Cell. Physiol.* **1935***, 5*, 495-508.

3. Mueller, P.; Rudin, D. O.; Tien, H. T.; Wescott, W. C., Reconstitution of cell membrane structure in vitro and its transformation into an excitable system. *Nature.* **1962***, 194*, 979-980.

4. Knoll, W.; Naumann, R.; Friedrich, M.; Robertson, J. W.; Losche, M.; Heinrich, F.; McGillivray, D. J.; Schuster, B.; Gufler, P. C.; Pum, D.; Sleytr, U. B., Solid supported lipid membranes: new concepts for the biomimetic functionalization of solid surfaces. *Biointerphases.* **2008***, 3*, FA125.

5. Miyamoto, V. K.; Stoeckenius, W., Preparation and characteristics of lipid vesicles. *J. Membr. Biol.* **1971***, 4*, 252-269.

6. Maherani, B.; Arab-Tehrany, E.; R Mozafari, M.; Gaiani, C.; Linder, M., Liposomes: a review of manufacturing techniques and targeting strategies. *Curr. Nanosci.* **2011***, 7*, 436-452.

7. Helenius, A.; Simons, K., Solubilization of membranes by detergents. *Biochim. Biophys. Acta Biomembr.* **1975***, 415*, 29-79.

8. Sanders, C. R.; Landis, G. C., Reconstitution of membrane proteins into lipid-rich bilayered mixed micelles for NMR studies. *Biochemistry.* **1995***, 34*, 4030-4040.

9. Tribet, C.; Audebert, R.; Popot, J.-L., Amphipols: polymers that keep membrane proteins soluble in aqueous solutions. *Proc. Natl. Acad. Sci. U. S. A.* **1996***, 93*, 15047-15050.

10. Peetla, C.; Stine, A.; Labhasetwar, V., Biophysical interactions with model lipid membranes: applications in drug discovery and drug delivery. *Mol. Pharm.* **2009***, 6*, 1264-1276.

11. Garcia-Saez, A., The secrets of the Bcl-2 family. *Cell Death Differ.* **2012***, 19*, 1733.

12. Walensky, L. D.; Gavathiotis, E., BAX unleashed: the biochemical transformation of an inactive cytosolic monomer into a toxic mitochondrial pore. *Trends Biochem. Sci.* **2011***, 36*, 642-652.

13. Westphal, D.; Kluck, R.; Dewson, G., Building blocks of the apoptotic pore: how Bax and Bak are activated and oligomerize during apoptosis. *Cell Death Differ.* **2014***, 21*, 196.

14. Kondos, S.; Hatfaludi, T.; Voskoboinik, I.; Trapani, J. A.; Law, R. H.; Whisstock, J. C.; Dunstone, M. A., The structure and function of mammalian membrane-attack complex/perforin-like proteins. *Tissue Antigens.* **2010***, 76*, 341-351.

15. Voskoboinik, I.; Whisstock, J. C.; Trapani, J. A., Perforin and granzymes: function, dysfunction and human pathology. *Nat. Rev. Immunol.* **2015***, 15*, 388.

16. Hotze, E. M.; Tweten, R. K., Membrane assembly of the cholesterol-dependent cytolysin pore complex. *Biochimica Et Biophysica Acta (BBA)-Biomembranes.* **2012***, 1818*, 1028-1038.

17. Ladokhin, A. S., pH-triggered conformational switching along the membrane insertion pathway of the diphtheria toxin T-domain. *Toxins.* **2013***, 5*, 1362-1380.

18. Young, R., Phage lysis: do we have the hole story yet? *Curr. Opin. Microbiol.* **2013***, 16*, 790-797.

19. Walther, T. H.; Gottselig, C.; Grage, S. L.; Wolf, M.; Vargiu, A. V.; Klein, M. J.; Vollmer, S.; Prock, S.; Hartmann, M.; Afonin, S., Folding and self-assembly of the TatA translocation pore based on a charge zipper mechanism. *Cell.* **2013***, 152*, 316-326.

20. Bayburt, T. H.; Grinkova, Y. V.; Sligar, S. G., Self-assembly of discoidal phospholipid bilayer nanoparticles with membrane scaffold proteins. *Nano Lett.* **2002***, 2*, 853-856.

21. Bayburt, T. H.; Sligar, S. G., Membrane protein assembly into Nanodiscs. *FEBS Lett.* **2010***, 584*, 1721-1727.

22. McLean, M. A.; Gregory, M. C.; Sligar, S. G., Nanodiscs: a controlled bilayer surface for the study of membrane proteins. *Annu. Rev. Biophys.* **2018***, 47*, 107-124.

23. Denisov, I. G.; Grinkova, Y. V.; Lazarides, A. A.; Sligar, S. G., Directed self-assembly of monodisperse phospholipid bilayer Nanodiscs with controlled size. *J. Am. Chem. Soc.* **2004***, 126*, 3477-3487.

24. Ritchie, T. K.; Grinkova, Y. V.; Bayburt, T. H.; Denisov, I. G.; Zolnerciks, J. K.; Atkins, W. M.; Sligar, S. G., Chapter 11 - Reconstitution of membrane proteins in phospholipid bilayer nanodiscs. *Methods Enzymol.* **2009***, 464*, 211-231.

25. Hagn, F.; Wagner, G., Structure refinement and membrane positioning of selectively labeled OmpX in phospholipid nanodiscs. *J. Biomol. NMR.* **2015***, 61*, 249-260.

26. Yao, Y.; Nisan, D.; Fujimoto, L. M.; Antignani, A.; Barnes, A.; Tjandra, N.; Youle, R. J.; Marassi, F. M., Characterization of the membrane-inserted C-terminus of cytoprotective BCL-XL. *Protein Expr. Purif.* **2016***, 122*, 56-63.

27. Kijac, A. Z.; Li, Y.; Sligar, S. G.; Rienstra, C. M., Magic-angle spinning solid-state NMR spectroscopy of nanodisc-embedded human CYP3A4. *Biochemistry.* **2007***, 46*, 13696-13703.

28. Gao, Y.; Cao, E.; Julius, D.; Cheng, Y., TRPV1 structures in nanodiscs reveal mechanisms of ligand and lipid action. *Nature.* **2016***, 534*, 347.

29. Zhang, M.; Huang, R.; Ackermann, R.; Im, S. C.; Waskell, L.; Schwendeman, A.; Ramamoorthy, A., Reconstitution of the Cytb(5)-CytP450 Complex in Nanodiscs for Structural Studies using NMR Spectroscopy. *Angew. Chem. Int. Ed.* **2016***, 55*, 4497-4499.

30. Denisov, I. G.; Sligar, S. G., Nanodiscs in Membrane Biochemistry and Biophysics. *Chem. Rev.* **2017***, 117*, 4669-4713.

31. Nasr, M. L.; Baptista, D.; Strauss, M.; Sun, Z. J.; Grigoriu, S.; Huser, S.; Pluckthun, A.; Hagn, F.; Walz, T.; Hogle, J. M.; Wagner, G., Covalently circularized nanodiscs for studying membrane proteins and viral entry. *Nat. Methods.* **2017***, 14*, 49-52.

32. Knewtson, K. E.; Perera, C.; Hymel, D.; Gao, Z.; Lee, M. M.; Peterson, B. R., Antibody–Drug Conjugate that Exhibits Synergistic Cytotoxicity with an Endosome–Disruptive Peptide. *ACS Omega.* **2019***, 4*, 12955-12968.

33. Meyer, C.; Reusser, F., A polypeptide antibacterial agent isolated fromTrichoderma viride. *Experientia.* **1967***, 23*, 85-86.

34. Mathew, M.; Balaram, P., A helix dipole model for alamethicin and related transmembrane channels. *FEBS Lett.* **1983***, 157*, 1-5.

35. Pieta, P.; Mirza, J.; Lipkowski, J., Direct visualization of the alamethicin pore formed in a planar phospholipid matrix. *Proc. Natl. Acad. Sci. U.S.A.* **2012***, 109*, 21223-21227.

36. Abbasi, F.; Leitch, J. J.; Su, Z. F.; Szymanski, G.; Lipkowski, J., Direct visualization of alamethicin ion pores formed in a floating phospholipid membrane supported on a gold electrode surface. *Electrochimica Acta.* **2018***, 267*, 195-205.

37. Tieleman, D. P.; Berendsen, H. J. C.; Sansom, M. S. P., An alamethicin channel in a lipid bilayer: Molecular dynamics simulations. *Biophys. J.* **1999***, 76*, 1757-1769.

38. Fox, R. O.; Richards, F. M., A Voltage-Gated Ion Channel Model Inferred from the Crystal-Structure of Alamethicin at 1.5-a Resolution. *Nature.* **1982***, 300*, 325-330.

39. Javadpour, M. M.; Juban, M. M.; Lo, W.-C. J.; Bishop, S. M.; Alberty, J. B.; Cowell, S. M.; Becker, C. L.; McLaughlin, M. L., De novo antimicrobial peptides with low mammalian cell toxicity. *J. Med. Chem.* **1996***, 39*, 3107-3113.

40. Dawson, C.; Drake, A.; Helliwell, J.; Hider, R., The interaction of bee melittin with lipid bilayer membranes. *Biochimica et Biophysica Acta (BBA)-Biomembranes.* **1978***, 510*, 75-86.

41. Terwilliger, T. C.; Weissman, L.; Eisenberg, D., The structure of melittin in the form I crystals and its implication for melittin's lytic and surface activities. *Biophys. J.* **1982***, 37*, 353-361.

42. Ladokhin, A. S.; Selsted, M. E.; White, S. H., Sizing membrane pores in lipid vesicles by leakage of co-encapsulated markers: Pore formation by melittin. *Biophys. J..* **1997***, 72*, 1762-1766.

43. Leveritt III, J. M.; Pino-Angeles, A.; Lazaridis, T., The structure of a melittin-stabilized pore. *Biophys. J.* **2015***, 108*, 2424-2426.

44. Yang, L.; Harroun, T. A.; Weiss, T. M.; Ding, L.; Huang, H. W., Barrel-stave model or toroidal model? A case study on melittin pores. *Biophys. J.* **2001***, 81*, 1475-1485.

45. Wu, Z.; Wagner, M. A.; Zheng, L.; Parks, J. S.; Shy, J. M., 3rd; Smith, J. D.; Gogonea, V.; Hazen, S. L., The refined structure of nascent HDL reveals a key functional domain for particle maturation and dysfunction. *Nat. Struct. Mol. Biol.* **2007***, 14*, 861-868.

46. Kang, H. J.; Coulibaly, F.; Clow, F.; Proft, T.; Baker, E. N., Stabilizing isopeptide bonds revealed in gram-positive bacterial pilus structure. *Science.* **2007***, 318*, 1625-1628.

47. Zakeri, B.; Fierer, J. O.; Celik, E.; Chittock, E. C.; Schwarz-Linek, U.; Moy, V. T.; Howarth, M., Peptide tag forming a rapid covalent bond to a protein, through engineering a bacterial adhesin. *Proc. Natl. Acad. Sci. U. S. A.* **2012***, 109*, E690-E697.

48. Wikoff, W. R.; Liljas, L.; Duda, R. L.; Tsuruta, H.; Hendrix, R. W.; Johnson, J. E., Topologically linked protein rings in the bacteriophage HK97 capsid. *Science.* **2000***, 289*, 2129-2133.

49. Oke, M.; Carter, L. G.; Johnson, K. A.; Liu, H.; McMahon, S. A.; Yan, X.; Kerou, M.; Weikart, N. D.; Kadi, N.; Sheikh, M. A., The Scottish structural proteomics facility: targets, methods and outputs. *J. Struct. Funct. Genomics.* **2010***, 11*, 167-180.

50. Hagan, R. M.; Björnsson, R.; McMahon, S. A.; Schomburg, B.; Braithwaite, V.; Bühl, M.; Naismith, J. H.; Schwarz-Linek, U., NMR spectroscopic and theoretical analysis of a spontaneously formed Lys–Asp isopeptide bond. *Angew. Chem. Int. Ed.* **2010***, 49*, 8421-8425.

51. Kang, H. J.; Baker, E. N., Intramolecular isopeptide bonds: protein crosslinks built for stress? *Trends Biochem. Sci.* **2011***, 36*, 229-237.

52. Schoene, C.; Fierer, J. O.; Bennett, S. P.; Howarth, M., SpyTag/SpyCatcher cyclization confers resilience to boiling on a mesophilic enzyme. *Angew. Chem. Int. Ed. Engl.* **2014***, 53*, 6101-6104.

53. Si, M.; Xu, Q.; Jiang, L.; Huang, H., SpyTag/SpyCatcher Cyclization Enhances the Thermostability of Firefly Luciferase. *PLoS One.* **2016***, 11*, e0162318.

54. Sun, X. B.; Cao, J. W.; Wang, J. K.; Lin, H. Z.; Gao, D. Y.; Qian, G. Y.; Park, Y. D.; Chen, Z. F.; Wang, Q., SpyTag/SpyCatcher molecular cyclization confers protein stability and resilience to aggregation. *New Biotechnol.* **2019***, 49*, 28-36.

55. Wang, Y.; Tian, J.; Xiao, Y.; Wang, Y.; Sun, H.; Chang, Y.; Luo, H., SpyTag/SpyCatcher cyclization enhances the thermostability and organic solvent tolerance of L-phenylalanine aldolase. *Biotechnol. Lett.* **2019***, 41*, 987-994.

56. Wang, J.; Wang, Y.; Wang, X.; Zhang, D.; Wu, S.; Zhang, G., Enhanced thermal stability of lichenase from Bacillus subtilis 168 by SpyTag/SpyCatcher-mediated spontaneous cyclization. *Biotechnol. Biofuels.* **2016***, 9*, 79.

57. Li, L.; Fierer, J. O.; Rapoport, T. A.; Howarth, M., Structural analysis and optimization of the covalent association between SpyCatcher and a peptide Tag. *J. Mol. Biol.* **2014***, 426*, 309-317.

58. Marcink, T. C.; Simoncic, J. A.; An, B.; Knapinska, A. M.; Fulcher, Y. G.; Akkaladevi, N.; Fields, G. B.; Van Doren, S. R., MT1-MMP Binds Membranes by Opposite Tips of Its beta Propeller to Position It for Pericellular Proteolysis. *Structure.* **2019***, 27*, 281-292 e286.

59. Schneider, C. A.; Rasband, W. S.; Eliceiri, K. W., NIH Image to ImageJ: 25 years of image analysis. *Nat. Methods.* **2012***, 9*, 671-675.

60. K., G.; White, M. A.; Stoilova-McPhie, S., Reversible stacking of lipid nanodiscs for structural studies of clotting factors. *Nanotecnol. Rev.* **2017***, 6*, 139-148.

61. Mihajlovic, M.; Lazaridis, T., Antimicrobial peptides in toroidal and cylindrical pores. *Biochim. Biophys. Acta.* **2010***, 1798*, 1485-1493.

62. Shoulders, C. C.; Kornblihtt, A. R.; Munro, B. S.; Baralle, F. E., Gene structure of human apolipoprotein A1. *Nucleic Acids Res.* **1983***, 11*, 2827-2837.

Chapter 3

Synthesis of fluorophores that target the endoplasmic reticulum of living mammalian cells

3.1. Introduction

The endoplasmic reticulum (ER) has a remarkably complex structure that generally contributes at least half of all membranes of animal cells. The ER is a fine interconnected network of tubules and sac-like structures throughout the cytoplasm and close to the nuclear membrane. The peripheral ER includes smooth tubules and rough sheets.[1,2] Processes essential for cellular maintenance and survival occur on and in this organelle. The external surface of the ER captures ribosomes involved in translation of membrane bound and secreted proteins, whereas the single internal space, termed the lumen, stores intracellular calcium,[3] carbohydrate metabolism,[4] regulates synthesis, folding,[5] and posttranslational processing of proteins in the secretory pathway,[6] and is a major site of cellular lipid biosynthesis.[7,8]

Stressful conditions such as hypoxia, oxidants or reductants, glucose deprivation, altered calcium regulation, viral infection, and expression of aberrant proteins can cause unfolded proteins to accumulate in the ER.[9] These stressors include changes in redox status due to hypoxia, oxidants or reductants, glucose deprivation, altered calcium regulation, viral infection, and expression of aberrant proteins. This triggers an unfolded protein response (UPR) in the ER that initiates complex signaling pathways. These pathways either promote adaptive responses such as upregulation of protective proteins,

or cellular death through apoptosis or even necrosis when stress is excessive.[10] Numerous pathologies are associated with ER stress including neurodegenerative disease, stroke, heart disease, diabetes, and cancer.[11-14] Consequently, agents that modulate ER stress are of substantial therapeutic interest. Some small molecules accumulate selectively in the ER. These compounds are generally amphipathic and moderately lipophilic.[15]

Structures of highly fluorescent[16] molecular probes that allow selective imaging of ER by microscopy are shown in Figure 3.1. These compounds include ER Tracker Blue-White DPX,[17] ER Tracker Green, ER Tracker Red, BODIPY Nile Red,[18] ER Thermo Yellow,[19] and fluorinated hydrophobic rhodols.[20] Some of these compounds are thought[16,21,22] to selectively accumulate in the ER because of the cholesterol-poor lipid composition of ER membranes.[23] The selectivity of these compounds for the ER has been proposed[15,21] to involve association with lipids comprising the ER membranes.[23] Despite the ER membrane having a surface area that is proposed to be as much as 30-fold greater than the plasma membrane, only 0.5-1% of the total cellular cholesterol is contained in the ER verses the 30-40% of the total cellular cholesterol contained in the plasma membrane.[24,25] The cholesterol content of other organelles (Golgi, mitochondria, lysosomes, etc) is intermediate between these two extremes.[23] Other fluorescent ER probes, such as ER Tracker Green and ER Tracker Red (Figure 3.1), link the BODIPY fluorophore to glibenclamide. This compound binds to sulphonylurea receptors of ATP-sensitive potassium channels that are abundant on the cytosolic face of ER membranes.[26] However, binding to these channels can alter ER function by perturbing calcium homeostasis,[27] and probes of the ER that do not bind potassium channels may be

advantageous for imaging and delivery applications. Other drawbacks of many commercially available probes of the ER relate to their structural complexity and associated high cost, typically in the range of thousands of dollars per milligram.

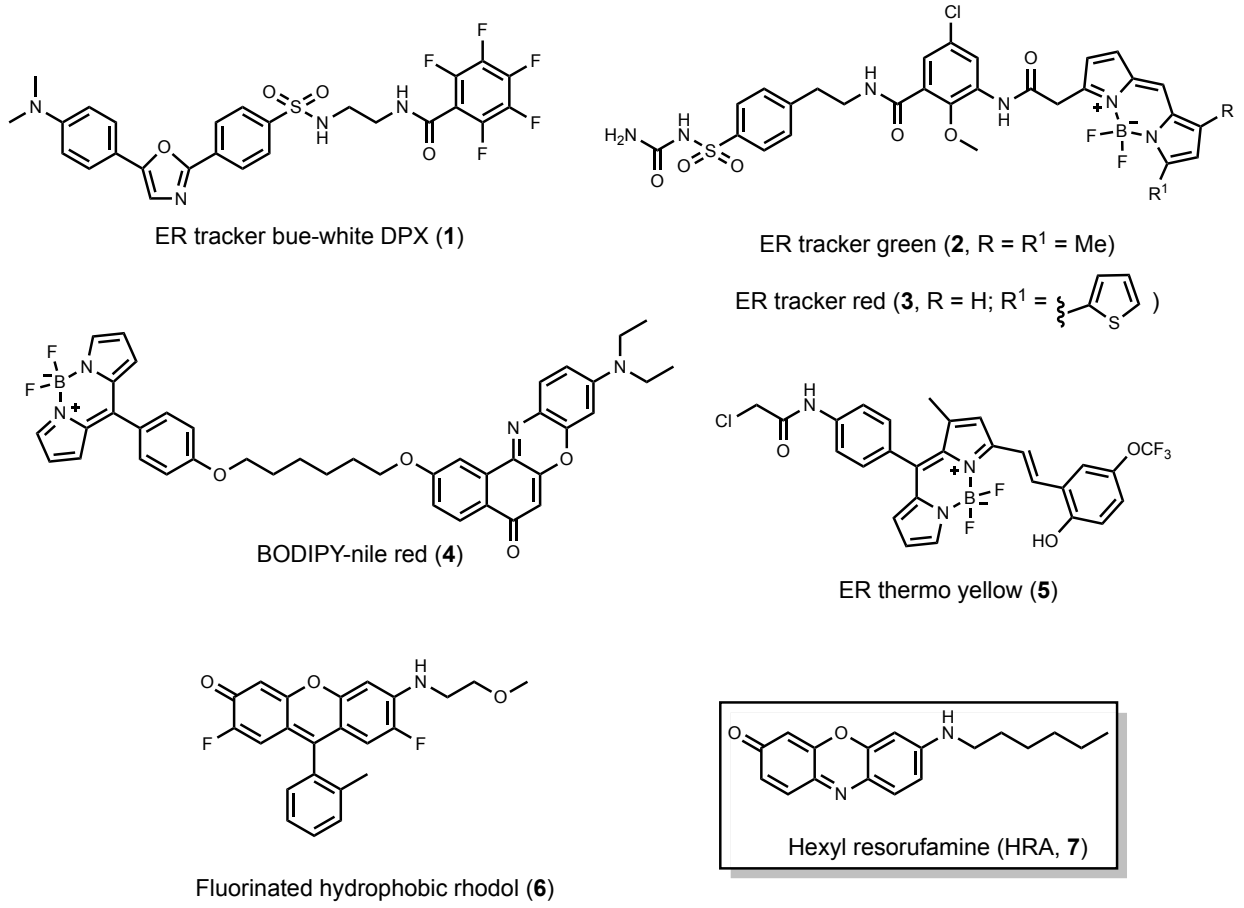

Figure 3.1. Structures of fluorescent molecular probes that selectively accumulate in the ER of mammalian cells. Hexyl resorufamine (HRA) is a novel fluorescent chemotype.

The design of hexyl resorufamine (HRA) was inspired by structurally related fluorinated hydrophobic rhodols such as **6** that selectively accumulate in endoplasmic reticulum,[20] as shown by Dr. Matt Meinig and Dr. Liqiang Fu, a previous graduate student and postdoctoral fellow in the Peterson group. Here, we investigated the utility of resorufamines as a counterstain for cells expressing enhanced green fluorescent protein (EGFP). We investigated the cytotoxicity of resorufamines towards HeLa cells, and their

specificity for the ER in living and fixed HeLa cells.[28] In these studies, some of the cell-based assays were conducted by Dr. Zhe Gao, a previous graduate student in the Peterson group. Dr. Digamber Rane, a post-doc in the Peterson group, helped optimize the synthesis of these molecular probes.

3.2. Synthesis of hydrophobic resorufamines

To develop new molecular probes of the ER, we investigated the use of resorufin (**8**, Scheme 1) as a starting material. This compound has several attractive features as a building block: it is relatively inexpensive (~$60/g), red fluorescent (Ex. = 572 nm; Em. = 585 nm), has a high extinction coefficient (56,000 M^{-1} cm^{-1}), and quantum yield (0.74) when deprotonated (pKa 5.8).[29] Moreover, O-alkyl derivatives of resorufin,[30,31] and the resorufin N-oxide termed resazurin (Alamar blue),[32] have been employed in a variety of bioassays.[33] However, to our knowledge, only one analogue has been described in a peer reviewed journal that replaces the phenol of resorufin with a nitrogen atom (in the form of the azide).[34]

This probe can be prepared in only two steps from the commercially available fluorophore resorufin. We previously used Buchwald-Hartwig amination chemistry to convert the fluorophore Pennsylvania Green[35-37] to N-alkyl rhodols such as **6**, and we envisioned using a similar approach to access N-alkyl resorufamines for studies of the subcellular distribution of these structurally related compounds.

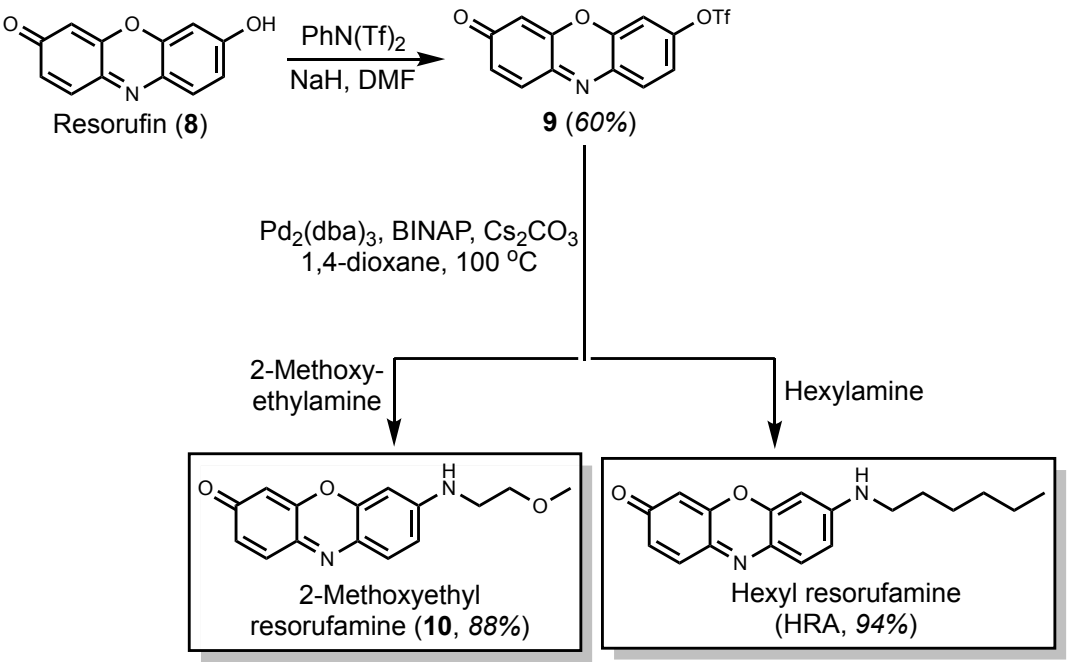

Scheme 3.1. The structure of resorufin and synthesis of resorufamine derivatives.

As shown in Scheme 3.1, resorufin (**8**) was converted to the triflate (**9**)[38] to provide a reactive building block. This triflate was used to prepare resorufamines by reaction with alkylamines under palladium-catalyzed conditions. Because ER Tracker Blue-White DPX is a highly hydrophobic (cLogD (pH 7.4) = 4.0) membrane associated probe, similar in hydrophobicity to **6** (cLogD (pH 7.4) = 3.9), we reasoned that novel probes that bind ER membranes should be of comparable hydrophobicity. Additionally, we hypothesized that the inclusion of straight chain alkanes might favor interactions with phospholipids that are prevalent in ER membranes. Correspondingly, a hydrophobic hexyl substituent was installed to provide the similarly hydrophobic hexyl resorufamine (HRA, cLogD (pH 7.4) = 3.8). As a control, by installing the same 2- methoxyethyl substituent found in **6**, we also prepared the structurally related 2-methoxyethyl resorufamine (**10**), but this compound was predicted to be substantially more polar (cLogD (**10**, pH 7.4) = 1.5).

3.3. Photophysical properties of hydrophobic resorufamines

To examine the photophysical properties of hydrophobic resorufamines, we obtained absorbance and fluorescence emission spectra in PBS, ethanol, and octanol. Spectroscopic studies of HRA and **10** revealed high fluorescence in organic solvents such as ethanol and octanol (Figure 3.2). However, their fluorescence was substantially weaker in aqueous buffers, particularly with HRA, which showed a very broad absorbance spectrum in phosphate buffered saline (PBS), suggesting aggregation of this more hydrophobic fluorophore in aqueous solution (Figure 2, panel A). We measured the quantum yield of HRA in PBS and ethanol, relative[39] to rhodamine 6G, and the extinction coefficient in EtOH and PBS (Figure 3.3). Measurement of extinction coefficients, and quantum yields relative[39] to rhodamine 6G, revealed that both HRA (Abs. λ_{max} = 565 nm; Ex. λ_{max} = 614 nm, ε. 34,300 M^{-1} cm^{-1}, Φ = 0.70, in ethanol) and **10** (Abs. λ_{max} = 565 nm; Ex. λ_{max} = 605 nm, ε. 31,600 M^{-1} cm^{-1}, Φ = 0.63, in ethanol) exhibit excellent spectral properties for fluorescence microscopy, and since their emission is red-shifted compared to resorufin, they should be highly orthogonal to many blue and green fluorophores commonly used to study cellular biology.

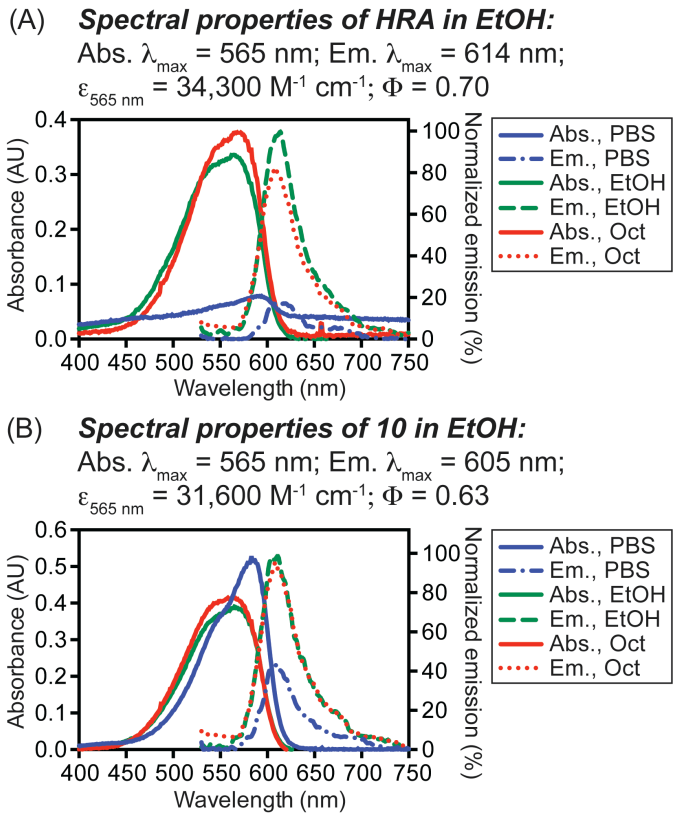

Figure 3.2. Photophysical properties and spectra of the resorufamines HRA (panel A) and **10** (panel B) in aqueous phosphate-buffered saline (PBS, pH 7.4), ethanol (EtOH), and octanol (Oct.). Absorbance (Abs.) spectra were acquired at 10 mM (1% DMSO). Fluorescence emission (Em.) spectra were acquired at 10 nM (Ex. 510 nm, 0.1% DMSO), with intensities normalized to the maximal fluorescence observed in ethanol.

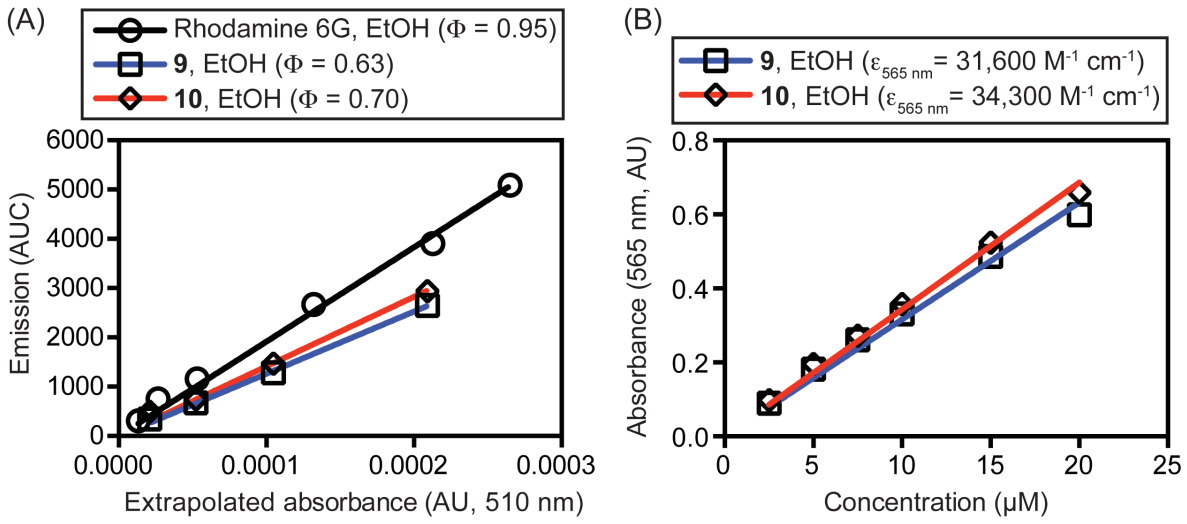

Figure 3.3. Data and linear regression used to determine quantum yields (Panel A) and molar extinction coefficients (Panel B) of **9** and HRA (**10**) in ethanol (1% DMSO).

3.4. Confocal laser scanning microscopy of living HeLa cells treated with resorufamines

To examine effects on living cells, the human cervical carcinoma cell line HeLa was treated with HRA and **10** for 30 min, followed by imaging by confocal laser scanning microscopy. As shown in Figure 3.4, these experiments revealed accumulation of both of these compounds in tubular subcellular structures. However, probe **10** required at least a 10-fold higher concentration than HRA to generate comparable cellular fluorescence, and consistent with its greater fluorescence in PBS, the background signal in media was much higher for **10** than HRA. In contrast, even at concentrations as low as 100 nM, HRA exhibited substantially higher fluorescence in these compartments, and its low background fluorescence in aqueous media obviated the need to wash cells prior to imaging. The tubular structures labeled by these compounds were identified as the ER by colocalization with the spectrally orthogonal organelle marker ER Tracker DPX Blue-White DPX.[17] These studies demonstrated that HRA has particular promise as a novel molecular probe of the ER, since it specifically accumulates in this organelle in living cells with high potency comparable to ER Tracker Blue-White DPX.

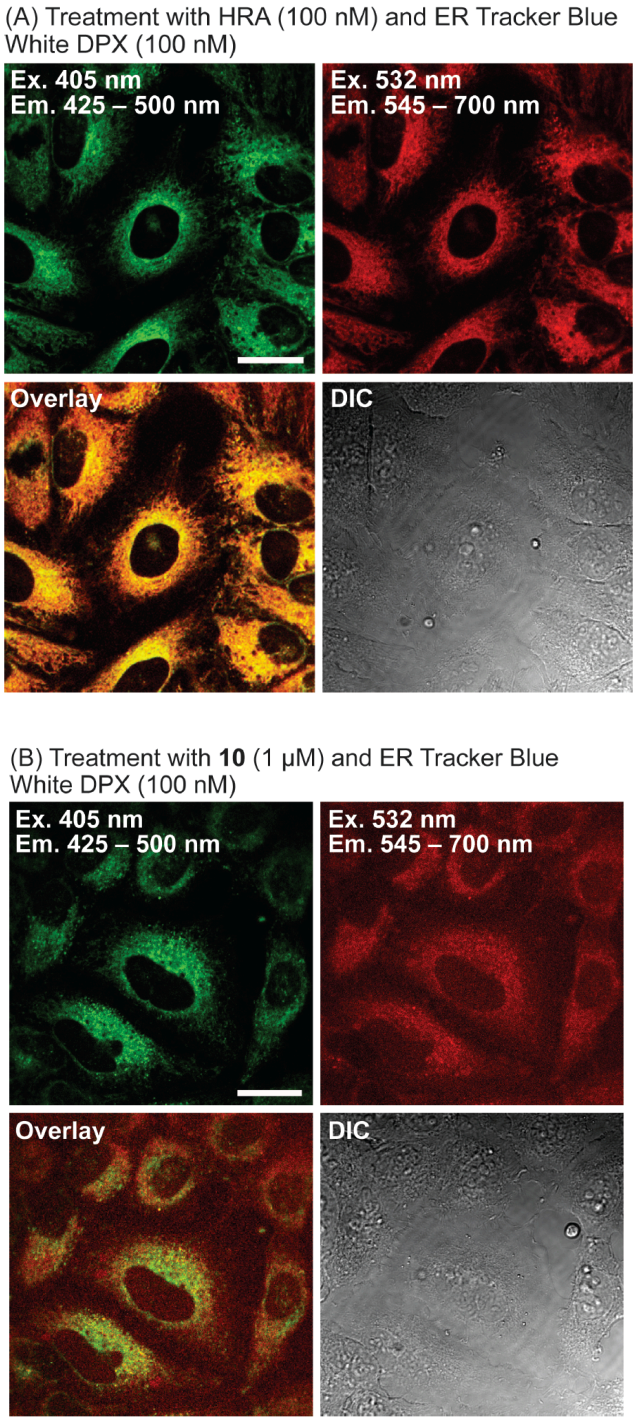

Figure 3.4. Confocal laser scanning and differential interference contrast (DIC) micrographs of living HeLa cells treated with ER-tracker Blue-White DPX (100 nM, 0.5 h) and HRA (Panel A, 100 nM, 0.5 h) or **10** (Panel B, 1 mM, 0.5 h). The fluorescence emission of ER tracker Blue-White DPX can be observed in the upper left panels and the fluorescence emission of the spectrally orthogonal resorufamines can be observed in the upper right panels. Colocalization of the fluorophores is shown in yellow in the lower left panels. Scale bar = 25 mm.

3.5. Confocal laser scanning microscopy of fixed HeLa Cells treated with resorufamines

To examine effects on fixed cells, the human cervical carcinoma cell line HeLa was treated with paraformaldehyde followed by incubation with Triton X-100 in PBS. As shown in Figure 3.5, it was observed that in these fixed cells, HRA was superior to ER tracker Blue-White DPX as a fluorescent probe. It can be noticed that the intensity of green fluorescence given by ER tracker blue-white is comparatively lesser than HRA. This compatibility of HRA with cellular fixation protocols suggests another potential advantage of this novel fluorescent probe as a tool for studies of the ER.

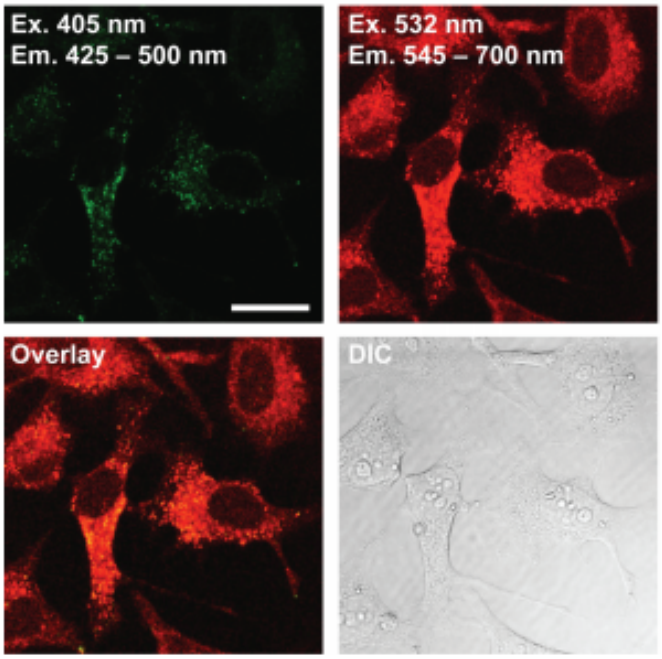

Figure 3.5. Confocal laser scanning and differential interference contrast (DIC) micrographs of fixed HeLa cells treated with ER-tracker Blue-White DPX (100 nM, 0.5 h) and HRA (100 nM, 0.5 h). The fluorescence emission of ERtracker Blue-White DPX can be observed in the upper left panels and the fluorescence emission of the spectrally orthogonal resorufamines can be observed in the upper right panels. Colocalization of the fluorophores is shown in yellow in the lower left panels. Scale bar = 25 mm.

3.6. Cellular toxicity of HeLa cells treated with resorufamines

We examined the cytotoxicities of HRA and **10** towards HeLa cells treated with these compounds for 48 h (Figure 3.6). As a toxic positive control, the tubulin-binding plant natural product colchicine[40] was used, with cellular viability measured by flow cytometry. As expected, colchicine was highly toxic (IC50 = 6 nM) under these conditions. Interestingly probe **10** (IC_{50} = 1 mM) was at least 10-fold more toxic than HRA (IC_{50} > 10 mM), illustrating another potential advantage of HRA over **10** as a molecular probe of the ER. Even after continuous treatment for 48 h at concentrations (100 nM) that can be used to image the ER by confocal microscopy, HRA was non-toxic.

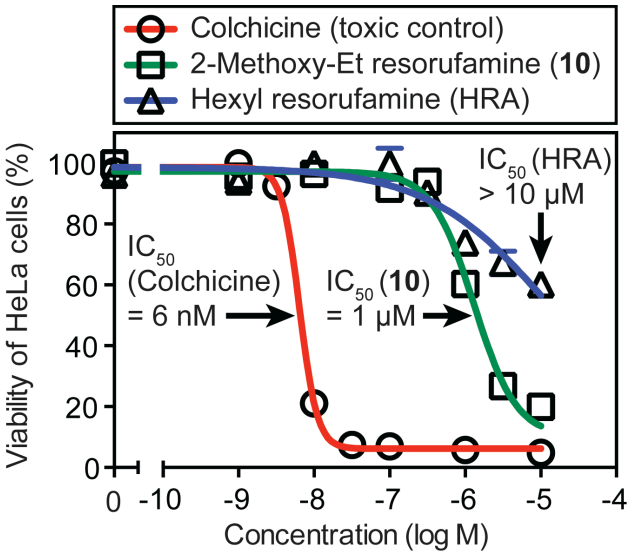

Figure 3.6. Cytotoxicity of compounds towards HeLa cells, after 48 h in culture, as analyzed by flow cytometry.

3.7. Transient transfection of HeLa cells

To further explore HRA as a probe of the ER, we investigated its utility as a counterstain for cells expressing enhanced green fluorescent protein (EGFP). To express EGFP in HeLa cells, we transiently transfected this cell line with a previously reported[41]

plasmid construct termed Str-KDEL_SBP-EGFP-GPI that can be used to synchronize secretory protein traffic in populations of cells (Figure 3.7).

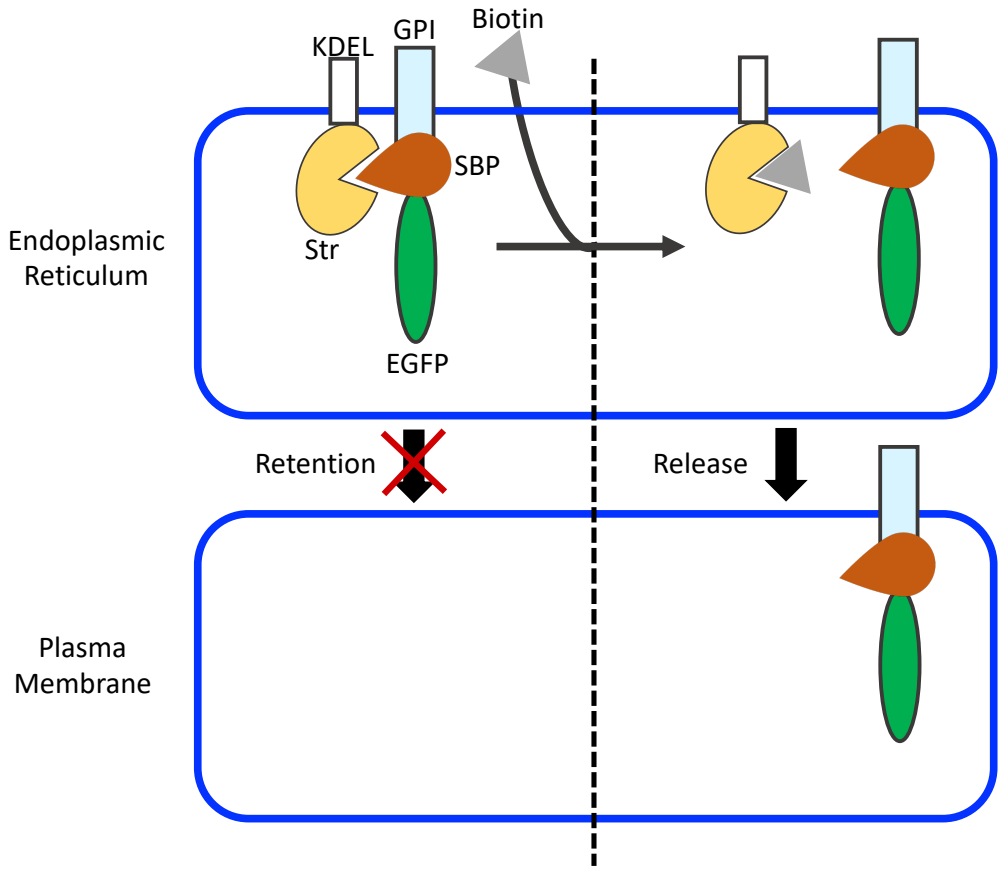

Figure 3.7. Cartoon representation HeLa cells transiently transfected with Str-KDEL_SBP-EGFP-GPI. Treatment with biotin releases SBP-EGFP-GPI from the ER to plasma membrane.

This construct encodes two different proteins bearing signal peptides that direct them into the ER: one is the protein streptavidin (Str) fused to the ER retention signal sequence KDEL; the second is a streptavidin binding peptide (SBP) fused to EGFP linked to a C-terminal peptide that will be modified with a GPI membrane anchor. If expressed alone, the signal sequence of the SBP-EGFP-GPI protein will cause its translocation into the ER for eventual secretion to the plasma membrane, where the attached GPI lipids will

result in localization of EGFP on the cell surface. However, coexpression with the Str-KDEL protein in the ER results in binding of Str to SBP, which traps the EGFP fusion protein in this organelle. Release of the EGFP fusion protein from the ER-localized Str protein can be accomplished by addition of the small molecule biotin to the cell culture media as a competitor. As shown in Figure 3.8, we found that transient transfection of HeLa cells with Str-KDEL_SBP-EGFP-GPI resulted in green fluorescence predominantly localized to the ER as imaged by colocalization with HRA. Moreover, addition of biotin to these transfected cells for 1 h triggered secretion of EGFP from the ER to the cellular plasma membrane, which could be observed as a substantial change in protein subcellular localization (Figure 3.8, compare panels A and B). These experiments confirmed that HRA is spectrally orthogonal to EGFP for studies by confocal microscopy, and it can be used as an ER counterstain in these types of experiments. Consequently, HRA may be useful for image-based screens for molecules that affect protein transport to and from the ER.

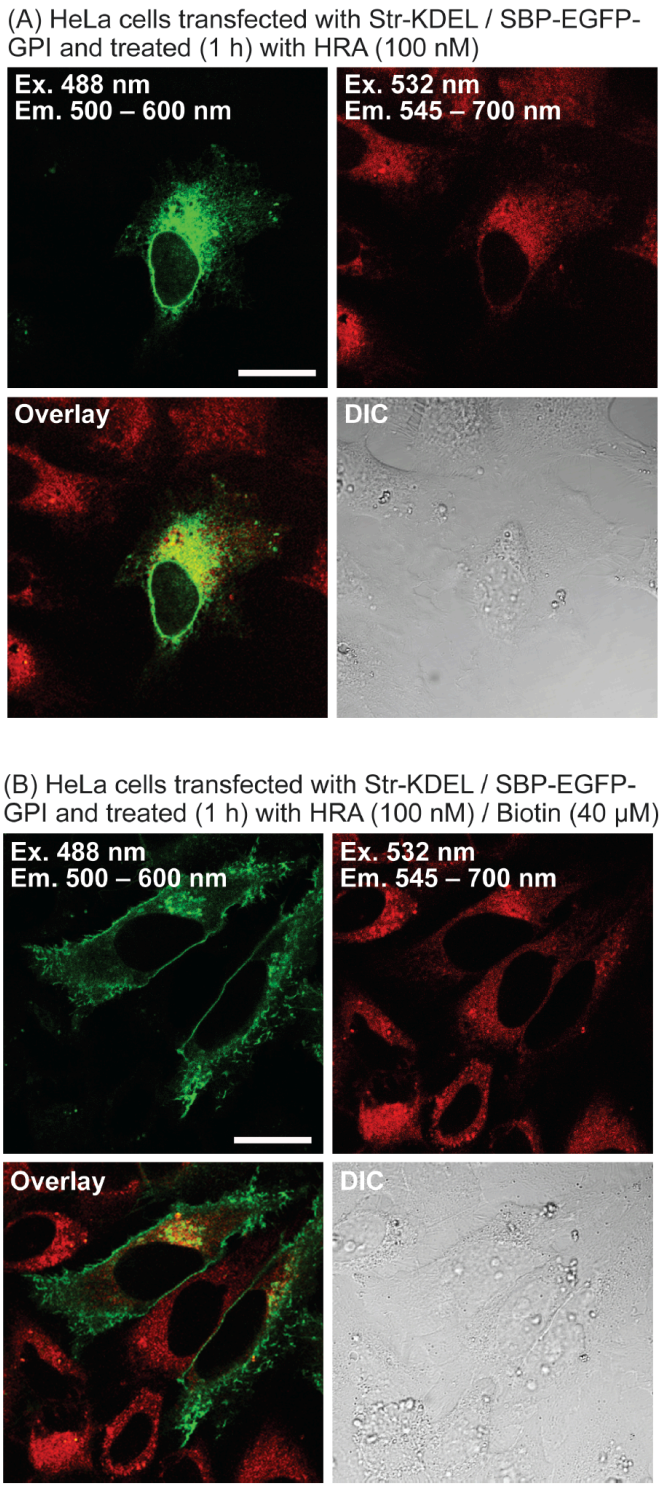

Figure 3.8. Panels A-B. Confocal laser scanning and differential interference contrast (DIC) micrographs of living HeLa cells.

Cells were transiently transfected with a plasmid encoding both the Str-KDEL and SBP-EGFP-GPI proteins and treated with HRA (100 nM, 1 h) as a red fluorescent ER marker. In Panel B, the small molecule biotin (40 μM) was additionally added for 1 h to release SBP-EGFP-GPI from the ER into the secretory pathway. The fluorescence emission of EGFP can be observed in the upper left panel and the fluorescence emission of the spectrally orthogonal HRA can be observed in the upper right panel. Colocalization of fluorophores is shown in yellow in the lower left panel. Scale bar = 25 mm.

3.8. Conclusions and future directions

We synthesized and investigated *N*-alkyl resorufamines as a novel fluorescent chemotype. These compounds were designed based on structural similarity to fluorinated hydrophobic rhodol fluorophores[20] that are known to accumulate in the ER of mammalian cells, Two resorufamines bearing hexyl (HRA) and 2- methoxyethyl (**10**) substituents could be readily prepared in only two steps from the commercially available fluorophore resorufin, making them highly cost-effective molecular probes. The fluorescence emission of these compounds is red-shifted compared to resorufin, making them spectrally orthogonal to many blue and green fluorophores, but they retain high quantum yields. Although both HRA and **10** accumulate in the ER of HeLa cells, HRA proved to be a superior molecular probe, with low background cellular fluorescence, high potency, and low toxicity. These advantages of HRA are correlated with its higher hydrophobicity, as evidenced by its calculated (ChemAxon software) octanol-water distribution coefficient

(cLogD, pH 7.4) of 3.8. This high hydrophobicity is very similar to ER-associated rhodol 6 (cLogD (pH 7.4). 3.9) and ER Tracker Blue-White DPX (cLogD (pH 7.4) = 4.0).

In contrast the calculated distribution coefficient of resorufamine **10** (cLogD (pH 7.4)) is 1.5, indicating substantially greater polarity, which limits its association with membranes and increases its background fluorescence in aqueous media. These differences in polarity are also evident in major changes in the absorbance spectra of HRA in organic solvents compared with PBS, where a substantial broadening, likely due to aggregation, is observed. Taken together, the cellular and physicochemical properties of HRA are consistent with its association with the unique membranes of the ER. Consequently, its mechanism of subcellular localization is likely to be similar to that of other hydrophobic probes such as ER Tracker Blue-White DPX. However, when compared with ER Tracker Blue-White DPX, HRA exhibited better cellular staining of cells that were fixed with paraformaldehyde and Triton X-100, suggesting it may have a broader range of potential applications. Based on its favorable photophysical properties, low cost of production, high potency, and low toxicity, HRA has potential as an important new red fluorescent molecular probe of the ER.

3.9. Experimental

3.9.1. General

^{1}H NMR and ^{13}C NMR spectra were acquired on Bruker DRX-400 or Avance AVIII 500 MHz instruments. ^{19}F NMR was acquired on a Bruker Avance VIII HD 400 MHz instrument. Chemical shifts (δ) are reported in parts per million (ppm) and are referenced to the central solvent peaks of DMSO-d6 (δ 2.50 (1H), 39.52 (13C)) or methanol-d4 (δ 3.31 (1H), 49.0 (13C)). Coupling constants are in Hertz (Hz). Absorbance spectra were

obtained on an Aligent 8452A diode array spectrometer. Fluorescence spectra were acquired with a Perkin-Elmer LS55 Fluorescence Spectrometer. High Resolution mass spectra were obtained at the Mass Spectrometry Laboratory at the University of Kansas on a Micromass LCT Premier time of flight mass spectrometer. All reactions were performed under an inert atmosphere (argon or nitrogen) in flame-dried or oven-dried glassware, or in a glass microwave vial (Biotage, LLC). All anhydrous solvents were either purchased from Sigma Aldrich or dried over a Glass Contour solvent system (Pure Process Technology, LLC). Thin-layer chromatography (TLC) was performed using commercial aluminum backed silica plates (TLC Silica gel 60 F254, Analytical Chromatography). Visualization was accomplished by UV irradiation. Flash chromatography was carried out on normal phase using silica gel (230–400 mesh) or by reverse phase on a Combiflash purification system (HP C18 gold column, 50 g). All reagents were purchased from TCI, Sigma Aldrich or Alfa Aesar. Molar extinction coefficients (ε) were calculated from Beer's Law plots of absorbance λmax versus concentration. Linear least squares fitting of the data (including a zero intercept) was used to determine the slope (corresponding to ε). Values (M^{-1} cm^{-1}) were calculated as follows: Absorbance = ε [concentration (M)] L, where L = 1 cm. Relative quantum yields (Φ) were determined by the method of Williams,[38] where the fluorophores were excited at 510 nm, and the integrated fluorescence emission (530 nm to 800 nm) was quantified (concentrations of 1 nM to 10 nM). Rhodamine 6G (Φ = 0.95 in ethanol) provided the standard.[42,43] The integrated fluorescence emission at a given concentration was plotted against the maximum absorbance of the sample at that concentration determined by extrapolation based on absorbance measurements at higher concentrations. Linear least

squares fitting of the data (including a zero intercept) was used to calculate the slope, which is proportional to the quantum yield. Quantum yields were calculated as follows: $\Phi_x = \Phi_{st}(Grad_x/Grad_{st})(\eta^2_x/\eta^2_{st})$, where Φ_{st} represents the quantum yield of the standard, Φ_x represents the quantum yield of the unknown, Grad is the slope of the best linear fit, and η is the refractive index of the solvent used.

3.9.2. Cell culture

The HeLa (CCL-2) cell line was obtained from ATCC. Dulbecco's Modified Eagle Medium (DMEM, Sigma D5796) was supplemented with FBS (10%, Sigma F0926), penicillin (100 units/L), and streptomycin (100 µg/L, Sigma P4333).

3.9.3. Plasmids

The plasmid Str-KDEL_SBP-EGFP-GPI[41] (pIRESneo3 backbone) was a gift from Franck Perez (Addgene Plasmid #65294). To form a DNA complex, this plasmid DNA (3 µg) was incubated (30 min, room temperature) with the DNA transfection reagent X-tremeGENE HP (9 µL, Roche) in serum free DMEM medium (300 µL). HeLa cells in DMEM were seeded onto an 8-well cover glass slide (Ibidi µSlide, 300 µL, 10,000 cells/well). After incubation at 37 °C for 16 h, the DNA complex (30 µL) was added to each well. After further incubation at 37 °C for 48 h, the cells were washed, further treated with probes, and analyzed by confocal microscopy.

3.9.4. Cellular toxicity

HeLa cells were seeded on a 48-well plate in complete DMEM at 20000 cells/300 µL/well 16 h prior to treatments. All compounds were serial diluted in DMSO and added to media to achieve a 1:1000 dilution factor (0.1% DMSO in each well). The original media was removed from all wells by aspiration and replaced with treatment media (330 µL) at the concentrations indicated. Plates were incubated for 48 h at 37 °C and cells were analyzed in triplicate. Following this incubation period the media was aspirated, and wells were washed with PBS (phosphate-buffered saline, pH 7.4). Wells were further treated with trypsin EDTA solution (50 µL) at 37 °C for 5 min followed by complete DMEM (100 µL). The total cell count for each well was determined by flow cytometry (Accuri C6) using light scattering to identify populations of live cells. Counts of viable cells for each treatment were used to generate dose-response curves that were fitted by non-linear regression (log inhibitor vs. response variable slope 4-parameter model (bottom constraint < 10%, GraphPad Prism 6) to determine IC50 values.

3.9.5. Confocal microscopy of HeLa cells

Cells were added to an 8-well cover glass slide (Ibidi µ-Slide, 300 µL, 20,000 cells/well) and allowed to proliferate for 24 h prior to addition of compounds. Compounds in DMSO stock solutions were serially diluted 1000-fold with complete media (final concentration of 0.1% DMSO) prior to addition to cells. Cells were treated with compounds at 37 °C. Living cells were imaged, without any additional washing steps, using a Leica SPE2 confocal laser-scanning microscope fitted with a 63X objective. ER-Tracker Blue-White DPX (100 nM) was excited with a 405 nm laser and emitted photons

were collected from 425 nm to 500 nm. Resorufamines were excited with a 532 nm laser and emitted photons were collected from 545 nm to 700 nm. EGFP was excited with a 488 nm laser and emitted photons were collected from 500–600 nm.

3.9.6. Synthetic procedures and compound characterization

3-Oxo-3H-phenoxazin-7-yl trifluoromethanesulfonate, resorufin triflate, 9

Resorufin (**8**, 500 mg, 2.34 mmol) was dissolved in anhydrous DMF (12 mL) in a flask wrapped in aluminum foil to protect from light. This flask was cooled to 4 °C in an ice bath and treated with sodium hydride (118 mg, 2.81 mmol), added in a single portion. This mixture was stirred at 4 °C for 30 min. *N*-Phenyl-bis(trifluoromethanesulfonimide) (1.0 g, 2.81 mmol) was added, and the reaction mixture was stirred at 4 °C for 10 min. The reaction mixture was warmed to 22 °C (room temperature) and stirred at room temperature for 24 h. The reaction was monitored by TLC (eluents: ethyl acetate and hexanes). The reaction was quenched with aqueous HCl (1N, 20 mL) and extracted with ethyl acetate (150 mL). The organic layer was further washed with saturated aqueous NaCl (2 × 50 mL), dried over anhydrous $MgSO_4$, and concentrated to dryness. The crude reaction mixture was purified by silica gel chromatography (eluent: ethyl acetate/hexanes) to yield **9** as a yellow solid (488 mg, 60%). ^{1}H NMR (400 MHz, DMSO-d_6): δ 8.00 (m, 1H), 7.84 (m, 1H), 7.60–7.53 (m, 2H), 6.87 (m, 1H); ^{13}C NMR (101 MHz, DMSO-d_6): δ 185.8, 149.9, 149.8, 149.2, 144.2, 135.2 (2 carbons) 132.9, 131.6, 118.6, 118.2 (q, J = 321.4 Hz, CF_3), 110.3, 106.4; ^{19}F NMR (376 MHz, DMSO-d_6) δ −72.5; HRMS (ESI) m/z calcd for $C_{13}H_7F_3NO_5S$ $[M + H]^+$: 345.9997, found: 345.9996.

Procedure for Buchwald-Hartwig amination

Resorufin triflate (**9**, 1.0 equiv), $Pd_2(dba)_3$ (0.1 equiv), BINAP (0.12 equiv), cesium carbonate (2.5 equiv), and amine (1.2 equiv) were weighed in a flame-dried Ar-flushed microwave vial (5 mL) in a glove box. The vial was sealed and anhydrous 1,4-dioxane (0.05 mM) was added. The sealed vial was placed in an oil bath preheated to 100 °C and stirred for 2.5 h. Completion of reaction was confirmed by TLC. The vial was cooled to room temperature and quenched by addition of trifluoroacetic acid (5 equiv). The crude reaction mixture was subjected to reverse phase purification (gradient of acetonitrile/water both containing 0.1% TFA) to yield resorufamines as reddish-brown solids.

7-(Hexylamino)-3H-phenoxazin-3-one, HRA, 7

Following the procedure for Buchwald-Hartwig amination, triflate **9** (34.5 mg, 0.1 mmol), $Pd_2(dba)_3$ (9.15 mg, 0.01 mmol), BINAP (7.47 mg, 0.012 mmol), cesium carbonate (81.45 mg, 0.25 mmol), and hexylamine (20 µL, 0.15 mmol) were weighed in a 5 mL microwave vial. 1,4-Dioxane (2 mL) was added and the reaction mixture was heated at 100 °C for 2.5 h to yield **7** (28 mg, 94%). ^{1}H NMR (400 MHz, methanol-d_4): δ 7.92 (d, J = 9.1 Hz, 1H), 7.79 (d, J = 9.5 Hz, 1H), 7.43–7.29 (m, 1H), 7.15 (dd, J = 9.1, 2.5 Hz, 1H), 7.04–6.90 (m, 2H), 3.62 (t, J = 7.2 Hz, 2H), 1.79 (p, J = 7.3 Hz, 2H), 1.59–1.23 (m, 6H), 1.02–0.84 (m, 3H); ^{13}C NMR (126 MHz, methanol-d_4): δ 170.4, 162.5, 152.5, 149.2, 141.4, 136.5, 135.0, 133.3, 125.5, 120.6, 103.1, 96.1, 46.0, 32.6, 29.6, 27.7, 23.6, 14.3. HRMS (ESI) m/z calcd for $C_{18}H_{21}N_2O_2[M + H]^+$: 297.1603, found: 297.1604.

7-((2-Methoxyethyl)amino)-3H-phenoxazin-3-one, 10

Following the procedure for Buchwald-Hartwig amination, triflate **9** (34.5 mg, 0.1 mmol), $Pd_2(dba)_3$ (9.15 mg, 0.01 mmol), BINAP (7.47 mg, 0.012 mmol), cesium carbonate (81.45 mg, 0.25 mmol), and 2-methoxyethylamine (13 µL, 0.15 mmol) were weighed in a 5 mL microwave vial. 1,4-Dioxane (2 mL) was added and the reaction mixture was heated at 100 °C for 2.5 h to yield **10** (24 mg, 88%). ^{1}H NMR (400 MHz, methanol-d_4): δ 7.87 (d, J = 9.1 Hz, 1H), 7.76 (d, J = 9.5 Hz, 1H), 7.38–7.29 (m, 1H), 7.15–7.09 (m, 1H), 6.98 (d, J = 2.4 Hz, 1H), 6.88 (q, J = 2.3, 1.9 Hz, 1H), 3.80–3.61 (m, 4H), 3.41 (s, 3H); ^{13}C NMR (126 MHz, methanol-d_4) δ170.3, 163.1, 152.4, 149.2, 141.4, 136.6, 135.0, 133.3, 125.5, 120.6, 103.1, 96.8, 71.0, 59.2, 45.9. HRMS (ESI) m/z calcd for $C_{15}H_{15}N_2O_3$ $[M + H]^+$: 271.1083, found: 271.1083.

3.10. References

1. Friedman, J. R.; Voeltz, G. K., The ER in 3D: a multifunctional dynamic membrane network. *Trends Cell Biol.* **2011***, 21*, 709-717.

2. Shibata, Y.; Voeltz, G. K.; Rapoport, T. A., Rough sheets and smooth tubules. *Cell.* **2006***, 126*, 435-439.

3. Clapham, D. E., Calcium signaling. *Cell.* **2007***, 131*, 1047-1058.

4. Hebert, D. N.; Garman, S. C.; Molinari, M., The glycan code of the endoplasmic reticulum: asparagine-linked carbohydrates as protein maturation and quality-control tags. *Trends in Cell Biol.* **2005***, 15*, 364-370.

5. Braakman, I.; Hebert, D. N., Protein folding in the endoplasmic reticulum. *CSH Perspect. Biol.* **2013***, 5*, a013201.

6. Rapoport, T. A., Protein translocation across the eukaryotic endoplasmic reticulum and bacterial plasma membranes. *Nature.* **2007***, 450*, 663.

7. Fagone, P.; Jackowski, S., Membrane phospholipid synthesis and endoplasmic reticulum function. *J. Lipid Res.* **2009***, 50*, S311-S316.

8. Vance, J. E., Phospholipid synthesis and transport in mammalian cells. *Traffic.* **2015***, 16*, 1-18.

9. Sovolyova, N.; Healy, S.; Samali, A.; Logue, S. E., Stressed to death–mechanisms of ER stress-induced cell death. *Biol. Chem.* **2014***, 395*, 1-13.

10. Tabas, I.; Ron, D., Integrating the mechanisms of apoptosis induced by endoplasmic reticulum stress. *Nat. Cell Biol.* **2011***, 13*, 184.

11. Deshaies, R. J., Proteotoxic crisis, the ubiquitin-proteasome system, and cancer therapy. *BMC biol.* **2014***, 12*, 94.

12. Shore, G. C.; Papa, F. R.; Oakes, S. A., Signaling cell death from the endoplasmic reticulum stress response. *Curr. Opin. Cell biol.* **2011***, 23*, 143-149.

13. Kim, I.; Xu, W.; Reed, J. C., Cell death and endoplasmic reticulum stress: disease relevance and therapeutic opportunities. *Nat. Rev. Drug Discov.* **2008***, 7*, 1013.

14. Lin, J. H.; Walter, P.; Yen, T. B., Endoplasmic reticulum stress in disease pathogenesis. *Annu. Rev. Mech. Dis.* **2008***, 3*, 399-425.

15. Colston, J.; Horobin, R.; Rashid-Doubell, F.; Pediani, J.; Johal, K., Why fluorescent probes for endoplasmic reticulum are selective: an experimental and QSAR-modelling study. *Biotech. Histochem.* **2003***, 78*, 323-332.

16. Lavis, L. D.; Raines, R. T., Bright building blocks for chemical biology. *ACS Chem. Biol.* **2014***, 9*, 855-866.

17. Cole, L.; Davies, D.; Hyde, G.; Ashford, A., ER-Tracker dye and BODIPY-brefeldin A differentiate the endoplasmic reticulum and Golgi bodies from the tubular-vacuole system in living hyphae of Pisolithus tinctorius. *J. Microsc.* **2000***, 197*, 239-248.

18. Yang, Z.; He, Y.; Lee, J. H.; Chae, W.-S.; Ren, W. X.; Lee, J. H.; Kang, C.; Kim, J. S., A Nile Red/BODIPY-based bimodal probe sensitive to changes in the micropolarity and microviscosity of the endoplasmic reticulum. *Chem. Comm.* **2014***, 50*, 11672-11675.

19. Arai, S.; Lee, S.-C.; Zhai, D.; Suzuki, M.; Chang, Y. T., A molecular fluorescent probe for targeted visualization of temperature at the endoplasmic reticulum. *Sci. Rep.* **2014***, 4*, 6701.

20. Meinig, J. M.; Fu, L.; Peterson, B. R., Synthesis of fluorophores that target small molecules to the endoplasmic reticulum of living mammalian cells. *Angew. Chem. Int. Ed. Engl.* **2015***, 54*, 9696-9699.

21. Terasaki, M.; Song, J.; Wong, J. R.; Weiss, M. J.; Chen, L. B., Localization of endoplasmic reticulum in living and glutaraldehyde-fixed cells with fluorescent dyes. *Cell.* **1984***, 38*, 101-108.

22. Horobin, R. W.; Stockert, J. C.; Rashid-Doubell, F., Uptake and localisation of small-molecule fluorescent probes in living cells: a critical appraisal of QSAR models and a case study concerning probes for DNA and RNA. *Histochem. Cell Biol.* **2013***, 139*, 623-637.

23. van Meer, G.; de Kroon, A. I., Lipid map of the mammalian cell. *J. Cell Sci.* **2011***, 124*, 5-8.

24. Lange, Y.; Ye, J.; Rigney, M.; Steck, T. L., Regulation of endoplasmic reticulum cholesterol by plasma membrane cholesterol. *J. Lipid Res.* **1999***, 40*, 2264-2270.

25. Maxfield, F. R.; Mesmin, B.; Pipalia, N.; Lamlal, T.; Eliezer, D. (**2011**). Intracellular cholesterol transport. In: Federation of American Societies for Experimental Biology.

26. Zhou, M.; He, H.-J.; Suzuki, R.; Liu, K.-X.; Tanaka, O.; Sekiguchi, M.; Itoh, H.; Kawahara, K.; Abe, H., Localization of sulfonylurea receptor subunits, SUR2A and SUR2B, in rat heart. *J. Histochem. Cytochem.* **2007***, 55*, 795-804.

27. Nelson, T. Y.; Gaines, K.; Rajan, A.; Berg, M.; Boyd, A., Increased cytosolic calcium. A signal for sulfonylurea-stimulated insulin release from beta cells. *J. Biol. Chem.* **1987***, 262*, 2608-2612.

28. Phaniraj, S.; Gao, Z.; Rane, D.; Peterson, B. R., Hydrophobic resorufamine derivatives: potent and selective red fluorescent probes of the endoplasmic reticulum of mammalian cells. *Dyes. Pigments.* **2016***, 135*, 127-133.

29. Bueno, C.; Villegas, M.; Bertolotti, S.; Previtali, C.; Neumann, M.; Encinas, a. V., The excited-state interaction of resazurin and resorufin with aminesin aqueous solutions. Photophysics and photochemical reaction. *Photochem. Photobiol.* **2002***, 76*, 385-390.

30. Burke, M. D.; Thompson, S.; Weaver, R. J.; Wolf, C. R.; Mayers, R. T., Cytochrome P450 specificities of alkoxyresorufin O-dealkylation in human and rat liver. *Biochem. Pharmacol.* **1994***, 48*, 923-936.

31. Kim, S. Y.; Hong, J.-I., Chromogenic and fluorescent chemodosimeter for detection of fluoride in aqueous solution. *Org. Lett.* **2007***, 9*, 3109-3112.

32. O'brien, J.; Wilson, I.; Orton, T.; Pognan, F., Investigation of the Alamar Blue (resazurin) fluorescent dye for the assessment of mammalian cell cytotoxicity. *Eur. J. Biochem.* **2000***, 267*, 5421-5426.

33. Lavis, L. D.; Raines, R. T., Bright ideas for chemical biology. *ACS Chem. Biol.* **2008***, 3*, 142-155.

34. Chen, B.; Lv, C.; Tang, X., Chemoselective reduction-based fluorescence probe for detection of hydrogen sulfide in living cells. *Anal. Bioanal. Chem.* **2012***, 404*, 1919-1923.

35. Mottram, L. F.; Boonyarattanakalin, S.; Kovel, R. E.; Peterson, B. R., The Pennsylvania Green Fluorophore: a hybrid of Oregon Green and Tokyo Green for

the construction of hydrophobic and pH-insensitive molecular probes. *Org. Lett.* **2006***, 8*, 581-584.

36. Mottram, L. F.; Maddox, E.; Schwab, M.; Beaufils, F.; Peterson, B. R., A Concise Synthesis of the Pennsylvania Green Fluorophore and Labeling of Intracellular Targets with O 6-Benzylguanine Derivatives. *Org. Lett.* **2007***, 9*, 3741-3744.
37. Woydziak, Z. R.; Fu, L.; Peterson, B. R., Efficient and scalable synthesis of 4-carboxy-pennsylvania green methyl ester: a hydrophobic building block for fluorescent molecular probes. *Synthesis.* **2014***, 46*, 158-164.
38. Miller, E. W.; Tulyathan, O.; Isacoff, E. Y.; Chang, C. J., Molecular imaging of hydrogen peroxide produced for cell signaling. *Nat. Chem. Biol.* **2007***, 3*, 263.
39. Williams, A. T. R.; Winfield, S. A.; Miller, J. N., Relative fluorescence quantum yields using a computer-controlled luminescence spectrometer. *Analyst.* **1983***, 108*, 1067-1071.
40. Finkelstein, Y.; Aks, S. E.; Hutson, J. R.; Juurlink, D. N.; Nguyen, P.; Dubnov-Raz, G.; Pollak, U.; Koren, G.; Bentur, Y., Colchicine poisoning: the dark side of an ancient drug. *Clin. Toxicol.* **2010***, 48*, 407-414.
41. Boncompain, G.; Divoux, S.; Gareil, N.; De Forges, H.; Lescure, A.; Latreche, L.; Mercanti, V.; Jollivet, F.; Raposo, G.; Perez, F., Synchronization of secretory protein traffic in populations of cells. *Nat. Methods.* **2012***, 9*, 493.
42. Velapoldi, R. A.; Tønnesen, H. H., Corrected emission spectra and quantum yields for a series of fluorescent compounds in the visible spectral region. *J. Fluoresc.* **2004***, 14*, 465-472.

43. Kubin, R. F.; Fletcher, A. N., Fluorescence quantum yields of some rhodamine dyes. *J. Lumin.* **1982**, *27*, 455-462.

Chapter 4

Fluorescence polarization assays of inhibitors of the protein-protein interaction between BfrB and Bfd

4.1. Introduction

Rapid bacterial evolution and the misuse of antibiotics has led to extensive antibiotic resistance. Infections by multi-drug resistant bacteria are a major health concern and these pathogens have become increasing difficult to treat.[1,2] *Pseudomonas aeruginosa* is an example of an antibiotic-resistant bacterium that the World Health Organization (WHO) has included in a critical priority list for new antibiotics.[3] This opportunistic Gram-negative bacterium is a leading cause of nosocomial infections, defined as those acquired under medical care, and accounts for 10% of all hospital-acquired infections.[4] This bacterium colonizes urinary catheters and endotracheal tubes,[5] accelerates lung function decay in cystic fibrosis patients[6] as it easily adapts to its surroundings, including surfaces within hospitals and clinics, making it particularly dangerous in these settings.[7] *P. aeruginosa* primarily affects patients with compromised immune systems, such as those with neutropenia, AIDS, severe burns, and cystic fibrosis.[8] Cystic fibrosis (CF) is congenital, inherited disease characterized by mutations in the gene encoding cystic fibrosis transmembrane conductance regulator (CFTR), a cAMP-regulated chloride channel.[7] Approximately 80% of adult patients with cystic fibrosis are chronically infected with *P. aeruginosa,* and these lung infections are typically associated with morbidity.[9,10] Although recent advances have improved the treatment of

lung infections in CF,[9,11] biofilms and drug resistance continue to hinder treatment strategies. Hence, there is a need for good research in the early stages of drug development, which would lead to a stronger pipeline of antibiotics.

With respect to *P. aeruginosa,* a better understanding of iron uptake by this bacterium could be critical for the discovery of new treatments as it is highly dependent on iron-dependent processes for infectivity and biofilm formation.[12,13] Strategies that interfere with bacterial iron acquisition and homeostasis have potential for the discovery of new antibiotics.[14-17] Iron is an essential cofactor in DNA synthesis, respiration, and nitrogen fixation, as it is able to participate in one-electron transfer reactions that catalyze enzymatic processes.[18,19] Proper regulation of iron homeostasis is critical in nature, since Fe^{2+} can react with O_2 and H_2O_2 to form insoluble Fe^{3+}, reactive hydroxyl radicals, and superoxide via the Haber-Weiss reaction.[20] To avoid the formation of these reactive oxygen species, cells tightly regulate iron acquisition and storage through the use of iron storage proteins and siderophores.[21] The processes of bacterial iron homeostasis involve the acquisition of iron from a host, storage of the obtained iron as the host denies this essential nutrient to invading pathogens, and optimum utilization of the stored iron. These processes are highly regulated for metabolic processes while preventing iron-induced toxicity.[22,23]

Iron is stored in bacteria in bacterial ferritin (Ftn) and bacterioferritin (Bfr),[24-26] which are particularly crucial for survival of bacteria under iron depletion conditions. Bacterioferritins are unique to bacteria and their major functions are to oxidize reactive Fe^{2+} to Fe^{3+}, store the mineral, and release it when needed.[27] Bfr and bacterial Ftn are assembled into a spherical structure consisting of 24 identical subunits with an outer

diameter of ~ 120 Å and an inner diameter of ~ 80 Å, and an interior cavity that can store up to ~ 3000 iron ions in Fe^{3+} form.[28,29] Two subunits are paired to form a dimer with heme, and therefore 12 heme molecules are present in each 24-mer protein.[30] Bfrs contain a ferroxidase center that converts Fe^{2+} to Fe^{3+}. This oxidation step is followed by translocation to the interior cavity, where it is mineralized for storage. Utilizing electrons originating from NADPH, the iron atoms are then reduced and released to the cytosol, a process facilitated by a ferrodoxin reductase and bacterioferritin-associated ferrodoxin (Bfd) (Figure 4.1).[31,32]

The bacterial Ftns and Bfrs have < 20% sequence similarity although they share an identical subunit fold and quaternary structures resulting in a variety of subunit packing 24-mer dynamics and function.[29,33,34] In *P. aeruginosa* (*Pa*), bacterioferritin (BfrB) is the main iron storage protein (Figure 4.1),[34] and this stored iron in BfrB is mobilized by specific interactions with *Pa*-Bfd. *Pa*-Bfd binds to *Pa*-BfrB (K_d = 3 μM) and facilitates iron mobilization by heme-mediated electron transfer.[35] Rivera and coworkers found that this protein-protein interaction consists of a highly complementary interface with a network of hotspots defined by leucines, glutamic acids, and a tyrosine that are conserved across a number of pathogenic species.[36,37]

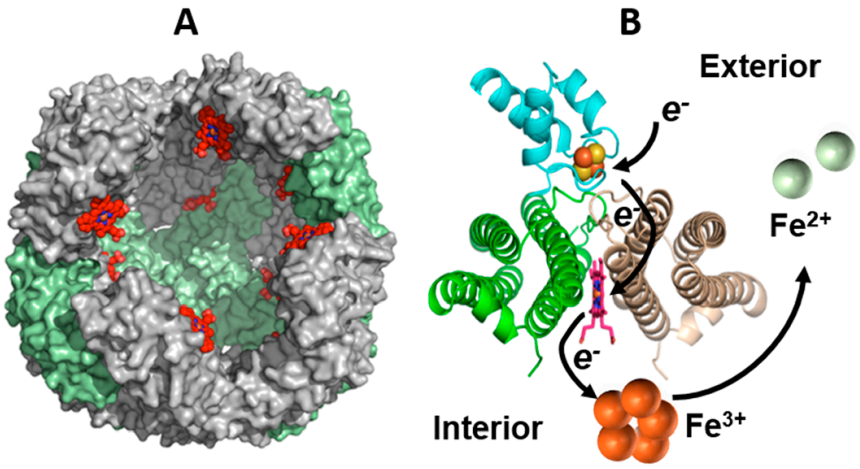

Figure 4.1. Structure and function of BfrB and Bfd.[37] (A) BfrB is a nearly spherical molecule assembled from 24 identical subunits and 12 hemes. This 24-mer assembly has a hollow cavity approximately 80 Å in diameter where iron is stored in the form of a Fe3+ mineral. (B) Each heme molecule (red) is buried at the interface of a subunit dimer (green and gray), with the heme propionates protruding into the interior cavity. Each molecule of Bfd (cyan) binds BfrB at the subunit dimer interface to facilitate electron flow from the [2Fe−2S] cluster (orange and yellow spheres) in Bfd to the Fe3+ mineral in the interior cavity of BfrB through a heme, thus promoting the mobilization of Fe2+.

4.2. Development of small molecule inhibitors of BfrB:Bfd interactions

The low permeability of the outer membrane of *P. aeruginosa*, as well as secondary adaptive resistance mechanisms such as increased efflux and enzymatic antibiotic modifications, enable it to be resistant to a wide range of antibiotics from β-lactams to fluoroquinolones.[38] Drug resistance is increasing,[4] and therefore new strategies must be developed to fight this bacterium. As described earlier, iron is an essential nutrient, but can be toxic if improperly regulated. This vulnerability could possibly be exploited through inhibition of the bacterial BfrB:Bfd interaction. Crystal structure of BfrB-Bfd complex showed 12 Bfd molecules that bind at the dimer interface above a heme molecule (Figure 4.1),[39] and that the K_d value of BfrB-Bfd binding was ~ 3 μM.[40] Since BfrB is unique to bacteria and archaea,[41] disruption of this protein-protein

interaction could present a novel, specific way to treat patients infected with *P. aeruginosa.*

To investigate this antibacterial approach, Dr. Huili Yao and Dr. Mario Rivera of the Louisiana State University Dept. of Chemistry came up with a new approach to perturb iron homeostasis in *P. aeruginosa* by designing small molecules that could potentially block the iron storage protein bacterioferritin B (BfrB) and its partner, the bacterioferritin associated ferredoxin (Bfd).[37] They conducted an iterative fragment-based drug discovery (FBDD) screen. In FBDD, a relatively small library of low molecular weight compounds that are generally polar and soluble is often screened by NMR against a protein target. When possible, this method provides an attractive alternative to more traditional high-throughput screening of large libraries of drug-like molecules. The fragments used in FBDD typically bind proteins with low affinity (mM) and are later combined with other fragments to generate leads for a drug discovery campaign.[42] Saturation transfer difference nuclear magnetic resonance spectroscopy (STD-NMR) was employed by the Rivera group to screen the fragment library that binds BfrB at the Bfd-binding site. STD-NMR is an attractive method for FDBB because it focuses on the signal of the ligand, so processing of additional NMR information of the receptor is unnecessary and very low concentrations of protein are required.[43] With the use of competitive displacement strategy, it was found that 18 fragments bind to BfrB, whereas 6 molecules bind at the Bfd-binding site. These fragments were then tested for binding to BfrB by two orthogonal assays, SPR and X-ray crystallography, and one fragment (**11**) (Figure 4.2) was selected to develop secondary hits for further studies of Bfrb-Bfd protein-protein interactions.

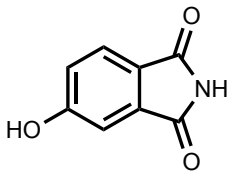

5-hydroxyisoindoline-1,3-dione (**11**)

Figure 4.2. Structure of fragment 1 (initial hit) that binds BfrB at the Bfd-binding site as identified by the Rivera group via a FBDD screen.

After the initial hit was identified, more than 100 second-generation compounds were designed to take advantage of additional interactions at the Bfd:BfrB binding interface. Docking to BfrB using Autodock vina[44] were performed on each of the derivatives, and those that showed promising docking scores were synthesized and investigated for binding and inhibition of iron release. Although all of the compounds for each of the initial hits were synthesized and tested in crystal soaking experiments by Rivera group, only 6 analogs from fragment **12** gave structures of analog-bound BfrB and these were selected for further studies (Figure 4.3).

This chapter describes a development of an assay using fluorescence polarization to quantify the binding affinities of small molecule inhibitors of the BfrB-Bfd protein-protein interaction.[37] I describe the spectral properties of the compounds tested, development of the fluorescence polarization assay and discuss potential future directions for this project. This FP assay was initially developed by Dr. Molly Lee, a previous graduate student in the Peterson lab.

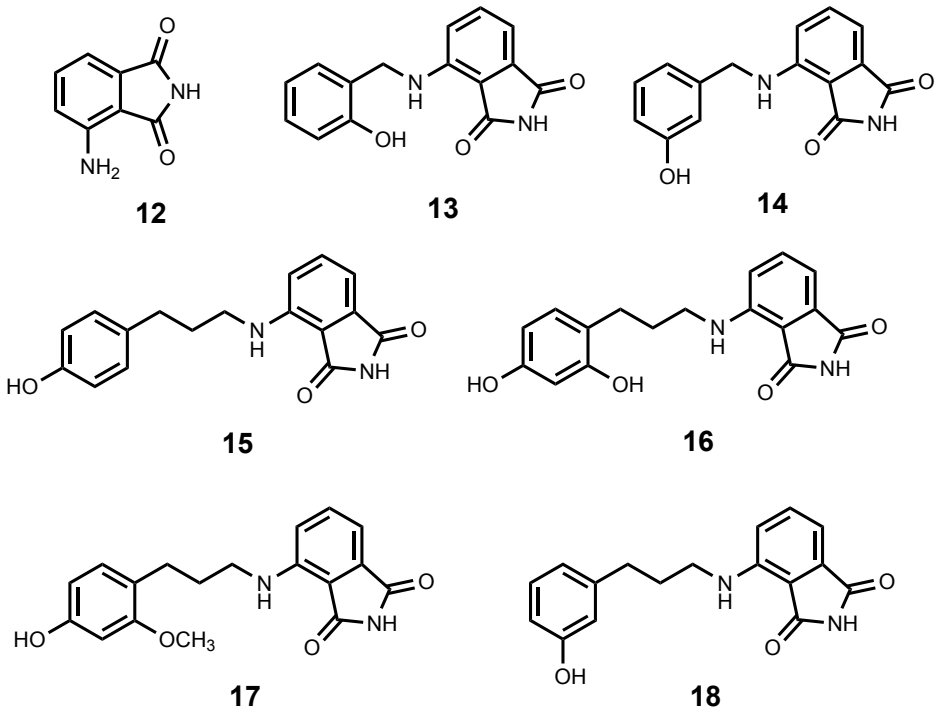

Figure 4.3. Structures of analogues of 4-aminoisoindoline fragment selected for binding affinity studies.

4.3. Development of a fluorescence polarization assay of inhibitors of BfrB:Bfd interactions

Spectroscopic studies revealed that the 12-heme molecules of the holo-BfrB protein fluoresce, and this intrinsic fluorescence was found to interfere with the signal from the fluorescent ligand. To overcome this complication, we used Apo-BfrB for fluorescence polarization assays. To confirm that studies using Apo-BfrB were valid, Dr. Huili Yao and Dr. Mario Rivera measured the binding affinity of Bfd to Apo-BfrB and holo-BfrB and found identical K_d values of 3 μM. Since the BfrB-Bfd interface is at the surface of the protein, the absence of heme, which is buried within the 24-mer protein, should not have a large effect on these binding interactions. Hence, Apo-BfrB is identical to that of

BfrB at the subunit level including the Bfd-binding sites and was used in the experiments because of its robustness and reproducibility.

Before starting the binding experiments with selected analogues and Apo-BfrB, photophysical properties of all the molecules were obtained. Although a high concentration of ligand was needed due to low brightness, initial experiments with compound **13** showed a 3-fold increase in fluorescence polarization when glycerol was added to buffer, indicating that as the mobility of the compound was restricted (due to the increase in viscosity of the solvent), the polarization of the compound was altered.[45,46] To investigate the affinity of analogs **12-18** binding to BfrB and to generate an equilibrium binding curve, Apo-BfrB was titrated into a fixed concentration of each fluorescent ligand for 1 h, followed by excitation at the respective excitation wavelength and analysis of fluorescence polarization at their emission wavelength. Curve fitting was used to calculate a direct binding K_d value (Figure 4.4).

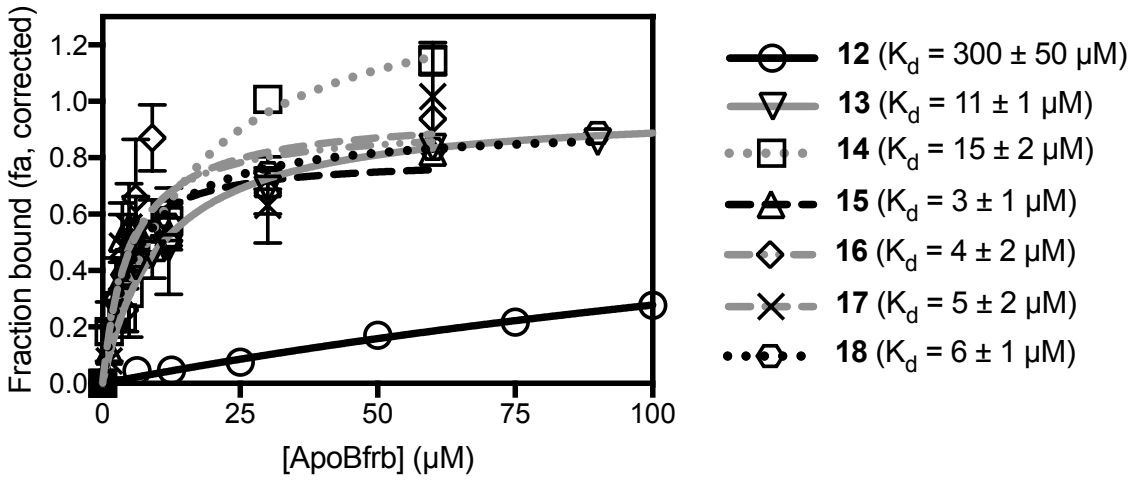

Figure 4.4. Quantification of the affinity (K_d) of Apo-BfrB for **12-18** by fluorescence polarization, corrected to account for changes in fluorescence intensity upon binding. Values were obtained in KPi buffer (100 mM) containing TCEP (1 mM, pH 7.6, 0.5% DMSO). [**12**] = 50 μM. [**14**, **15**] = 2 μM. [**13**, **16**, **17**, **18**] = 5 μM. Dissociation constants (K_d) were calculated using a one-site binding model in GraphPad Prism.

4.4. Conclusions and future directions

Investigations by the Rivera group have previously shown that interference with iron storage process from bacterioferritin perturbs bacterial iron homeostasis.[22] Based on these results, FBDD screen using STD-NMR was employed to design and synthesize small molecule inhibitors of BfrB-Bfd protein-protein interaction. To test the binding affinity of these compounds, we collaborated with the Rivera laboratory to develop a new fluorescence polarization assay. These binding studies along with other observations offer a promising target for antimicrobial inhibition of *Pseudomonas aeruginosa* and could help to overcome challenges arising from multidrug resistance observed with this superbug. Better inhibitors, as well as assays to screen these inhibitors more readily, need to be developed for this goal to be realized.

4.5. Experimental

4.5.1. General

Apo-BfrB was expressed and purified as described previously.[29,35] Absorbance spectra and measurements of molar extinction coefficients (ε) were generated using semimicro (1.4 mL) UV quartz cuvettes (Sigma-Aldrich, Z27667-7) on an Agilent 8452A diode array spectrometer. All optical spectroscopy and protein binding assays were conducted in 100 mM KP_i (pH 7.6) with TCEP (1 mM), unless otherwise noted. All fluorescence emission spectra were acquired using a SUPRASIL ultra-micro quartz cuvette (PerkinElmer, B0631079) on a Perkin-Elmer LS55 Fluorescence Spectrometer (10 nm excitation slit width).

4.5.2. Determination of K_d values by fluorescence polarization (FP)

To calculate dissociation constants (K_d), fluorescence polarization (FP) values were measured in triplicate. Different concentrations of Apo-BfrB were incubated with fixed concentrations of ligands (100 mM KPi buffer containing 1 mM TCEP, pH 7.6) were incubated with increasing concentrations of Apo-BfrB (based on a protein dimer) at room temperature (22 °C) with shaking for 1 h, followed by excitation of the small molecules near the absorbance λ_{max} (**12**, 380 nm; **13**, **14**, 400 nm; **15**, **17**, **18**, 410 nm; **16**, 415 nm) with analysis of fluorescence polarization near the emission λ_{max} (**12**, 565 nm; **13**, **17**, 540 nm; **14**, 525 nm; **15**, **16**, **18**, 550 nm). The ligand was maintained in buffer for a maximum of 5 min prior to incubation with the protein to minimize any potential for degradation. Fixed ligand concentrations were chosen to be near or below predicted K_d values to assure equilibrium binding measurements. Measurements of fluorescence intensity (I) and fluorescence polarization (P) at the respective emission and absorption wavelengths were recorded for each sample to allow correction for fluorescence enhancement or quenching during binding.

The change in polarization for each sample was calculated by subtracting the average (n=3) polarization of the free ligand (P_f). This change was plotted against the concentration of Apo-BfrB, and the maximum polarization of the fully bound complex was estimated (B_{max}) based on a one-site specific binding model (GraphPad Prism 6.0). This polarization of the complex (P_b) was used in the following equation to calculate the apparent fraction bound (F_a):

$$F_a = \frac{P - P_f}{P_b - P_f}$$

Background-subtracted fluorescence (*I*) signals were calculated as follows:

$$I = I_{380} - I_{Bfrb}$$

where I_{BfrB} is the background fluorescence intensity of the protein alone at each concentration measured, excited under the same conditions as the protein with the small molecule. In order to correct for fluorescence enhancement or quenching, a fluorescence enhancement factor (*Q*) was calculated using the following equation, where *I* and I_0 are the fluorescence intensity (λ_{ex}= 380 nm, λ_{em}= 565 nm) of the sample and free ligand, respectively:

$$Q = \frac{I - I_0}{I_0}$$

To incorporate fluorescence enhancement/quenching into the measurements, the corrected fraction bound (f_a) was calculated using the following equation:

$$f_a = \frac{F_a}{1 + Q(1 - F_a)}$$

To calculate the dissociation constant (K_d), the corrected fraction bound was plotted against the concentration of Apo-BfrB (dimer concentration), and a one site-specific binding equation of GraphPad Prism 6.0 was used for curve fitting.

4.6. References

1. Venter, H.; Blaskovich, M. A.; Butler, M. S.; Cooper, M. A., Polishing the tarnished silver bullet: the quest for new antibiotics. *Essays Biochem.* **2017***, 61*, 103-114.
2. Laxminarayan, R.; Duse, A.; Wattal, C.; Zaidi, A. K.; Wertheim, H. F.; Sumpradit, N.; Vlieghe, E.; Hara, G. L.; Gould, I. M.; Goossens, H., Antibiotic resistance—the need for global solutions. *Lancet Infect. Dis.* **2013***, 13*, 1057-1098.
3. Tacconelli, E.; Carrara, E.; Savoldi, A.; Harbarth, S.; Mendelson, M.; Monnet, D. L.; Pulcini, C.; Kahlmeter, G.; Kluytmans, J.; Carmeli, Y., Discovery, research, and development of new antibiotics: the WHO priority list of antibiotic-resistant bacteria and tuberculosis. *Lancet Infect. Dis.* **2018***, 18*, 318-327.
4. Aloush, V.; Navon-Venezia, S.; Seigman-Igra, Y.; Cabili, S.; Carmeli, Y., Multidrug-Resistant Pseudomonas aeruginosa: Risk Factors and Clinical Impact. *Antimicrob. Agents Chemother.* **2006***, 50*, 43-48.
5. Boucher, H. W.; Talbot, G. H.; Bradley, J. S.; Edwards, J. E.; Gilbert, D.; Rice, L. B.; Scheld, M.; Spellberg, B.; Bartlett, J., Bad bugs, no drugs: no ESKAPE! An update from the Infectious Diseases Society of America. *Clin. Infect. Dis.* **2009***, 48*, 1-12.
6. Konstan, M. W.; Morgan, W. J.; Butler, S. M.; Pasta, D. J.; Craib, M. L.; Silva, S. J.; Stokes, D. C.; Wohl, M. E. B.; Wagener, J. S.; Regelmann, W. E., Risk factors for rate of decline in forced expiratory volume in one second in children and adolescents with cystic fibrosis. *J. Pediatr.* **2007***, 151*, 134-139. e131.
7. Gellatly, S. L.; Hancock, R. E. W., Pseudomonas aeruginosa: new insights into pathogenesis and host defenses. *Pathog. Dis.* **2013***, 67*, 159-173.

8. Lyczak, J. B.; Cannon, C. L.; Pier, G. B., Establishment of Pseudomonas aeruginosa infection: lessons from a versatile opportunist. *Microbes Infect.* **2000***, 2*, 1051-1060.

9. Høiby, N., Recent advances in the treatment of Pseudomonas aeruginosainfections in cystic fibrosis. *BMC Med.* **2011***, 9*, 32.

10. West, S. H.; Zeng, L.; Lee, B.; et al., Respiratory infections with pseudomonas aeruginosa in children with cystic fibrosis: Early detection by serology and assessment of risk factors. *JAMA.* **2002***, 287*, 2958-2967.

11. Smith, D. J.; Lamont, I. L.; Anderson, G. J.; Reid, D. W., Targeting iron uptake to control Pseudomonas aeruginosa infections in cystic fibrosis. *Eur. Resp. J.* **2013***, 42*, 1723-1736.

12. Vasil, M. L.; Ochsner, U. A., The response of Pseudomonas aeruginosa to iron: genetics, biochemistry and virulence. *Mol. Microbiol.* **1999***, 34*, 399-413.

13. Kaneko, Y.; Thoendel, M.; Olakanmi, O.; Britigan, B. E.; Singh, P. K., The transition metal gallium disrupts Pseudomonas aeruginosa iron metabolism and has antimicrobial and antibiofilm activity. *J. Clin. Invest.* **2007***, 117*, 877-888.

14. Ballouche, M.; Cornelis, P.; Baysse, C., Iron metabolism: a promising target for antibacterial strategies. *Recent patents on anti-infective drug discovery.* **2009***, 4*, 190-205.

15. Foley, T. L.; Simeonov, A., Targeting iron assimilation to develop new antibacterials. *Expert Opin. Drug Dis.* **2012***, 7*, 831-847.

16. Heinzl, G. A.; Huang, W.; Yu, W.; Giardina, B. J.; Zhou, Y.; MacKerell Jr, A. D.; Wilks, A.; Xue, F., Iminoguanidines as allosteric inhibitors of the iron-regulated heme

oxygenase (HemO) of pseudomonas aeruginosa. *J. Med. Chem.* **2016***, 59*, 6929-6942.

17. Lueangsakulthai, J.; Jangpromma, N.; Temsiripong, T.; McKendrick, J. E.; Khunkitti, W.; Maddocks, S.; Klaynongsruang, S., A novel antibacterial peptide derived from Crocodylus siamensis haemoglobin hydrolysate induces membrane permeabilization causing iron dysregulation, oxidative stress and bacterial death. *J. Appl. Microbiol.* **2017***, 123*, 819-831.
18. Theil, E. C.; Goss, D. J., Living with Iron (and Oxygen): Questions and Answers about Iron Homeostasis. *Chem. Rev.* **2009***, 109*, 4568-4579.
19. Meneghini, R., Iron Homeostasis, Oxidative Stress, and DNA Damage. *Free Radic. Biol. Med.* **1997***, 23*, 783-792.
20. Haber, F.; Weiss, J., The Catalytic Decomposition of Hydrogen Peroxide by Iron Salts. *Proc. Roy. Soc. Lond. Math. Phys. Sci.* **1934***, 147*, 332-351.
21. Andrews, S. C. Iron Storage in Bacteria. In R. K. Poole (Ed.), *Adv. Microbiol. Phys.* **1998**, (Vol. Volume 40, pp. 281-351): Academic Press.
22. Eshelman, K.; Yao, H.; Hewage, A. N. P.; Deay, J. J.; Chandler, J. R.; Rivera, M., Inhibiting the BfrB: Bfd interaction in Pseudomonas aeruginosa causes irreversible iron accumulation in bacterioferritin and iron deficiency in the bacterial cytosol. *Metallomics.* **2017***, 9*, 646-659.
23. Keyer, K.; Imlay, J. A., Superoxide accelerates DNA damage by elevating free-iron levels. *Proc. Natl. Acad. Sci. U S A.* **1996***, 93*, 13635-13640.
24. Rivera, M. Bacterioferritin: Structure Function and Protein–Protein Interactions. In *Handbook of Porphyrin Science (Volume 30) With Applications to Chemistry,*

Physics, Materials Science, Engineering, Biology and Medicine—Volume 30: Heme Proteins—Part II **2014**, (pp. 135-178): World Scientific.

25. Andrews, S.; Norton, I.; Salunkhe, A. S.; Goodluck, H.; Aly, W. S.; Mourad-Agha, H.; Cornelis, P. Control of iron metabolism in bacteria. In *Metallomics and the Cell* **2013**, (pp. 203-239): Springer.
26. Rivera, M., Bacterioferritin: structure, dynamics, and protein–protein interactions at play in iron storage and mobilization. *Acc. Chem. Res.* **2017***, 50*, 331-340.
27. Andrews, S. C.; Robinson, A. K.; Rodríguez-Quiñones, F., Bacterial iron homeostasis. *FEMS Microbiol. Rev.* **2003***, 27*, 215-237.
28. Lewin, A.; Moore, G. R.; Le Brun, N. E., Formation of protein-coated iron minerals. *Dalton Trans.* **2005**, 3597-3610.
29. Weeratunga, S. K.; Lovell, S.; Yao, H.; Battaile, K. P.; Fischer, C. J.; Gee, C. E.; Rivera, M., Structural Studies of Bacterioferritin B from Pseudomonas aeruginosa Suggest a Gating Mechanism for Iron Uptake via the Ferroxidase Center. *Biochemistry.* **2010***, 49*, 1160-1175.
30. Macedo, S.; Romao, C. V.; Mitchell, E.; Matias, P. M.; Liu, M. Y.; Xavier, A. V.; LeGall, J.; Teixeira, M.; Lindley, P.; Carrondo, M. A., The nature of the di-iron site in the bacterioferritin from Desulfovibrio desulfuricans. *Nat. Struct. Mol. Biol.* **2003***, 10*, 285-290.
31. Rui, H.; Rivera, M.; Im, W., Protein Dynamics and Ion Traffic in Bacterioferritin. *Biochemistry.* **2012***, 51*, 9900-9910.
32. Wang, A.; Zeng, Y.; Han, H.; Weeratunga, S.; Morgan, B. N.; Moënne-Loccoz, P.; Schönbrunn, E.; Rivera, M., Biochemical and Structural Characterization of

Pseudomonas aeruginosa Bfd and FPR: Ferredoxin NADP+ Reductase and Not Ferredoxin Is the Redox Partner of Heme Oxygenase under Iron-Starvation Conditions. *Biochemistry.* **2007***, 46*, 12198-12211.

33. Ruvinsky, A. M.; Vakser, I. A.; Rivera, M., Local packing modulates diversity of iron pathways and cooperative behavior in eukaryotic and prokaryotic ferritins. *J. Chem. Phys.* **2014***, 140*, 03B617_611.
34. Ma, J.-F.; Ochsner, U. A.; Klotz, M. G.; Nanayakkara, V. K.; Howell, M. L.; Johnson, Z.; Posey, J. E.; Vasil, M. L.; Monaco, J. J.; Hassett, D. J., Bacterioferritin A modulates catalase A (KatA) activity and resistance to hydrogen peroxide in Pseudomonas aeruginosa. *J. Bacteriol.* **1999***, 181*, 3730-3742.
35. Weeratunga, S. K.; Gee, C. E.; Lovell, S.; Zeng, Y.; Woodin, C. L.; Rivera, M., Binding of Pseudomonas aeruginosa Apobacterioferritin-Associated Ferredoxin to Bacterioferritin B Promotes Heme Mediation of Electron Delivery and Mobilization of Core Mineral Iron. *Biochemistry.* **2009***, 48*, 7420-7431.
36. Yao, H.; Wang, Y.; Lovell, S.; Kumar, R.; Ruvinsky, A. M.; Battaile, K. P.; Vakser, I. A.; Rivera, M., The Structure of the BfrB–Bfd Complex Reveals Protein–Protein Interactions Enabling Iron Release from Bacterioferritin. *J. Am. Chem. Soc.* **2012***, 134*, 13470-13481.
37. Hewage, A. N. P.; Yao, H.; Nammalwar, B.; Gnanasekaran, K. K.; Lovell, S.; Bunce, R. A.; Eshelman, K.; Phaniraj, S. M.; Lee, M. M.; Peterson, B. R., Small Molecule Inhibitors of the BfrB–Bfd Interaction Decrease Pseudomonas aeruginosa Fitness and Potentiate Fluoroquinolone Activity. *J. Am. Chem. Soc.* **2019***, 141*, 8171.

38. Breidenstein, E. B. M.; de la Fuente-Núñez, C.; Hancock, R. E. W., Pseudomonas aeruginosa: all roads lead to resistance. *Trends Microbiol.* **2011***, 19*, 419-426.

39. Yao, H.; Wang, Y.; Lovell, S.; Kumar, R.; Ruvinsky, A. M.; Battaile, K. P.; Vakser, I. A.; Rivera, M., The structure of the BfrB–Bfd complex reveals protein–protein interactions enabling iron release from bacterioferritin. *J. Am. Chem. Soc.* **2012***, 134*, 13470-13481.

40. Wang, Y.; Yao, H.; Cheng, Y.; Lovell, S.; Battaile, K. P.; Midaugh, C. R.; Rivera, M., Characterization of the bacterioferritin/bacterioferritin associated ferredoxin protein–protein interaction in solution and determination of binding energy hot spots. *Biochemistry.* **2015***, 54*, 6162-6175.

41. Andrews, S. C., The Ferritin-like superfamily: Evolution of the biological iron storeman from a rubrerythrin-like ancestor. *Biochim. Biophys. Acta Gen. Subjects.* **2010***, 1800*, 691-705.

42. Joseph-McCarthy, D.; Campbell, A. J.; Kern, G.; Moustakas, D., Fragment-Based Lead Discovery and Design. *J. Chem. Inf. Model.* **2014***, 54*, 693-704.

43. Viegas, A.; Manso, J.; Nobrega, F. L.; Cabrita, E. J., Saturation-Transfer Difference (STD) NMR: A Simple and Fast Method for Ligand Screening and Characterization of Protein Binding. *J. Chem. Ed.* **2011***, 88*, 990-994.

44. Trott, O.; Olson, A. J., AutoDock Vina: improving the speed and accuracy of docking with a new scoring function, efficient optimization and multithreading. *J. Comp. Chem.* **2010***, 31*, 455-461.

45. Jameson, D. M.; Ross, J. A., Fluorescence Polarization/Anisotropy in Diagnostics and Imaging. *Chem. Rev.* **2010***, 110*, 2685-2708.

46. James, N. G.; Jameson, D. M., Steady-state fluorescence polarization/anisotrophy for the study of protein interactions. *Methods in Molecular Biology*, **2014**, vol. 1076, Humana Press, Totowa, NJ.

APPENDIX A

Mass spectra of membrane scaffold proteins

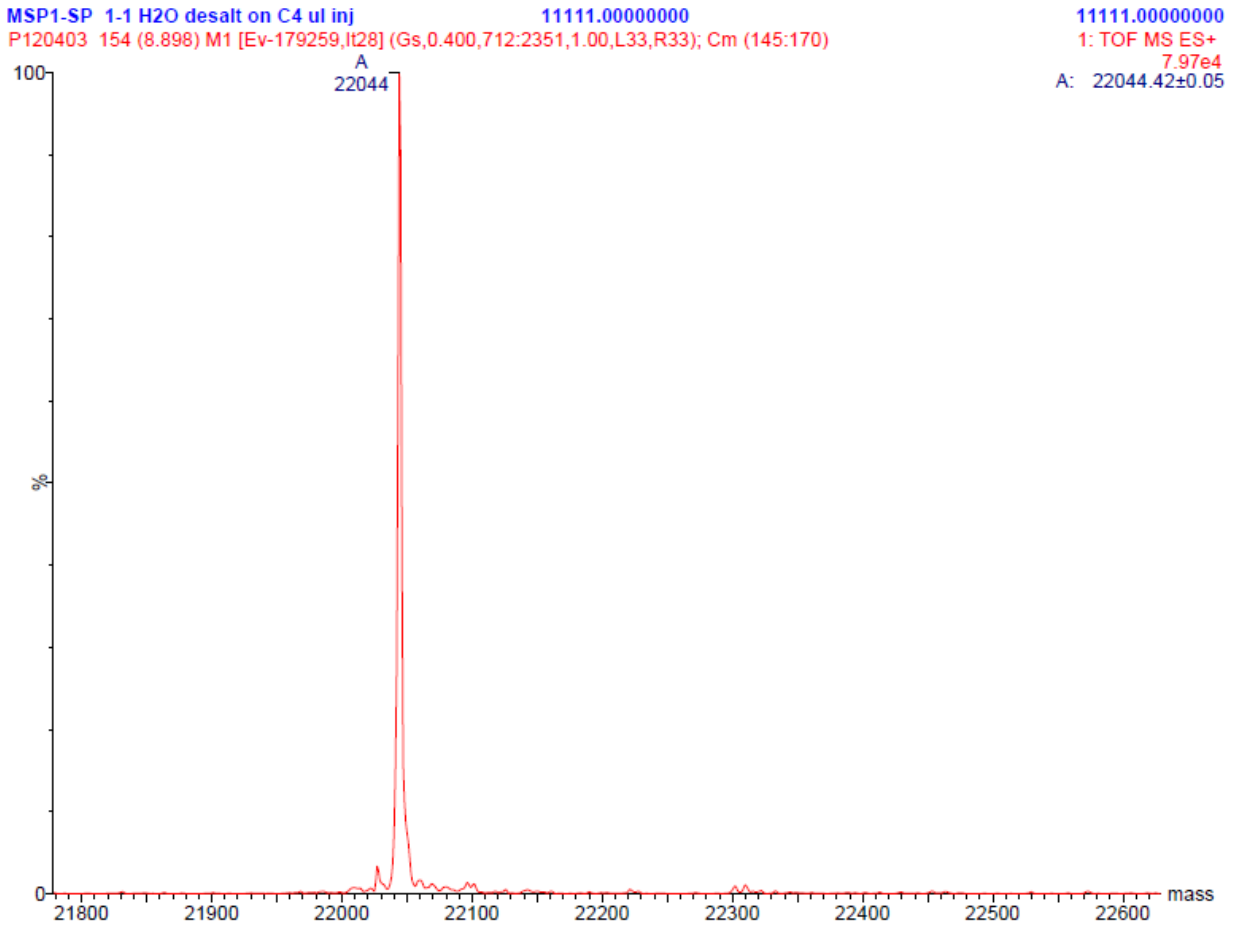

Figure 5.1. Mass spectrum of the traditional membrane scaffold protein MSP1D1. MSP1D1 was found to have a mass of 22044 Da. Expected mass: 22044 Da.

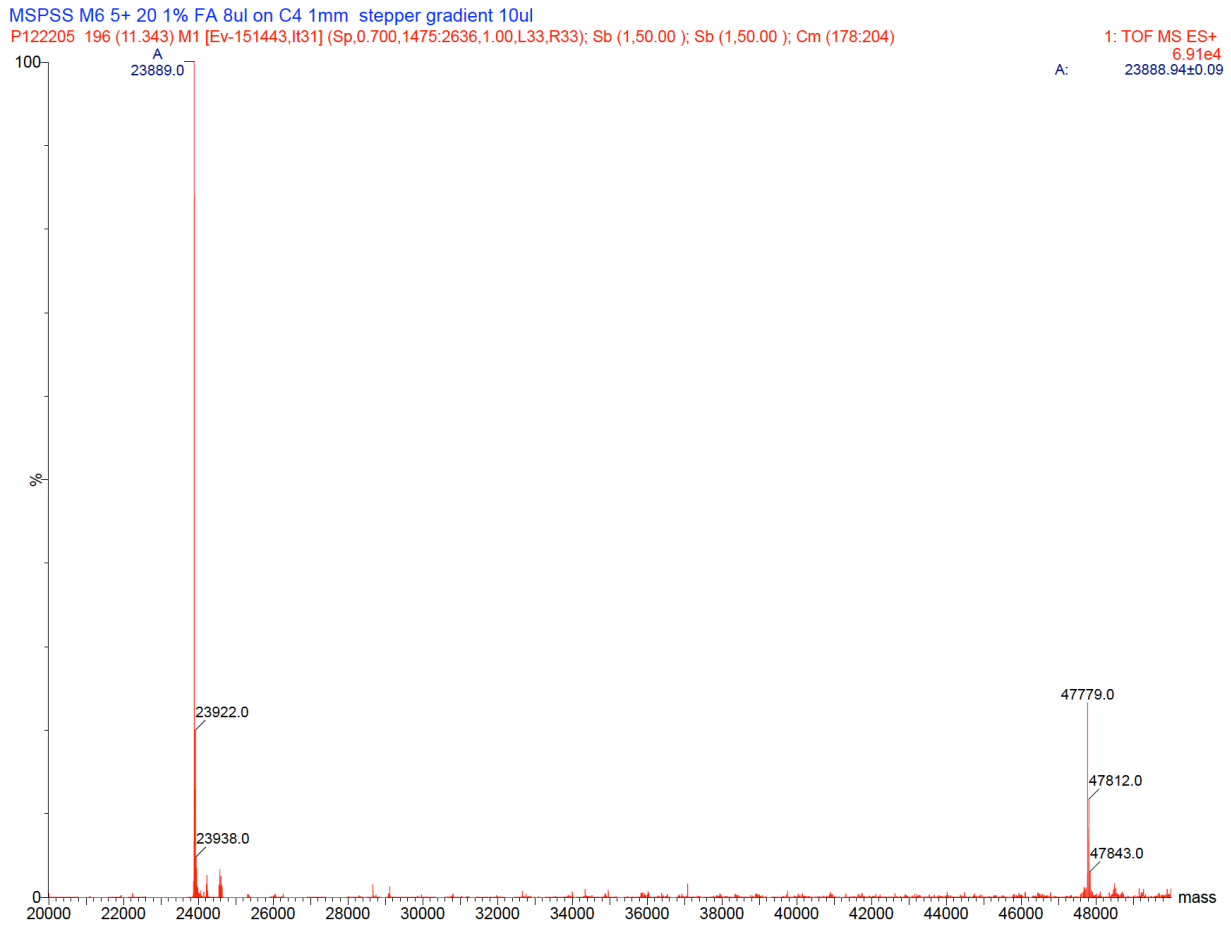

Figure 5.2. Mass spectrum of disulfide linked MSPSS_M6. MSPSS_M6 was found to have a mass of 23889 Da. Expected mass: 23891 Da. A dimer of mass 47779 can also be observed.

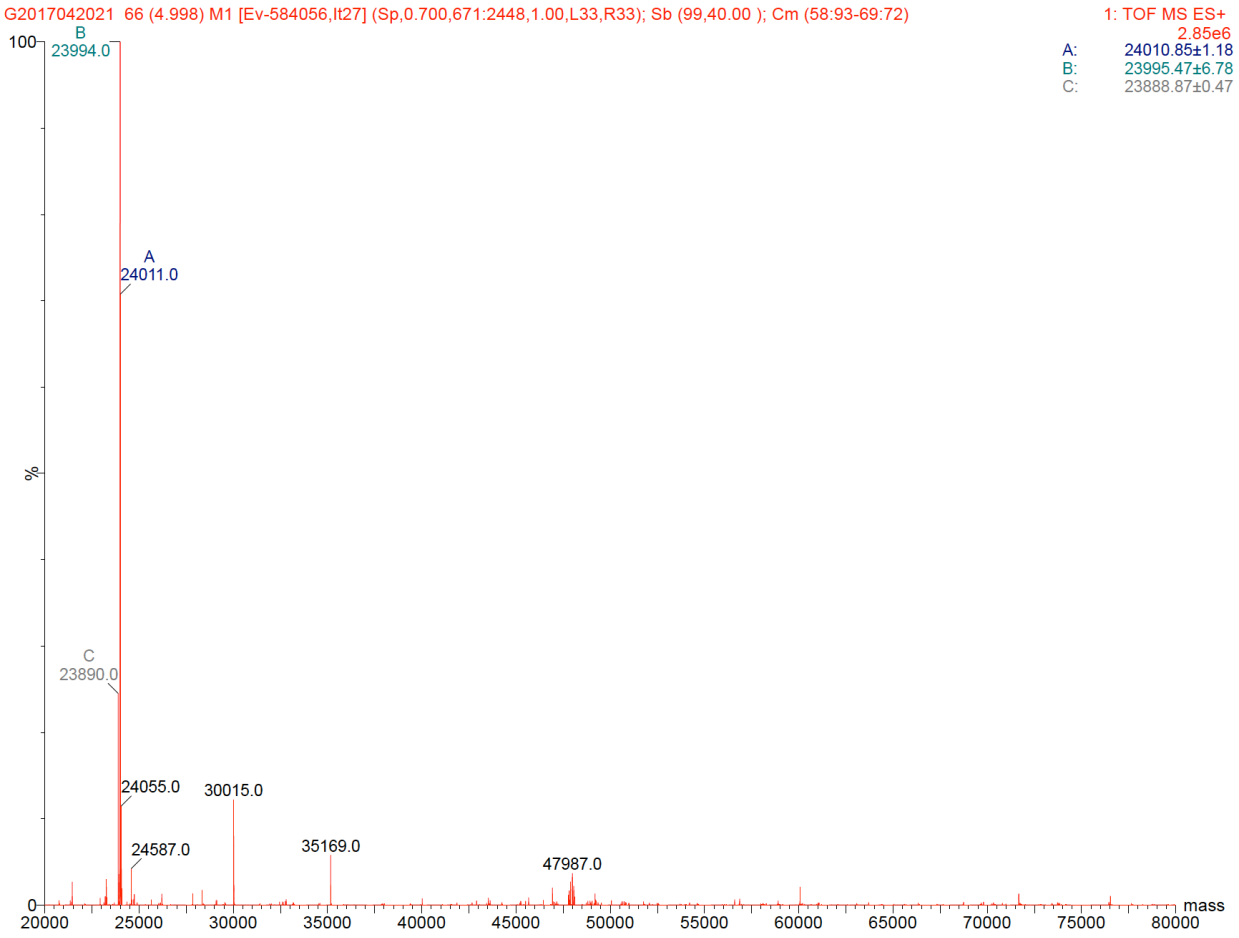

Figure 5.3. Mass spectrum of the covalently cross-linked mxy_MSPSS_M6. mxy_MSPSS_M6 was found to have a mass of 23994 Da. Expected mass after the addition of meta-xylene to MSPSS_M6: 23993 Da. Higher oligomers are absent in this case.

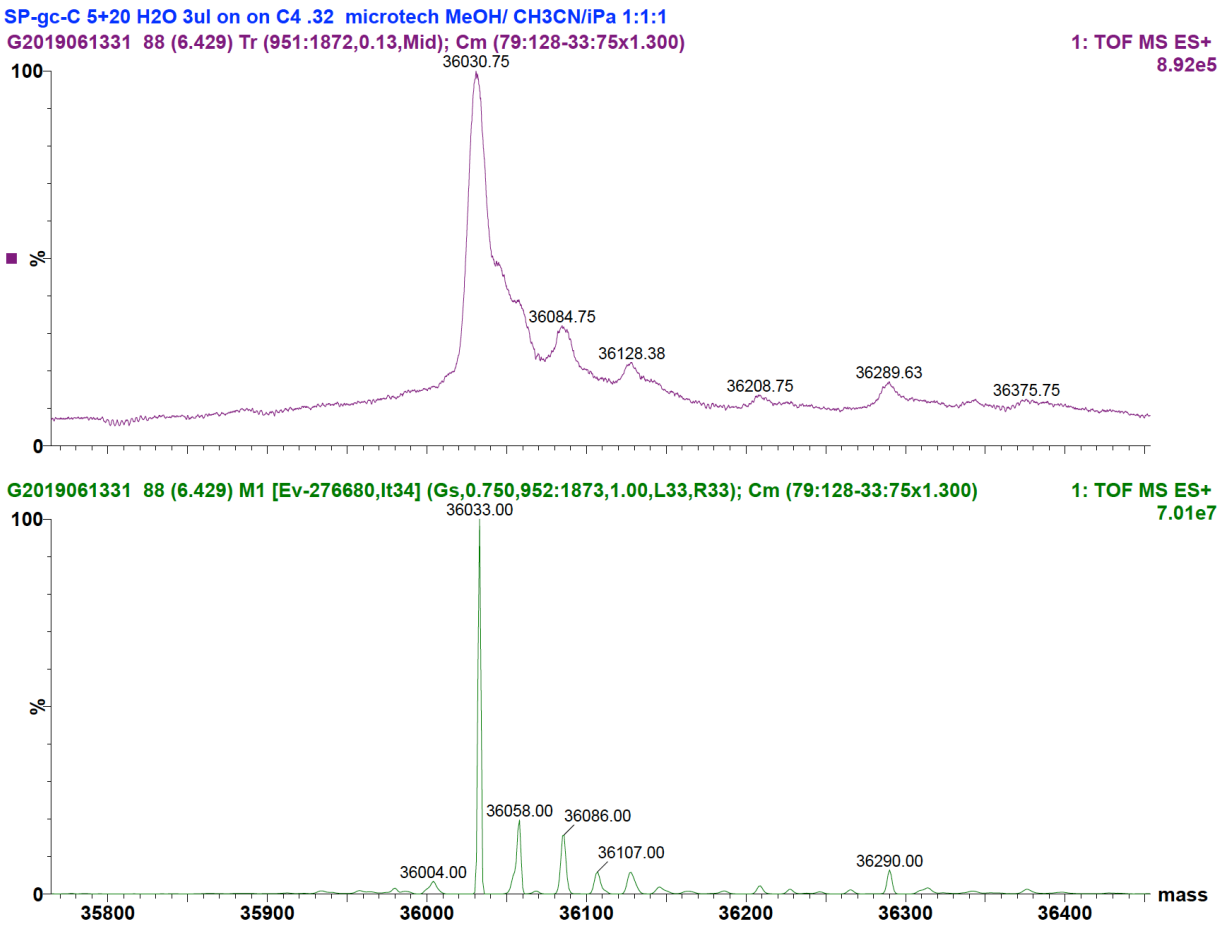

Figure 5.4. Mass spectrum of SpyMSP protein. SpyMSP was found to have a mass of 36031 Da. Expected mass: 36031 Da, after loss of a water molecule.

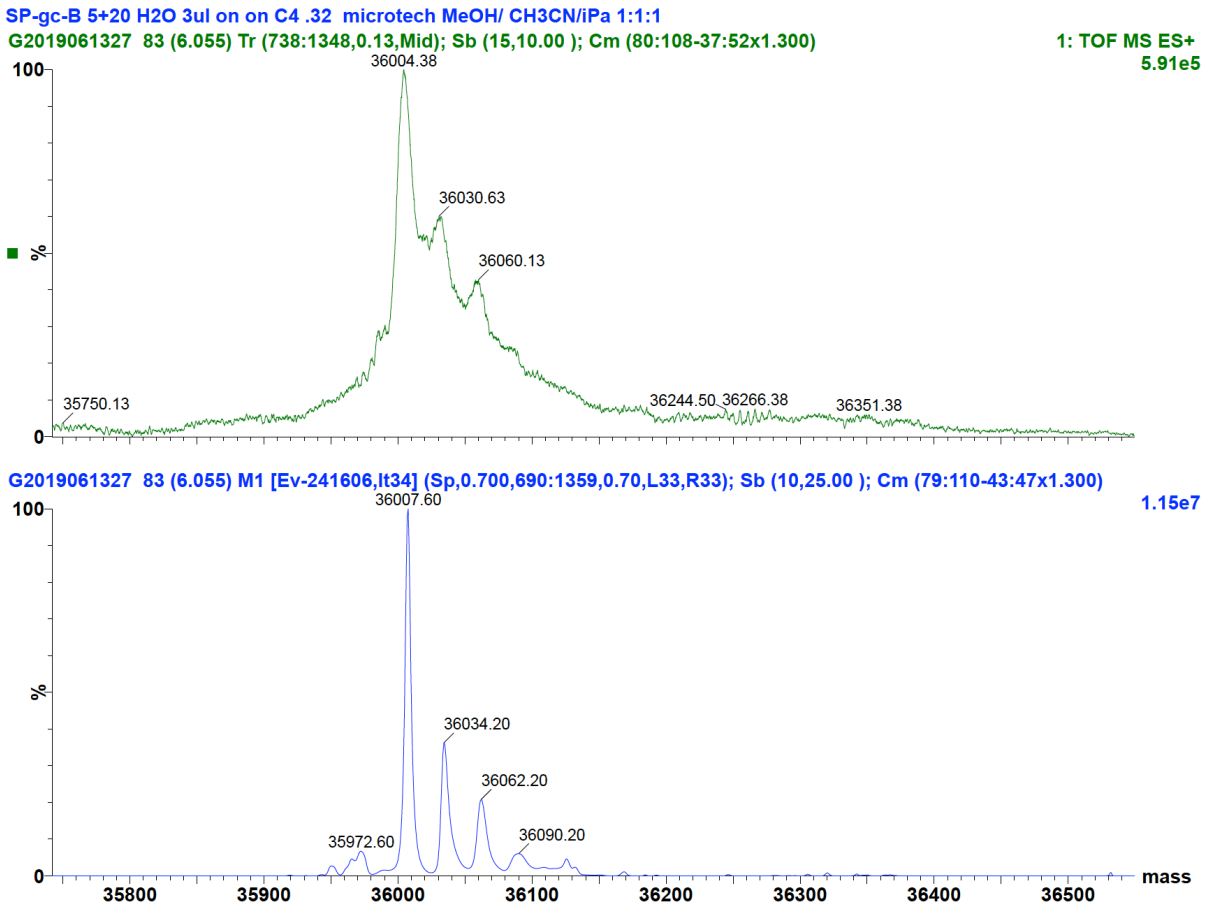

Figure 5.5. Mass spectrum of SpyMSP D340A. SpyMSP D340A was found to have a mass of 36004 Da. Expected mass: 36005 Da.

APPENDIX B

Nmr spectra

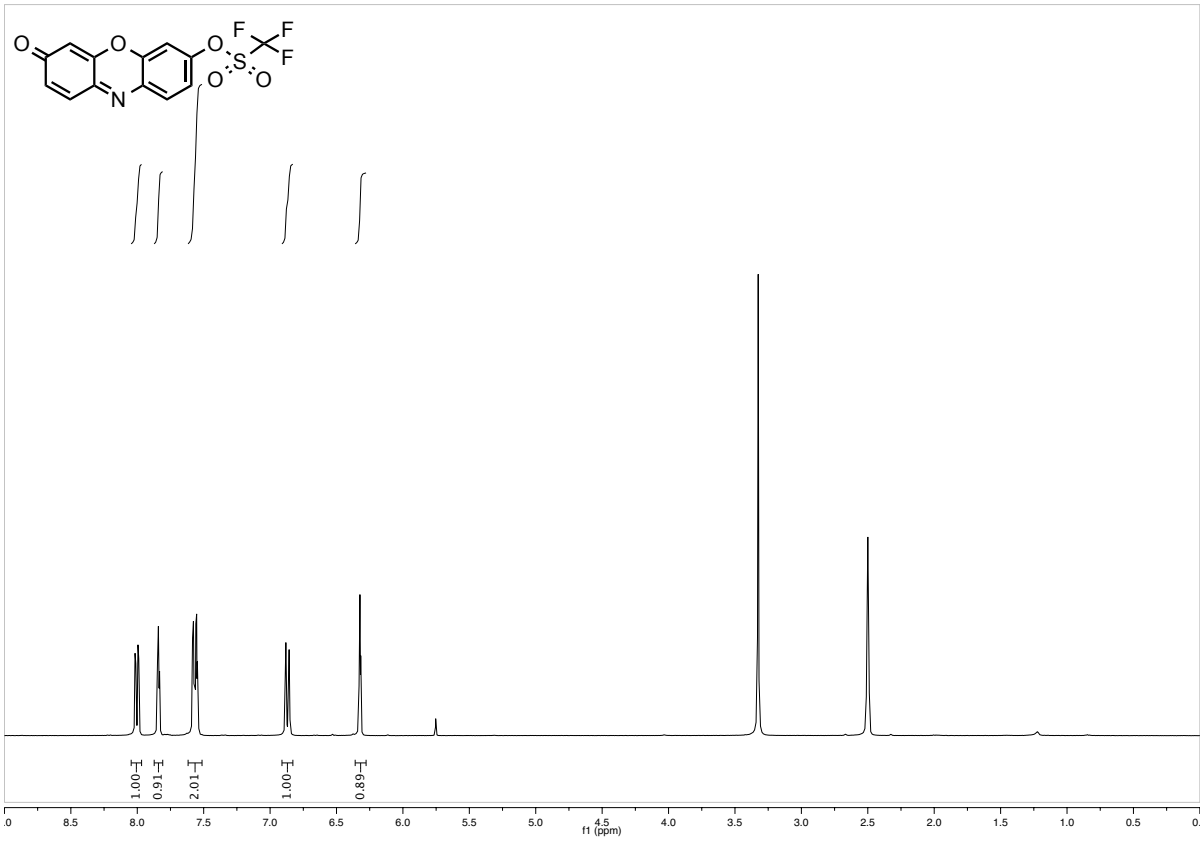

Figure 5.6. ^{1}H NMR (400 MHz, DMSO-d_6) spectrum of resorufin triflate (**9**).

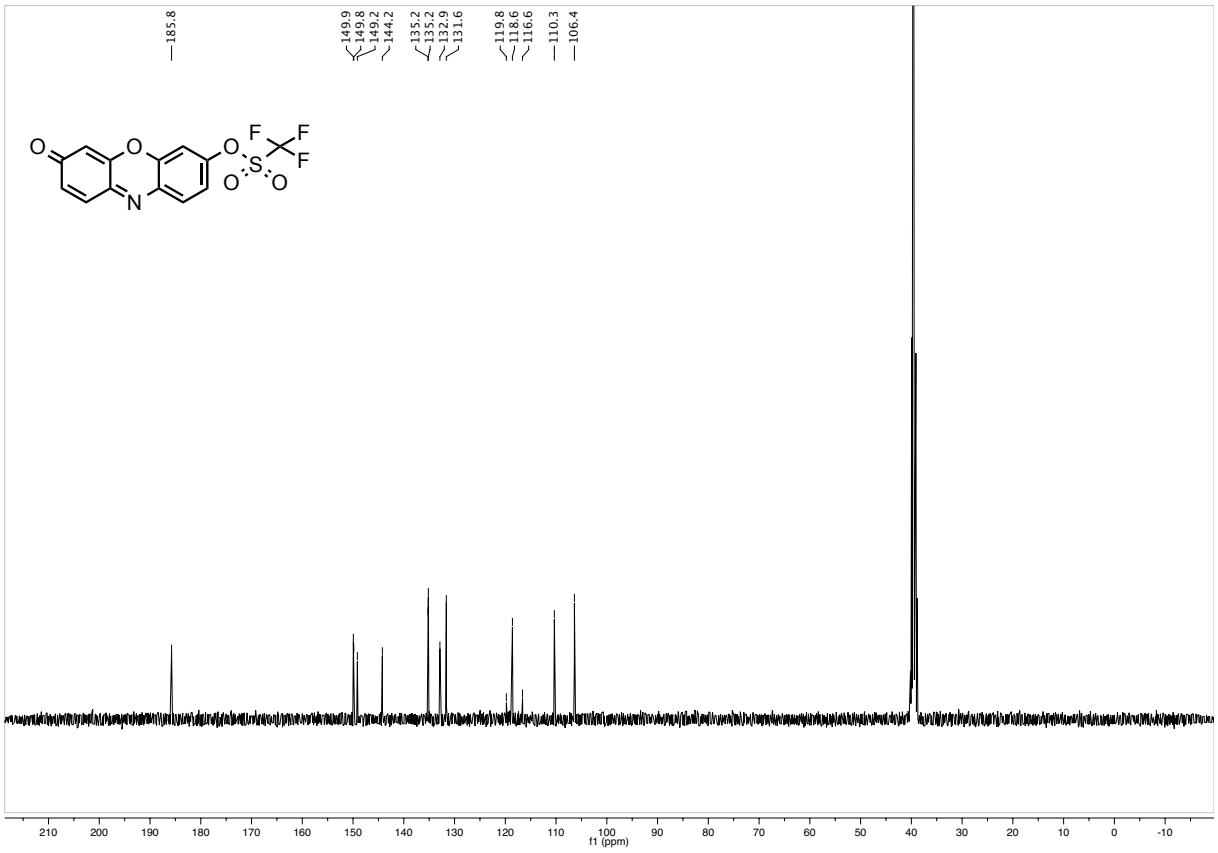

Figure 5.7. ^{13}C NMR (101 MHz, DMSO-d_6) spectrum of resorufin triflate (**9**).

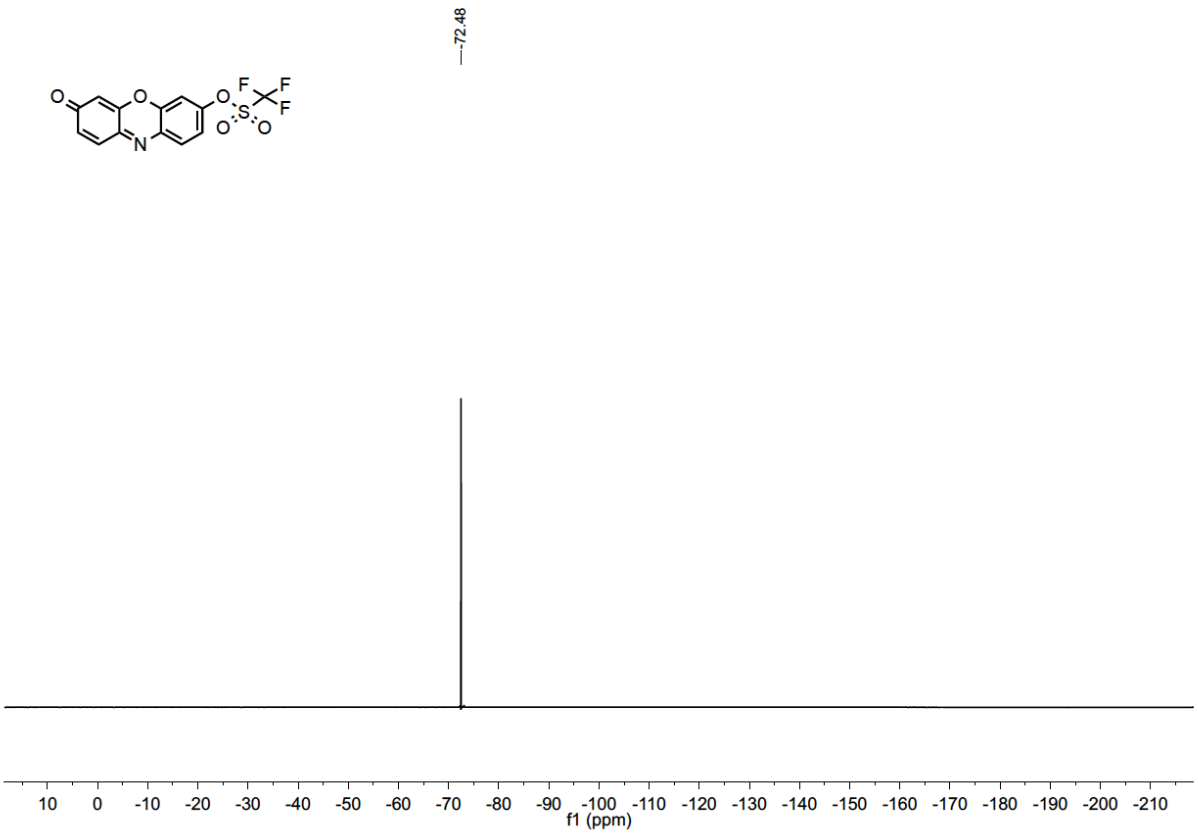

Figure 5.8. ^{19}F NMR (376 MHz, DMSO-d_6) spectrum of resorufin triflate (**9**).

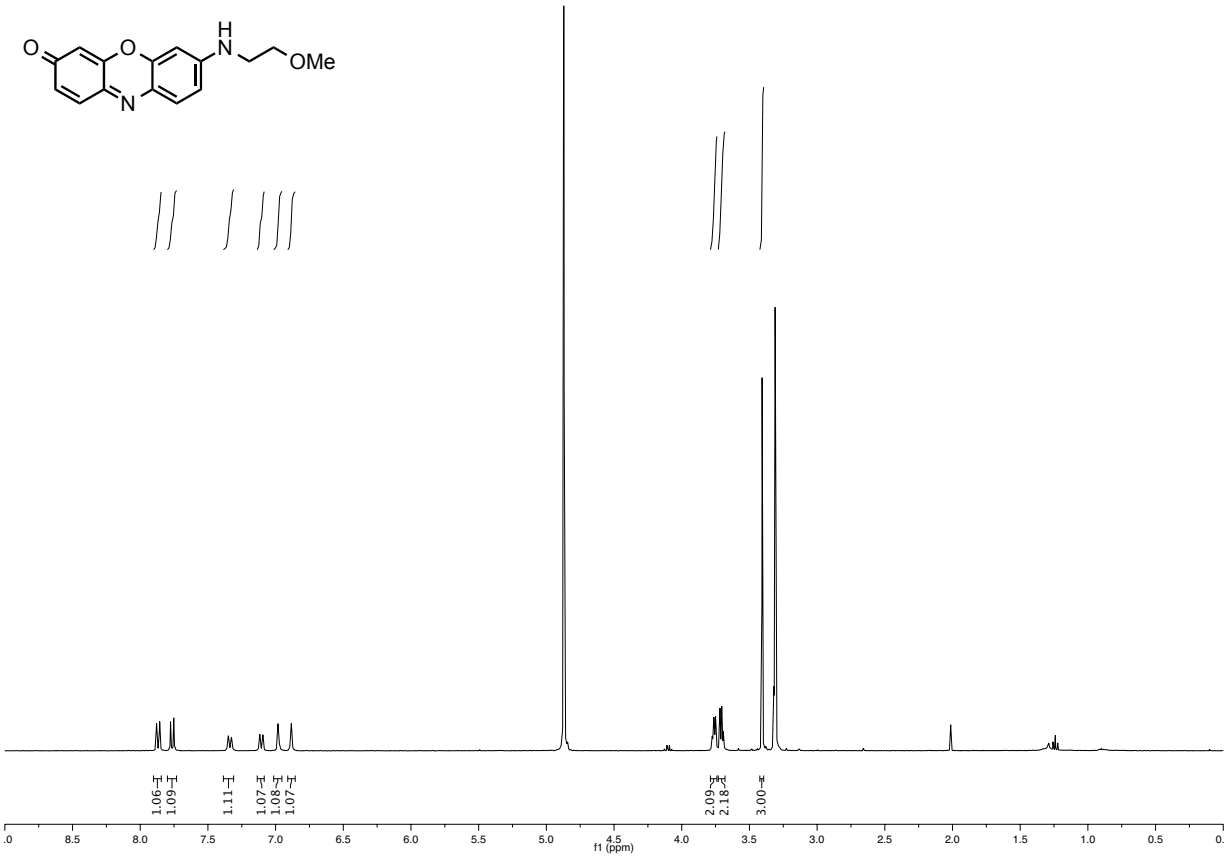

Figure 5.9. ^{1}H NMR (400 MHz, CD_3OD) spectrum of **10**.

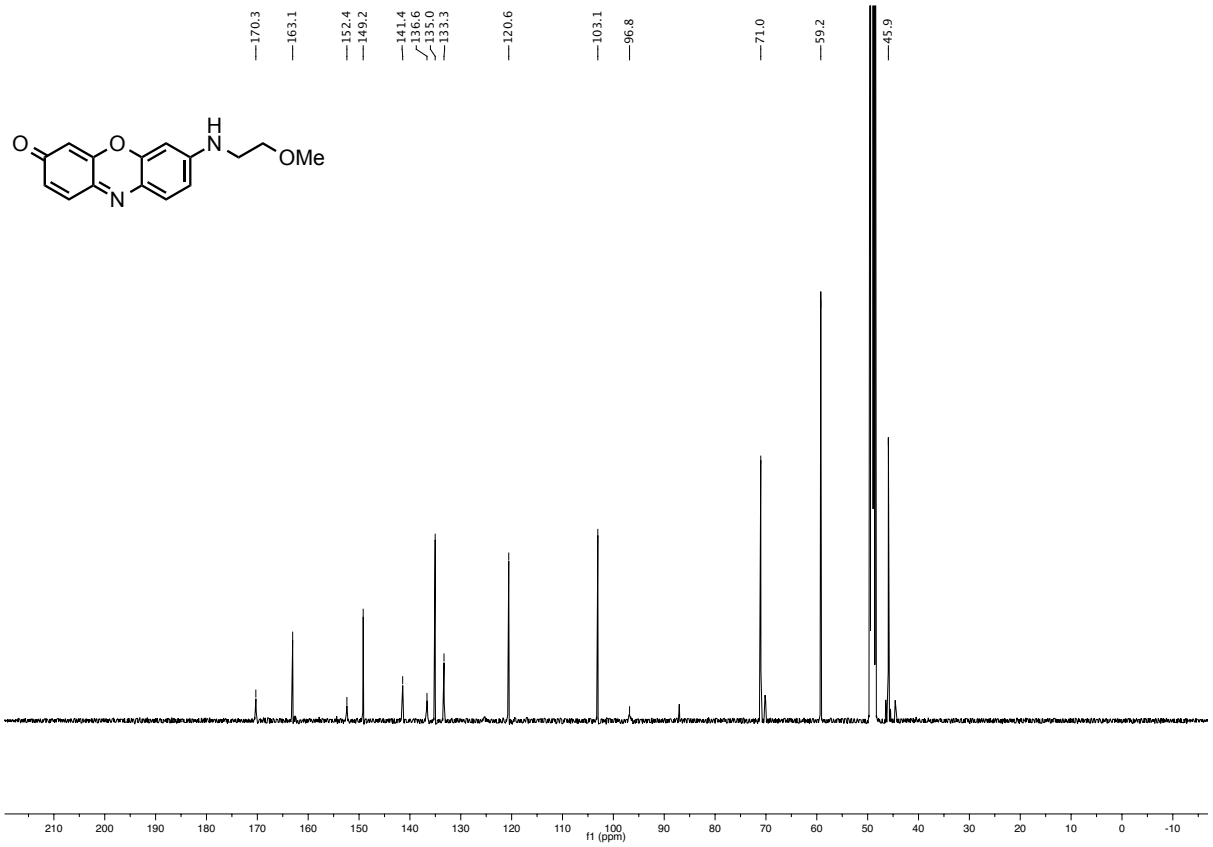

Figure 5.10. ^{13}C NMR (126 MHz, CD_3OD) spectrum of **10**.

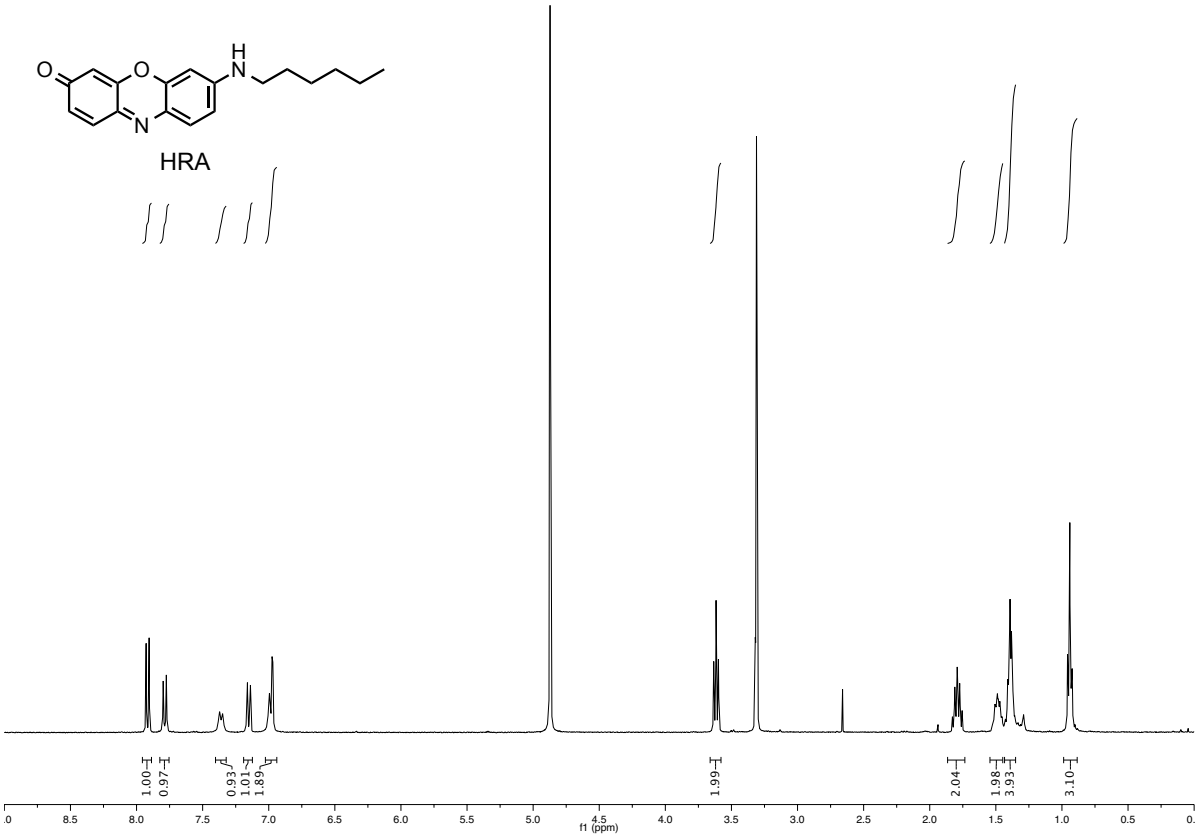

Figure 5.11. ^{1}H NMR (400 MHz, CD_3OD) spectrum of HRA.

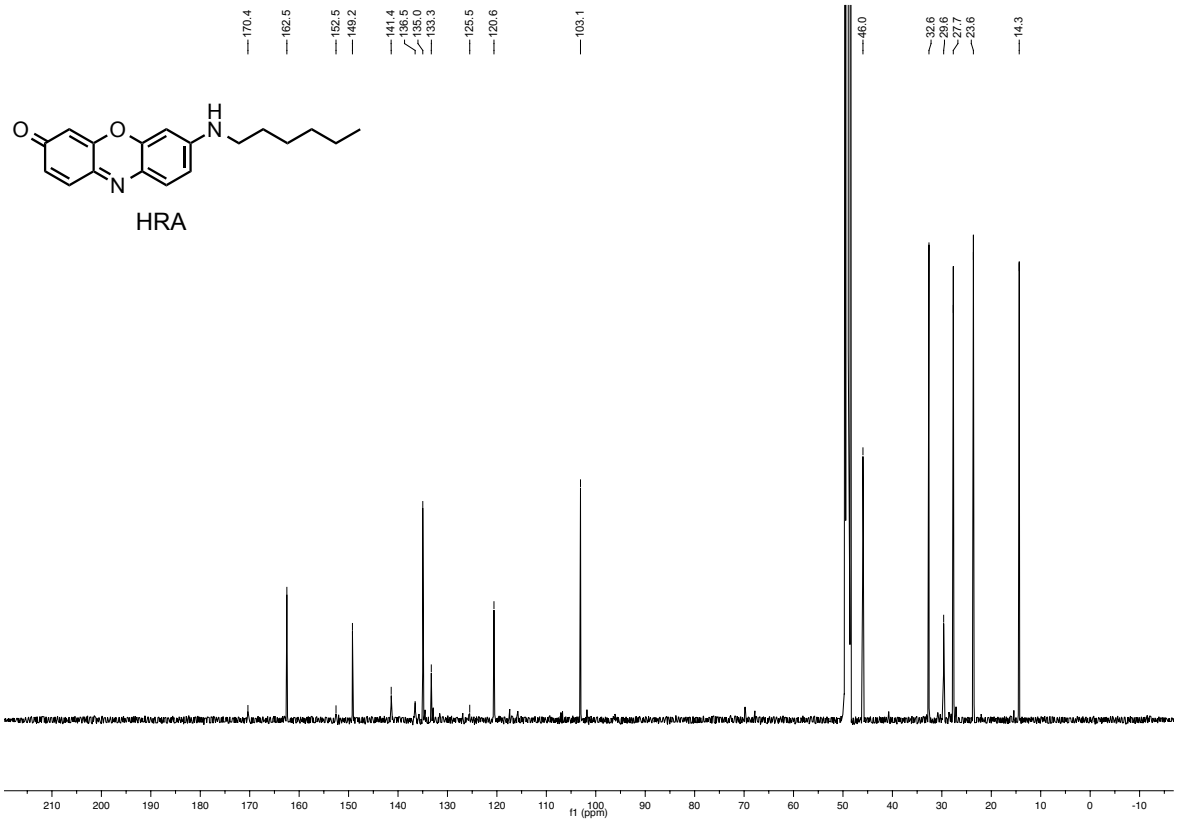

Figure 5.12. ^{13}C NMR (126 MHz, CD_3OD) spectrum of HRA.

APPENDIX C

Gene sequence and translation of Spy_MSP

```
 CCATGGGTTACTACCATCACCATCACCATCACGATTACGACATCCCAACGACCGAAAACCTG 60
  1  M  G  Y  Y  H  H  H  H  H  H  D  Y  D  I  P  T  T  E  N  L  20

 61 TATTTTCAGGGCTCTGGTGATAGTGCTACCCATATTAAATTCTCAAAACGTGATGAGGAC 120
 21  Y  F  Q  G  S  G  D  S  A  T  H  I  K  F  S  K  R  D  E  D  40

121 GGCAAAGAGTTAGCTGGTGCAACTATGGAGTTGCGTGATTCATCTGGTAAAACTATTAGT 180
 41  G  K  E  L  A  G  A  T  M  E  L  R  D  S  S  G  K  T  I  S  60

181 ACATGGATTTCAGATGGACAAGTGAAAGATTTCTACCTGTATCCAGGAAAATATACATTT 240
 61  T  W  I  S  D  G  Q  V  K  D  F  Y  L  Y  P  G  K  Y  T  F  80

241 GTCGAAACCGCAGCACCAGACGGTTATGAGGTAGCAACTGCTATTACCTTTACAGTTAAT 300
 81  V  E  T  A  A  P  D  G  Y  E  V  A  T  A  I  T  F  T  V  N  100

301 GAGCAAGGTCAGGTTACTGTAAATGGCAAAGCAACTAAAGGTGACGCTCATATCGGCTCT 360
101  E  Q  G  Q  V  T  V  N  G  K  A  T  K  G  D  A  H  I  G  S  120

361 GGTGGTTCTGGTCAaTTGAATCTGAAGTTGCTTGATAACTGGGATAGCGTTACGTCTACC 420
121  G  G  S  G  Q  L  N  L  K  L  L  D  N  W  D  S  V  T  S  T  140

421 TTCAGTAAACTTCGCGAACAACTGGGCCCCGTGACGCAGGAATTCTGGGACAACCTGGAA 480
141  F  S  K  L  R  E  Q  L  G  P  V  T  Q  E  F  W  D  N  L  E  160

481 AAAGAAACCGAGGGACTGCGTCAGGAAATGTCCAAAGATTTAGAAGAGGTGAAGGCCAAG 540
161  K  E  T  E  G  L  R  Q  E  M  S  K  D  L  E  E  V  K  A  K  180

541 GTTCAGCCATATCTCGATGACTTTCAGAAAAAATGGCAGGAAGAGATGGAATTATATCGT 600
181  V  Q  P  Y  L  D  D  F  Q  K  K  W  Q  E  E  M  E  L  Y  R  200

601 CAAAAGGTGGAACCGCTGCGTGCGGAACTGCAAGAGGGGGCACGCCAAAAACTCCATGAG 660
201  Q  K  V  E  P  L  R  A  E  L  Q  E  G  A  R  Q  K  L  H  E  220

661 CTCCAAGAGAAGCTCAGCCCATTAGGCGAAGAAATGCGCGATCGCGCCCGTGCACATGTT 720
221  L  Q  E  K  L  S  P  L  G  E  E  M  R  D  R  A  R  A  H  V  240

721 GATGCACTCCGGACTCATTTGGCGCCGTATTCGGATGAACTTCGCCAGCGTTTGGCCGCA 780
241  D  A  L  R  T  H  L  A  P  Y  S  D  E  L  R  Q  R  L  A  A  260

781 CGTCTCGAGGCGCTGAAAGAAAACGGGGGTGCCCGCTTGGCTGAGTACCACGCGAAAGCG 840
261  R  L  E  A  L  K  E  N  G  G  A  R  L  A  E  Y  H  A  K  A  280

841 ACAGAACACCTGAGCACCTTGAGCGAAAAAGCGAAACCGGCGCTGGAAGATCTACGCCAG 900
281  T  E  H  L  S  T  L  S  E  K  A  K  P  A  L  E  D  L  R  Q  300

901 GGCTTATTGCCTGTTCTTGAGAGCTTTAAAGTCAGTTTTCTGTCAGCTCTGGAAGAATAT 960
301  G  L  L  P  V  L  E  S  F  K  V  S  F  L  S  A  L  E  E  Y  320
```

```
 961 ACTAAAAAGCTGAATACCCAGGGCTCTGGTGGTTCTGGTGCGCATATTGTGATGGTGGAT 1020
  321  T  K  K  L  N  T  Q  G  S  G  G  S  G  A  H  I  V  M  V  D  340

1021 GCGTATAAACCGACCAAATAAGCTT 1045
 341  A  Y  K  P  T  K  *      346
```

Figure 5.13. SpyMSP (1-346) gene sequence and translation. This gene was expressed from pET28a after cloning into the NcoI and HindIII sites (underlined). For the D340A mutant, the GAT codon for Asp340 was changed to GCG.

APPENDIX D

List of cell lines used

Cell Line	Media	Growth	Cultivation temperature	Organism	Source	Notes
HeLa	DMEM +10% FBS +Pen/ Strep	Adherent	37 °C	Human (cervical tissue)	ATCC	ATCC #CCL-2
DH5alpha *E.coli*	Luria-Bertani Broth	n/a	37 °C	Bacteria	Peterson Lab	Cloning
BL21 (DE3) *E.coli*	Terrific Broth	n/a	37 °C (15 - 30 °C after IPTG induction)	Bacteria	Peterson Lab	Protein Expression

APPENDIX E

List of plasmids used

Name	Gene Product	Gene Species	Vector	Type	Source
pMSP1D1	Membrane Scaffold Protein	Synthetic gene	pET28a	Bacterial Expression Vector	Addgene #20061
pMSPSS_M6	Cys-MSP-Cys	Synthetic gene	pET28a	Bacterial Expression Vector	Subcloning
pSpyMSP	SpyCatcher-MSP-SpyTag	Synthetic gene	pET28a	Bacterial Expression Vector	GenScript
pSpyMSP D340A	SpyCatcher-MSP-D340A-SpyTag	Synthetic gene	pET28a	Bacterial Expression Vector	Subcloning
pStr-KDEL_SBP-EGFP-GPI	Streptavidin-KDEL and SBP-EGFP-GPI	Synthetic gene	pIRESneo3	Bacterial Expression Vector	Addgene #65294